STUDY OF HYDRODYNAMICS AND HEAT TRANSFER INDUCED BY MULTIPLE DROPLET TRAIN IMPINGEMENTS

A Dissertation

by

TAOLUE ZHANG

Submitted to the Office of Graduate and Professional Studies of
Texas A&M University
in partial fulfillment of the requirements for the degree of

DOCTOR OF PHILOSOPHY

Chair of Committee,	Jorge Alvarado
Co-Chair of Committee,	Reza Sadr
Committee Members,	Sai-Chuen Lau
	Yassin A. Hassan
	Michael Pate
Head of Department,	Andreas A. Polycarpou

May 2017

Major Subject: Mechanical Engineering

ABSTRACT

Recently, spray cooling heat transfer has received considerable attention due to its ability to dissipate high thermal loads. However, the physical mechanisms of spray cooling remain not well-understood due to the complexity of sprays. In order to better understand the underlying physical mechanisms found in spray cooling, a number of studies have been conducted by isolating spray parameters and focusing on well-controlled droplet train impingement cooling schemes. Most of the previous droplet train impingement studies have mainly focused on the thermal performance of single, double and collinearly arranged triple droplet train impingement. In the current study, the heat transfer and hydrodynamic characteristics of various droplet train impingement arrays have been investigated experimentally.

A piezo-electric droplet generation system has been designed and constructed, which is capable of producing well-controlled droplet trains arranged in various patterns (single, double, triangulated and hexagonal-arranged droplet trains). A translucent sapphire substrate, which was coated with a thin film ITO (Indium Tin Oxide), has been used as a heater in experiments. Well-calibrated high speed optical camera and IR thermal camera have been used to characterize the hydrodynamics and heat transfer of droplet train impingement.

Droplet-induced crown propagation dynamics has been analyzed experimentally. A revised crown propagation model was proposed in the current study, which is capable of predicting the crown base diameter as a function of time. A transition from crown

spreading to splashing has been observed by increasing droplet Weber number. Heat transfer measurements show that strong splashing was unfavorable for heat transfer due to the instability of the liquid film. For multiple droplet train impingement, it was found that impact spacing and impingement pattern play significant roles in terms of heat transfer performance. Furthermore, empirical heat transfer correlations have been postulated and fitted using experimental data for various impingement patterns. Results indicate that the postulated correlations are in good agreement with experimental data. Comparisons have been made between droplet train impingement and circular jet impingement for various impingement patterns. It has been found that droplet train impingement leads to much better heat transfer performance than circular jet impingement due to the effective mixing of fluid during droplet impingement process. In summary, the effects of droplet Weber number, impact spacing and impingement pattern on heat transfer and hydrodynamics during droplet train impingement have been explored and elucidated.

DEDICATION

To Dr. Jorge L. Alvarado for his inspiration and support

To my family for their unconditional love

ACKNOWLEDGEMENTS

I would like to thank my committee chair, Dr. Alvarado, my committee co-chair, Dr. Sadr, and my committee members, Dr. Lau, Dr. Hassan and Dr. Pate, for their guidance and support throughout the course of this research.

Thanks also go to my friends and colleagues and the department faculty and staff for making my time at Texas A&M University a great experience. I also want to extend my gratitude to the Qatar National Research Fund, which provided the funding for my research.

Finally, thanks to my family for their encouragement during my PhD study.

CONTRIBUTORS AND FUNDING SOURCES

Contributors

This work was supervised by a dissertation committee, consisting of Professor Jorge L. Alvarado [advisor] of the Department of Engineering Technology and Industrial Distribution [Outside Department], Professor Reza Sadr [co-advisor] of Mechanical Engineering Program in Texas A&M University at Qatar [Outside Department], Professors Sai-Chuen Lau and Michael Pate of Department of Mechanical Engineering [Home Department], Professor Yassin A. Hassan of Department of Nuclear Engineering [Outside Department].

The numerical data in Chapter 4.1.1 was provided by Jayaveera Muthusamy, PhD student in Department of Mechanical Engineering, Texas A&M University.

All other work conducted for dissertation was completed by the student independently.

Funding Sources

This work was supported by the National Priority Research Program (NPRP) of the Qatar National Research Fund (QNRF), grant No.: NPRP 6-1304-2-525.

NOMENCLATURE

A_d	Projected area of droplet
A_{htr}	Area of heater
c_p	Specific heat
d	Diameter
d_c	Crown diameter
$d_{c,rim}$	Crown rim diameter
$d_{c,base}$	Crown base diameter
$d_{c,rim,\max}$	Maximum crown rim diameter
d_c^*	Non-dimensional crown diameter $\left(\frac{d_c}{d_d}\right)$
d_{cra}	Crater diameter
d_d	Droplet diameter
d_j	Jet diameter
d_{orf}	Orifice diameter
D	Digital counts
E	Experimental uncertainty
f	Droplet impingement frequency for each droplet train

h	Heat transfer coefficient
h_{fg}	Latent heat of vaporization
h_{hump}	Hump height
$h_{spot}(r)$	Liquid film thickness within the initial spot
$\bar{h}_{spot}$	Average film thickness within the initial spot
h_0	Unperturbed liquid film thickness
h_0^*	Non-dimensional unperturbed liquid film thickness $\left(\frac{h_0}{d_d}\right)$
H_{in}	Liquid film thickness inside impact crater
H_{out}	Liquid film thickness outside impact crater
I	Current
k	Thermal conductivity
L_{heater}	Length of heater
$\dot{m}''$	Mass flux
n_{cusp}	Number of cusps
Nu_d	Nusselt number using diameter as characteristic length $\left(\frac{h \cdot d}{k}\right)$
Oh	Droplet Ohnesorge number $\left(\frac{\mu}{\sqrt{\rho \cdot \sigma \cdot d_d}}\right)$
q''	Heat flux

q''_{crt}	Critical heat flux
q_{loss}	Heat losses
Q	Volumetric flow rate
r	Radial position
$r_{c,rim,\max}$	Maximum crown rim radius
$r_{l,r}$	Lamella radius at crown's free rim
r_{rim}	Radius of crown's free rim
R	Radius of initial spot
Re	Reynolds number $\left(\frac{\rho \cdot V_d \cdot d}{\mu}\right)$
S	Horizontal impact spacing
S^*	Dimensionless impact spacing $\left(d_d / S\right)$
S_{in}	Inter-droplet spacing
St	Strouhal number $\left(\frac{f \cdot d_d}{V_d}\right)$
t	Dimensional time
t^*	Non-dimensional time $(2\pi \cdot f \cdot t)$
T	Temperature
$\bar{u}(r)$	Average radial velocity in the direction normal to liquid film
V	Voltage

V_d	Droplet impingement velocity
V_j	Jet impingement velocity
V_d^*	Non-dimensional droplet impingement velocity $\left(\frac{V_d \cdot \rho^{1/4}}{\sigma^{1/4} \nu^{1/8} f^{3/8}}\right)$
We	Droplet Weber number $\left(\frac{\rho \cdot d_d \cdot V_d^2}{\sigma}\right)$
μ	Dynamic viscosity
ρ	Density
σ	Surface tension
ν	Kinematic viscosity
ε	Emissivity

TABLE OF CONTENTS

Page

LIST OF FIGURES

Page

LIST OF TABLES

Page

CHAPTER I

INTRODUCTION

Future electronic systems will require the use of high heat flux removal technologies due to the amazing growth in thermal loads, which could lead to decreased reliability and reduced product life time. Innovative thermal management technologies are needed to improve the safety and reliability of electronic equipment. Over the past few decades, liquid cooling technologies such as jet impingement cooling, channel flow cooling and spray cooling have shown the ability to dissipate high thermal loads [1]. However, spray cooling does provide the best balance among high heat flux removal capability, isothermality and fluid inventory [2].

1.1. Motivation

During the past few decades, numerous studies [3-13] have been conducted to investigate the effects of spray parameters and surface structures on spray cooling heat transfer performance. However, the physical mechanisms of spray cooling are still not well understood due to the complexity of sprays. Some researchers [14-72] have tried to isolate spray parameters and focus their efforts on studying single droplet impingement and droplet train impingement. However, previous studies about droplet train impingement [48-57] have mainly focused on the heat transfer characteristics of single, double, and collinearly arranged triple droplet train impingement. Therefore, there is a

need to investigate the heat transfer and hydrodynamics of droplet train impingement arrays for the purpose of cooling applications.

1.2. Objective

The purpose of this study is to investigate the hydrodynamics and heat transfer induced by single droplet train impingement and droplet train impingement arrays for surface cooling applications. To satisfy this objective, piezo-electric droplet generators have been used to produce mono-dispersed droplet trains with the ability to control droplet impingement parameters such as droplet Weber number and horizontal impact spacing. Translucent heating elements have been fabricated using nano-fabrication techniques, such as Physical Vapor Deposition (PVD) and Plasma-Enhanced Chemical Vapor Deposition (PE-CVD) techniques. A high speed imaging system has been employed to observe the droplet train impingement dynamics. An infrared (IR) thermal imaging system has been employed to acquire heater surface temperature data. The study has revealed the effects of droplet Weber number and horizontal impact spacing on hydrodynamics and heat transfer performance of various droplet train impingement configurations. This work has also revealed that droplet train impingement leads to better heat transfer performance than circular jet impingement for various impingement configurations. Generally, this study attempts to increase the overall understanding of droplet impingement dynamics and droplet-induced surface cooling. It is also hoped that this study will be used in industry for the design of droplet impingement cooling systems.

1.3. Overview

This dissertation is divided into five chapters. Chapter II presents a review of literature in the area of spray cooling, droplet impingement dynamics and droplet impingement cooling. Chapter III describes the experimental setup used in this work and uncertainty analysis of all the measurements. Chapter IV includes experimental results and analysis of the heat transfer and hydrodynamics induced by single and multiple droplet train impingements. Comparison between droplet train impingement and circular jet impingement are also included in Chapter IV. Chapter V includes conclusions and recommendations for future work.

CHAPTER II

LITERATURE REVIEW

2.1. Literature review of spray cooling

During the past few decades, numerous studies have been carried out to investigate the effects of spray parameters on surface cooling. For instance, in the studies conducted by Chen et al. [3, 4], the effects of droplet velocity, droplet flux and droplet diameter on surface cooling were investigated. In their study [3, 4], it was found that droplet velocity has the most dominant effect on critical heat flux (CHF), followed by droplet flux and droplet diameter [3, 4].

Tilton [5] studied spray cooling experimentally by using pressure-atomized water sprays. The average droplet diameter and mean droplet velocity were about 80 μm and 10 m/s, respectively [5]. Tilton [5] claimed that lower droplet diameter leads to higher heat transfer coefficient. Tilton [5] also claimed that mass flow rate of water may not be a factor in controlling CHF.

Sehmbey et al. [6] studied the heat transfer characteristics of liquid nitrogen spray cooling using different nozzles and various flow rate. Sehmbey et al. [6] found that heat transfer coefficient increases with mass flow rate of the cooling liquid. It was also found that both CHF and heat transfer coefficient increase as the orifice size of the nozzle decreases [6].

Rini et al. [7] studied the effects of droplet-bubble interactions on spray cooling performance. Rini et al. [7] claimed that higher droplet flux leads to an increase in

secondary nucleation sites, which is favorable for heat transfer. Rini et al. [7] also claimed that higher droplet flux leads to a shorter nucleation bubble growth time (i.e. the early removal of nucleation bubble).

Researchers have also investigated the effects of impact angle on spray cooling heat transfer performance. For instance, Schwarzkof et al. [8] studied the effects nozzle inclination angle on spray cooling using PF5060 as heat transfer fluid. The inclination angle was varied between 0º and 60º with respect to the direction of gravity [8]. Schwarzkof et al. [8] found that the cooling capacity remained the same when the inclination angle was set to below 40º, but dropped off significantly when the angle exceed 40º.

Aguilar et al. [9] studied the effects of impact angle between nozzle and skin surface on cryogenic spray cooling. Aguilar et al. [9] claimed that a 90º impact angle (i.e. normal impact) leads to the optimum heat transfer performance. They [9] also found that angles as low as 15º with respect to the surface have an insignificant effect on heat transfer. Only exaggerated angles of 5º result in a 10% lower heat flux and 30% lower heat extraction with respect to the normal impact condition. Their findings are consistent with the experimental results obtained by Zhang et al. [53]

Mudawar and Estes [10] optimized CHF in spray cooling of a square surface by adjusting nozzle-to-surface distance. It was found that CHF could be maximized when the spray was configured such that the spray area just impinged the square surface of the heater [10].

Many researchers have found out that spray cooling performance could be greatly enhanced by using structured surfaces. For instance, Silk et al. [11] studied the effects of surface geometries on spray cooling by machining and using millimeter scale cubic pin fins, pyramids, and straight fins on the top surface of copper blocks with a cross-sectional area of 2 cm^2. The surface area of the cubic finned surface and the straight finned surface was 4.0 cm^2, while the pyramids finned surface had a surface area of 4.5 cm^2 [11]. All the structured surfaces led to higher CHF when compared with the flat surfaces, which they attributed to an increase in surface area [11]. They also found that the straight finned surface had the largest CHF enhancement relative to the flat surface, followed by the cubic pin finned and pyramids finned surfaces [11]. Their results indicate that heat transfer does not scale directly with total wetted area. Furthermore, it has been speculated that straight finned surface leads to higher CHF due to greater surface flow confinement effects [11].

Hsieh and Yao [12] studied the effects of micro-structured surfaces on water spray cooling by fabricating and using square micro-studs arrays with various Bond numbers and groove area on silicon surfaces. Four heat transfer regimes were classified in their study, namely: flooded regime, thin film regime, partial dryout regime and dryout regime [12]. It was found that micro-textured surfaces usually lead to better heat transfer performance compared with a bare surface in the thin film and partial dryout regimes [12]. They attributed the heat transfer enhancement to an effective capillary force within the micro-structures, which helps the spreading of deposited liquid film over the heated surface, keeping the surface wetted at high heat flux values [12]. It was

also found that Bond number of the microstructures is the primary factor responsible for the heat transfer enhancement when micro-textured surfaces are used [12]. However, surface texture has negligible effects on heat transfer performance in the flooded and dryout regimes because the heated surface was totally covered by liquid in the flooded regime, and by vapor in the dry out regime [12].

Kim et al. [13] studied the effects of micro-porous surfaces on water spray cooling by applying micron-size aluminum particles on heater surfaces. It was found that heat transfer coefficient could be greatly enhanced by using micro-porous surfaces [13]. Furthermore, micro-porous surfaces can increase CHF significantly (about 21 W/cm^2) over plain surfaces (about 15 W/cm^2), which they attributed to the capillary pumping effect of the micro-porous coatings [13]. However, the size of the micro-scale particle coatings was found to have a negligible effect on heat transfer performance [13].

2.2. Literature review of droplet impingement dynamics

Droplet impingement is a common phenomenon encountered in spray and discrete droplet impingement cooling. Therefore, the study of the hydrodynamics of droplet impingement can help understand the physical mechanisms of spray and droplet impingement cooling in terms of dimensionless physical variables such as Weber number.

2.2.1. Literature review of droplet impact on solid dry surfaces

Droplet impact on dry surfaces exhibit complicated features due to the effects of droplet properties, surface roughness and wettability. For instance, in the experimental studies conducted by Rioboo et al. [14], six distinct outcomes of single droplet impact on dry surfaces were identified, namely: deposition, prompt splash, corona splash, receding break-up, partial rebound and complete rebound. Qualitative analysis have also been conducted to investigate the effects of experimental variables, such as droplet velocity, droplet diameter, surface roughness and contact angle on the hydrodynamics of droplet impingement. It has been found that not all outcomes are achievable for a given droplet-surface combination [14].

Rioboo et al. [15] studied the evolution of single droplet impingement on dry surfaces. Four evolution phases have been identified, namely: kinematic phase, spreading phase, relaxation phase, and wetting/equilibrium phase. It has been found that the diameter of the spreading droplet is proportional to $t^{1/2}$ only in the kinematic phase.

Roisman et al. [16] studied inertia dominated droplet impingement on a solid dry surface both numerically and theoretically. A theoretical model was proposed to predict the droplet-induced liquid film thickness [16]. Roisman et al. [16] claimed that when the droplet Weber number and Reynolds number are high enough (i.e. inertia dominated), the flow generated by droplet impingement is universal near the impingement center. Roisman et al. [16] also claimed that the dimensionless film thickness is independent of droplet properties and surface wettability when droplet impingement is inertia dominated.

Mundo et al. [18] studied the deposition-splashing transition for droplet-solid wall interactions. An empirical correlation, as shown in Equation 1, was proposed to predict the transition between deposition and splashing for single droplet impact on hydrophilic surfaces [18].

$$\left(Oh \cdot \mathrm{Re}^{1.25}\right)_{crt} = K \tag{1}$$

In Equation 1, K is a constant, which depends on the roughness of the surface. Mundo et al. [18] claimed a K value of 57.7 for smooth surfaces, where Oh and Re are Ohnesorge number and Reynolds number of the impinging droplets, respectively. In general, when the left hand side of Equation 1 exceeds the value of K, the droplets tend to splash.

2.2.2. Literature review of droplet impact on liquid films

Droplet-thin liquid film interactions are usually accompanied with crown propagation phenomena [19-28]. For instance, Cossali et al. [19] studied the crown propagation dynamics induced by droplet-thin liquid film interactions. Cossali et al. [19] plotted crown diameter (d_c) as a function of time (t). Correlations by Cossali et al. [19] show that $d_c = K \cdot t^n$, where K is a constant and n is very close to 0.5.

Mukherjee and Abraham [20] studied the effect of liquid film thickness on crown propagation dynamics. A Lattice-Boltzmann model was employed in their numerical work [20], in which they [20] found that crown diameter increases with liquid film thickness when non-dimensional film thickness (h_0^*) is lower than 0.25. Nevertheless, when the film was thicker ($h_0^* > 0.25$), the opposite trend was observed [20].

Yarin and Weiss [23] studied the hydrodynamics of droplet train (stream of successive droplets) impingement and proposed a theoretical model (hereinafter referred to as YWM) to predict crown base diameter as a function of time, as follows:

$$d_{\mathrm{c,base}} = 2 \cdot (2Ft)^{1/2} \tag{2}$$

The value of F in Equation 2 depends on the conditions of initial spot formation, which is defined as the moment when crown base propagation velocity equals to droplet impingement velocity [23]. Equation 3 was used to determine the value of F, as follows:

$$F = \int_0^L \bar{u}(r) dr \tag{3}$$

In Equation 3, L is the length crown propagation domain, $\bar{u}(r)$ is the average radial velocity in the direction normal to the liquid film.

Yarin and Weiss [23] in their model formulation assumed that $\bar{u}(r)$ is equal to V_d at the center of initial spot, while $\bar{u}(r)$ is equal to 0 elsewhere:

$$\bar{u}(r) = \begin{cases} V_d, & 0 \le r \le R \\ 0, & r > R \end{cases} \tag{4}$$

In Equation 4, V_d refers to droplet impingement velocity. The radius of the initial spot, R, is estimated from the mass balance equation, as follows:

$$\rho \pi R^2 \bar{h}_{spot} = \frac{1}{6} \rho \pi d_d^3 \tag{5}$$

In Equation 5, d_d refers to droplet diameter and $\bar{h}_{spot}$ refers to the average liquid film thickness within the initial spot. Yarin and Weiss [23] assumed that $\bar{h}_{spot}$ is equal to

the thickness of the unperturbed liquid film (h_0) produced by the impingement droplets, as follows:

$$\bar{h}_{spot} = h_0 \tag{6}$$

By using the above assumptions shown in Equations 4, 5 and 6, a simplified YWM takes the mathematical form of:

$$d_{c,base} = \left[2d_d \cdot \left(\frac{2}{3} \right)^{1/4} \cdot \frac{V_d^{1/2}}{d_d^{1/4} h_0^{1/4}} \right] \cdot t^{1/2} \tag{7}$$

The non-dimensional form of this simplified YWM is as follows:

$$d_{c,base}^{*} = \left[\frac{2V_d^{1/2}}{6^{1/4} h_0^{1/4} \pi^{1/2} d_d^{1/4} f^{1/2}} \right] \cdot \left(t^{*} \right)^{1/2} \tag{8}$$

Where,

$$d_{c,base}^{*} = \frac{d_{c,base}}{d_d}$$

$$t^{*} = 2\pi f t$$

Yarin and Weiss [23] also proposed an equation to predict the unperturbed liquid film thickness (h_0) induced by droplet train impingement, as follows:

$$h_0 = \left(\frac{\nu}{f} \right)^{1/2} \tag{9}$$

Yarin and Weiss [23] found that the theoretical predictions given by Equations 8 and 9 reach reasonable agreement with experimental data. However, theoretical predictions given by Equations 8 and 9 consistently over-predict crown propagation diameter as a function of time [23]. Yarin and Weiss [23] and Yarin [24] attributed the over-prediction to the exclusion of viscous losses at the moment of droplet impingement.

Trujillo and Lee [25] proposed a crown propagation model by taking into account viscous losses during droplet impingement. Their predictions [25], however, are rather close to the predictions given by YWM [23].

It should be noted that YWM should be used for the prediction of crown base diameter. Rieber and Frohn [26] and Shetabivash et al. [27] have clarified this point in their numerical crown propagation studies. Nevertheless, Yarin and Weiss [23] compared the theoretical predictions given by YWM with the crown rim diameter data measured experimentally. Fig. 1 shows a schematic diagram which depicts crown base diameter and rim diameter from a cross-sectional point of view. However, in experiments, it is difficult to see the propagation of droplets clearly. This is because the crowns and liquid rims formed by propagating droplets tend to block the field of view of the crown propagation region. As a result, it is difficult to determine the exact crown base location using experimental side view images [23].

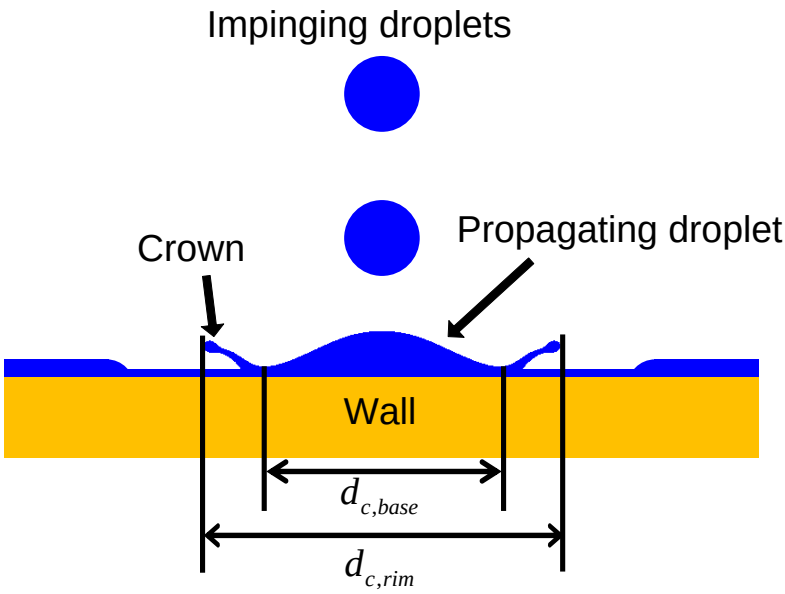

Fig. 1. Schematic diagram of crown base diameter and rim diameter

Rieber and Frohn [26] conducted numerical studies of single droplet impacting on thin liquid films by solving Navier-Stokes equation directly. In their study [26], crown base diameter was determined as a function of time, and the numerical results reached excellent agreement with the original results of the YWM (Equations 2 and 3). However, the simplified YWM proposed by Yarin and Weiss [23] greatly over-predicts crown propagation [26]. Rieber and Frohn [26] attributed the over-prediction to the assumptions associated with $\bar{u}(r)$ proposed by Yarin and Weiss [23] (i.e. Equation 4). Rieber and Frohn [26] claimed that at the moment of initial spot formation, $\bar{u}(r)$ varies linearly between 0 at the center or point of impact, and V_d at the crown base location, as postulated in Equation 10.

$$\bar{u}(r)=\begin{cases}\dfrac{r}{R}V_d, & 0\le r\le R\\ 0, & r>R\end{cases} \tag{10}$$

By using the assumptions shown in Equations 5, 6 and 10, Rieber and Frohn [26] came up with a different simplified YWM:

$$d_{c,base}=\left[2d_d\cdot\left(\frac{1}{6}\right)^{1/4}\frac{V_d^{1/2}}{d_d^{1/4}h_0^{1/4}}\right]\cdot t^{1/2} \tag{11}$$

The non-dimensional form of Equation 11 is as follows:

$$d^*_{c,base}=\left[\frac{\sqrt{2}V_d^{1/2}}{6^{1/4}h_0^{1/4}\pi^{1/2}d_d^{1/4}f^{1/2}}\right]\cdot\left(t^*\right)^{1/2} \tag{12}$$

The predictions given by Equation 11 agree very well with the numerical results by Rieber and Frohn [26].

Shetabivash et al. [27] studied the crown propagation dynamics induced by single droplet impingement, and compared their numerical results of crown base propagation with the predictions given by Equations 7 and 11. Shetabivash et al. [27] found that the estimates given by Equation 7 greatly over-predict crown propagation while an excellent agreement was reached when using Equation 11. The disagreement clearly indicates that the assumptions should be carefully postulated to simplify the YWM in order to obtain accurate crown propagation predictions.

2.2.3. Literature review of droplet-induced splashing dynamics

Droplet-induced splashing is a fascinating fluid dynamic phenomenon that has been studied by many researchers [23-45]. For instance, Yarin and Weiss [23] studied

the transition from spreading to splashing induced by droplet train impingement experimentally. Yarin and Weiss [23] defined splashing as the emergence of secondary droplets from the rim of the droplet-induced crown. Yarin and Weiss [23] claimed that splashing threshold cannot be described solely by the droplet Reynolds number or Weber number. Therefore the non-dimensional droplet impingement velocity (V_d^*), as described in Equation 13, has been used to describe the transition threshold:

$$\left(V_d^*\right)_{crt} = \left(\frac{V_d \rho^{1/4}}{\sigma^{1/4} \nu^{1/8} f^{3/8}}\right)_{crt} = 17 \sim 18 \tag{13}$$

In Equation 13, V_d, ρ, σ, ν and f stand for velocity, density, surface tension, kinematic viscosity and impingement frequency of the droplet train, respectively. Yarin and Weiss [23] claimed that when V_d^* exceeds a value of 18, droplets tend to splash upon impact.

Cossali et al. [29] studied the mechanism of crown splashing induced by single droplet impact on thin liquid films. Various mixtures of water and glycerol were used to span a wide range of fluid properties [29]. An experimental correlation, as shown in Equation 14 was proposed to predict the spreading-splashing transition threshold.

$$\left(Oh^{-0.4} \cdot We\right)_{crt} = 2100 + 5880 \cdot \left(h_0^*\right)^{1.44} \tag{14}$$

Where,

$$0.1 < h_0^* < 1$$
$$Oh > 0.007$$

In Equation 14, Oh and We are the Ohnesorge number and Weber number of the impinging droplets, respectively. h_0^* is the non-dimensional liquid film thickness. In

general, when the left hand side exceeds the right hand side of Equation 14, droplets tend to splash upon impact.

Wang and Chen [30] studied the splashing dynamics induced by single droplet impact on thin liquid films. A novel experimental method was employed to produce thin liquid films (h_0^*<0.1) [30]. Break-up of droplet-induced crown was observed during the crown propagation process at a h_0^* value of 0.05 [30].

Cheng and Lou [31] studied the effects of droplet impingement angle on splashing dynamics. A wide range of impact angles (0~60°) were used in their numerical work [31]. They [31] found that splashing was asymmetric when impingement was oblique (i.e. impact angle > 0°). It was also found that the increase of the impact angle leads to a transition from splashing to partial splashing and spreading [31].

The physical mechanisms associated with droplet-induced splashing are complicated and different mechanisms have been used to explain the phenomena [26, 34-37]. For instance, Rieber and Frohn [26] claimed that Plateau-Rayleigh instability theory could be used to explain droplet-induced splashing. Rieber and Frohn [26] also determined the number of cusps on the crown's free rim numerically and compared it with the predictions given by Equation 15, as follows:

$$n_{cusp} = \frac{2\pi \cdot r_{l,r}}{9.0147 \cdot r_{rim}} \tag{15}$$

In Equation 15, $r_{l,r}$ stands for the lamella radius at the crown's free rim, and r_{rim} represents the radius of the free rim. Definitions of $r_{l,r}$, r_{rim} and other splashing-related

terminologies are shown in Fig. 2. A detailed description of the relevant splashing-related terminologies can be found in Cheng and Low [31].

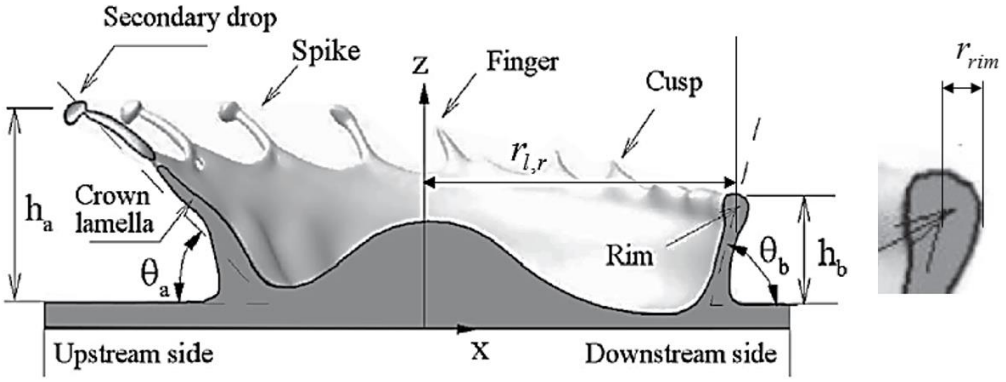

Fig. 2. Definition of splashing-related terminologies by Cheng and Low [31]

Rieber and Frohn [26] found that the predictions given by Equation 15 could reach good agreement with numerical data. Zhang et al. [34] studied droplet-induced splashing experimentally and reached similar conclusions with Rieber and Frohn [26]. However, Yoon et al. [35] and Liu et al. [36] claimed that droplet-induced splashing phenomena may be described using Kevin-Helmholtz instability theory, rather than Plateau-Rayleigh instability theory or Rayleigh-Taylor instability theory. Krechetnikov [37] claimed that droplet-induced splashing was due to both Rayleigh-Taylor and Richtmyer-Meshkov instabilities. The disagreement indicates that the physical mechanism of droplet-induced splashing should be further investigated.

2.3. Literature review of droplet impingement cooling

Droplets in spray cooling are usually generated by nozzles, which cannot generate mono-dispersed droplets. In order to better understand the mechanisms of spray cooling, researchers [46-72] have tried to isolate spray parameters and focused their efforts on studying single droplet impingement cooling and droplet train impingement cooling.

Herbert et al. [46] investigated the heat and mass transfer during a droplet impinging on a hot wall both experimentally and numerically. Herbert et al. [46] found that single phase forced convection was the dominant heat transfer mechanism during the initial stage of the impingement process. However, at the final stage of the impact, heat transfer near the three-phase contact line was dominated by evaporation.

Shen et al. [47] examined the hydrodynamics and heat transfer characteristics of a single water droplet impinging on smooth and nano-porous surfaces. It was found that there was an increase in impact diameter on a nano-porous surface when the surface was heated [47]. The increased droplet spreading on the nano-structured surface suggests a greater potential for increased heat transfer [47].

Sawyer et al. [49] investigated the critical heat flux (CHF) of surface cooling induced by single droplet train impingement. A major contribution of the work by Sawyer et al. [49] is a correlation which can be used to predict CHF as a function of droplet Weber number and Strouhal number, as follows:

$$\frac{q''_{crt}}{\rho_L h_{fg} V_d} = 0.166 \cdot We^{-0.4138} St^{0.8906} \tag{16}$$

Where,

$$175 \le We \le 730$$
$$0.007 \le St \le 0.03$$

Healy et al. [50] studied the CHF of single water droplet train impingement cooling at low droplet Weber number conditions. Healy et al. [50] claimed that the CHF prediction given by Sawyers et al. [50], as shown in Equation 16, does not predict CHF well in the droplet Weber number range of 55 to 109. Healy et al. [50] attributed the disagreement to the splashing of droplet impingements at higher Weber numbers. However, hydrodynamics of droplet impingement were not discussed in Healy et al. [50].

Sellers and Black [51] undertook a study to investigate the thermal performance of single water droplet train with droplet diameters in the range of 50 to 300 μm, and droplet impingement velocities in the range of 3 to 14.2 m/s. Sellers and Black [51] also proposed a CHF correlation as a function of droplet Weber number and Strouhal number, but they used a different non-dimensional CHF compared with Sawyer et al. [49]. The correlation is as follows:

$$\frac{q''_{crt}}{\dot{m}'' h_{fg}} = 1.1145 \cdot We^{-0.1202} St^{-0.1431} \tag{17}$$

Where,

$$23 \le We \le 202$$
$$0.047 \le St \le 0.58$$

It should be noted that early studies about droplet train impingement cooling [49-51] used embedded thermocouples in heating elements to measure surface temperatures,

which could only provide limited assessment and understanding of the key heat transfer mechanism within the droplet impingement zone. Furthermore, information about hydrodynamics of droplet train impingement was not included in these studies [49-51].

Recently, researchers have used high speed imaging and infrared (IR) thermal imaging techniques to characterize the hydrodynamics and heat transfer of droplet train impingement cooling. Both imaging techniques have helped better understand the physics of droplet impingement cooling.

For instance, Tsai [52] and Zhang et al. [53] studied single and double droplet train impingement cooling experimentally. An IR camera was used to measure surface temperature distribution [52-53]. It was found that a 0° droplet impingement angle (i.e. droplets impacting heater surface normally) results in optimum heat transfer performance for a single droplet train impingement cooling [52-53]. For double droplet train impingement cooling, heat transfer is highly dependent on the horizontal impact spacing.

Soriano [54] and Soriano et al. [55] studied the effects of single and collinearly arranged triple droplet train impingement on liquid film heat transfer. Soriano [54] and Soriano et al. [55] claimed that high frequency droplet train impingement cooling leads to a more uniform Nusselt number distribution compared with circular jet impingement cooling. Soriano [54] and Soriano et al. [55] also claimed that single phase forced convection was the main heat transfer mechanism within the impact craters even at high heat flux conditions.

Lin [56] and Alvarado and Lin [57] studied the effects nano-structured surfaces on droplet train impingement cooling. Nanoscale pillar arrays were fabricated on the heater surface using Step Flash and Imprinting Lithography (S-FIL) technique [58]. Lin [56] and Alvarado and Lin [57] found that heat transfer was greatly enhanced when nano-structured surfaces were used. Heat Transfer enhancement was attributed to a better surface wettability when using nano-structured surfaces [56-57].

Trujillo et al. [59] investigated the heat and momentum transfer characteristics of single droplet train impingement numerically. Trujillo et al. [59] claimed that crown propagations induced by droplet train impingement help convect hotter bottom liquid upwardly and outwardly, leading to an effective thermal mixing mechanism. It was also found that the compression of the liquid film to 15 μm inside the impact crater allowed for a significant rise in heat transfer through the liquid film, helping dissipate a large portion of heat [59].

In the numerical studies conducted by Trujillo and Lewis [60], an analytical expression for the Nusselt number radial profile was developed for single droplet train impingement cooling. It was found that the Nusselt number scales as $\sim Re^{1/2}$, which is consistent with the results obtained for circular liquid jet impingement by Liu et al. [61]. This indicated that circular jet impingement and droplet train impingement bare some similarities in terms of heat transfer.

2.4. Gaps identified in the current knowledge

Based on the literature review in the area of spray cooling, droplet impingement dynamics and droplet impingement cooling, gaps in the current knowledge base have been identified, as follows:

- The physical mechanisms of spray cooling are not well understood due to the complexity of sprays, which are characterized by having high droplet flux, droplets with random trajectories and impact angles [2-13]. Therefore, there is a need to isolate spray parameters and focus on the study of droplet impingement dynamics and droplet-induced surface heat transfer.
- Previous model about droplet-induced crown propagation dynamics [23] have shown the limited ability to give accurate predictions. There is a need to revise the previous crown propagation model in order to obtain accurate crown propagation predictions.
- Previous studies about droplet train impingement cooling [49-60] have mainly focused on the thermal performance of droplet train impingement. There is a need to investigate the role of hydrodynamics of droplet train impingement on cooling in more depth.
- Previous studies about droplet train impingement cooling [49-60] only investigated single, double and collinear arranged triple droplet train impingement cooling. There is a need to investigate the heat transfer and

hydrodynamics of multiple droplet train impingement arrays for the purpose of cooling applications.

2.5. Study objectives

With the goal of gaining a better understanding of hydrodynamics and heat transfer of droplet train (droplet stream) impingement cooling, well-controlled experiments have been performed with the following specific objectives:

- To differentiate droplet-induced crater and crown, and to investigate the physical relationship between them.
- To revise the simplified crown propagation model proposed by Yarin and Weiss [23] for the purpose of obtaining accurate crown propagation predictions.
- To postulate crown propagation model based on empirical results.
- To study the effects of droplet-induced spreading-splashing transition on hydrodynamics and surface heat transfer.
- To study the heat transfer process and hydrodynamics of triangulated droplet train impingement array.
- To design and construct a droplet train impingement prototype capable of producing multiple droplet train impingement arrays.
- To study the heat transfer and hydrodynamics of hexagonal droplet train impingement arrays.

- To postulate dimensionless correlations for droplet-induced film hydrodynamics and surface heat transfer.
- To compare the heat transfer performance of droplet train impingement and circular jet impingement for various impingement patterns.

CHAPTER III

EXPERIMENTAL SETUP AND UNCERTAINTY ANALYSIS

In this chapter, description of experimental setup, which was used to conduct droplet impingement experiments is presented. Additionally, the experimental methodologies and experimental uncertainty analysis are introduced and discussed.

3.1. Experimental setup

An experimental setup, as the one shown in Fig. 3, was developed and used to conduct droplet impingement experiments. Generally, the experimental setup comprises of three subsystems, namely, droplet production system, heater system and the data acquisition system. Detailed descriptions of each subsystem are provided below.

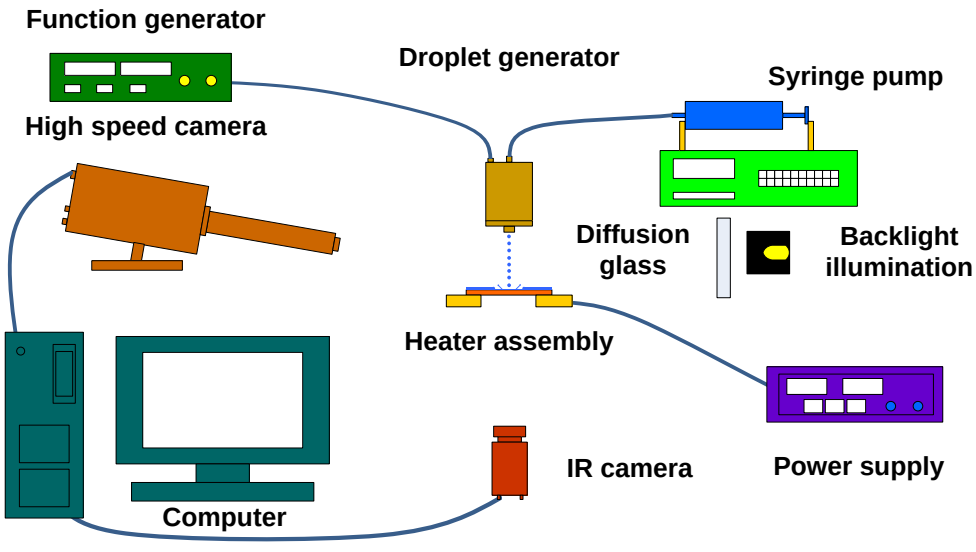

Fig. 3. Schematic diagram of experimental setup

3.1.1. Droplet production system

In this study, 3M Novec engineering fluid (HFE-7100) was selected as cooling liquid due to its low saturation point of 61 ºC and dielectric properties, which make it suitable for electronic cooling applications. Thermal physical properties of HFE-7100 are shown in Table 1, as follows:

Table 1. Thermal physical properties of HFE-7100 at room temperature (data from 3M)

Density, ρ (kg/m^3)	1520
Saturation point, T_{sat} (ºC)	61
Latent heat of vaporization, h_{fg} (kJ/kg)	111.6
Specific heat, c_p (J/kg-K)	1173
Thermal conductivity, k (W/m-K)	0.07
Surface tension, σ (N/m)	0.0136
Dynamic viscosity, μ (kg/m-s)	0.00061

The cooling liquid was delivered to the droplet generator using a syringe pump (Cole Parmer dual syringe pump, accuracy: 0.1% of rated flow rate) and disturbed by high frequency vibrations as it flowed through the droplet generator. In this work, single, double and triangulated triple droplet trains were produced by using a droplet generator made by TSI Corporation (TSI MDG-100 Monosize Droplet Generator). However, the droplet generator made by TSI Corporation has limited ability to produce multiple droplet train arrays. A droplet impingement prototype with higher capacity was designed

and constructed, which is capable of producing hexagonal droplet train arrays. Fig. 4 shows the components and CAD drawings of the prototype.

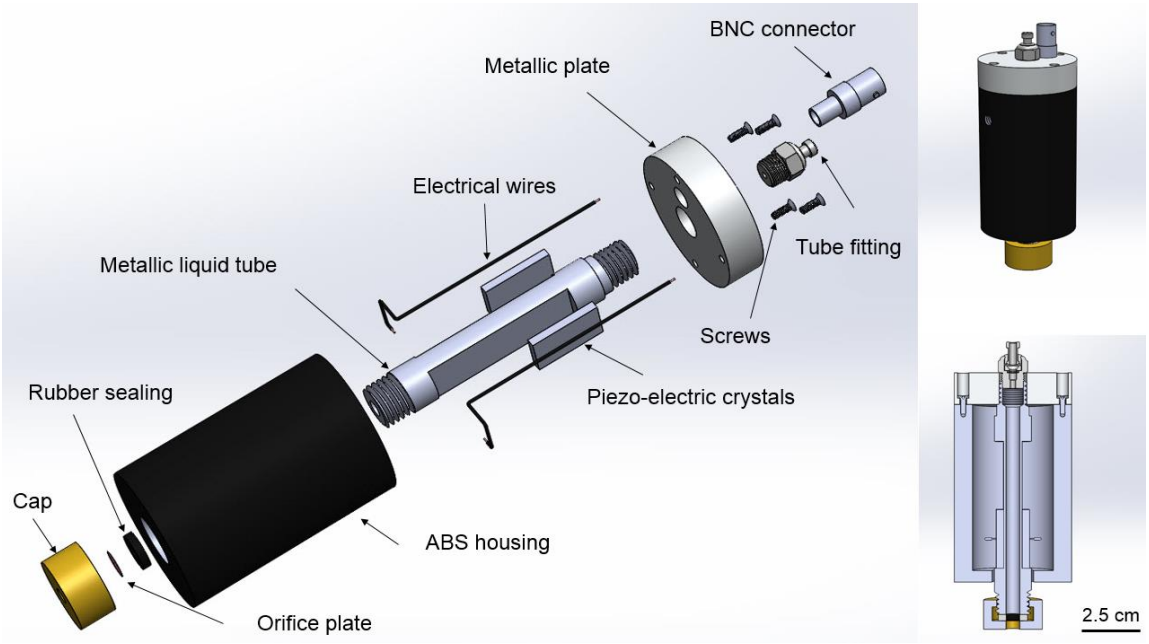

Fig. 4. Components and 3-D CAD drawings of droplet impingement prototype

The working principle of the droplet impingement prototype and the overview of droplet trains produced by the prototype are shown in Fig. 5. As shown in Fig. 5, a pair of piezo-electric crystals were attached to the metallic liquid tube using silver-based electrical conductive epoxy. Square wave signals produced by a function generator (BK Precision Model 4011 A, accuracy: ± 10 Hz) were used to induce vibrations of the piezo-electric crystals, which caused the breakup of the liquid jets based on Plateau-Rayleigh instability [32-33].

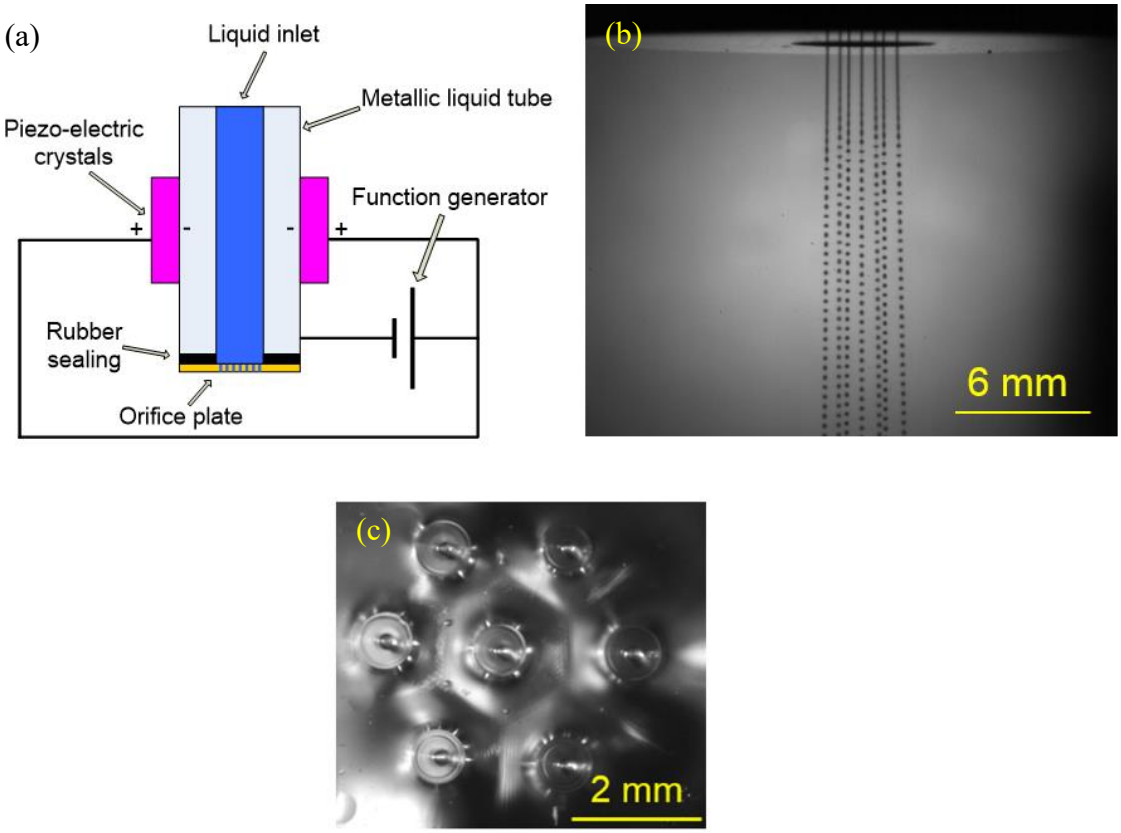

Fig. 5. (a) Working principle of the droplet impingement prototype, (b) overview of hexagonal droplet trains produced by the prototype and (c) bottom view of hexagonal droplet train impingement

An orifice plate, as shown in Fig. 6, was mounted at the bottom of the droplet generator to produce droplet trains. In this work, all the orifice plates were fabricated by National Aperture Inc. using the etching method. All the orifices were etched on thin film stainless steel foil (thickness = 12 μm) to ensure the high quality of orifices with smooth edges. Orifice plates with desired orifice diameters and patterns were used to produce droplet trains in a wide range of droplet Weber numbers and horizontal impact spacings. Impact heights (3-6 cm) were carefully chosen to make sure well-formed

droplets could remained spherical during the impingement process. The effects of drag on droplet velocity and evaporation of droplets before impingement were found to be negligible [55].

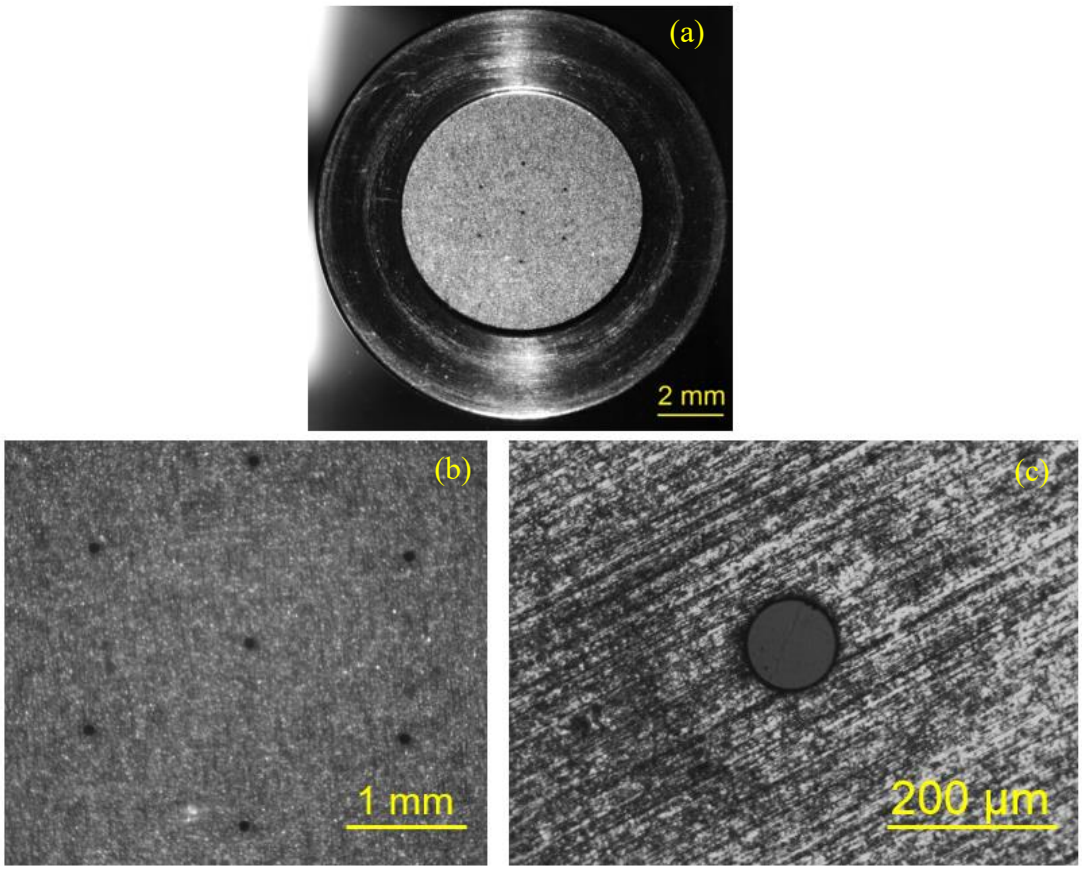

Fig. 6. (a) Hexagonal array orifice plate, (b) zoomed view of orifice array and (c) zoomed view of a single orifice

In the current work, the droplet generators were also used to produce circular jets by turning off the function generator. The purpose of producing circular jets is to compare the cooling performance between droplet train impingement and circular jet impingement (see Section 4.5 for detailed information about the comparison between circular jet impingement cooling and droplet train impingement cooling). Impact heights (about 5 mm) were carefully chosen to make sure the jets remained circular and stable during impingement process. Fig. 7 shows the production of mono-dispersed droplet trains and circular jets at a same flow rate condition. As shown in Fig. 7(a), circular jets break-up into mono-dispersed droplet trains when the function generator was turned on. In Fig. 7(b), circular jets finally break-up into random droplets when the function generator was turned off. In this study, the impact heights were carefully chosen to make sure the droplet trains remained mono-dispersed while jets remained circular and stable during impingement process.

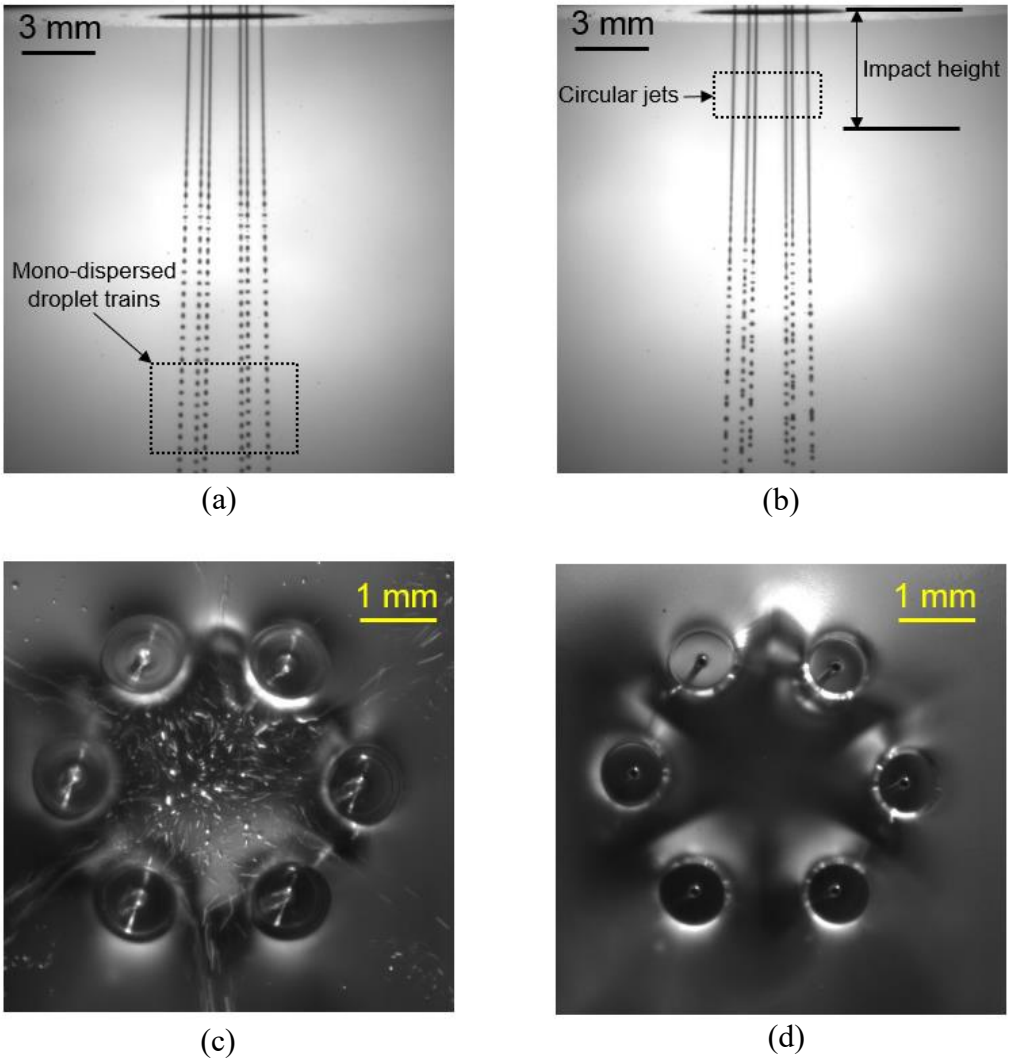

Fig. 7. Productions of (a) mono-dispersed droplet trains at f = 8000 Hz and (b) circular jets when function generator was off, bottom view of (c) droplet trains and (d) circular jets impingement. All images were captured at Q = 6*100 mL/h, d_{orf} = 100 µm and S = 1.8 mm

3.1.2. Heater system

A heater assembly as the one shown in Fig. 8, was used to conduct droplet impingement heat transfer experiments.

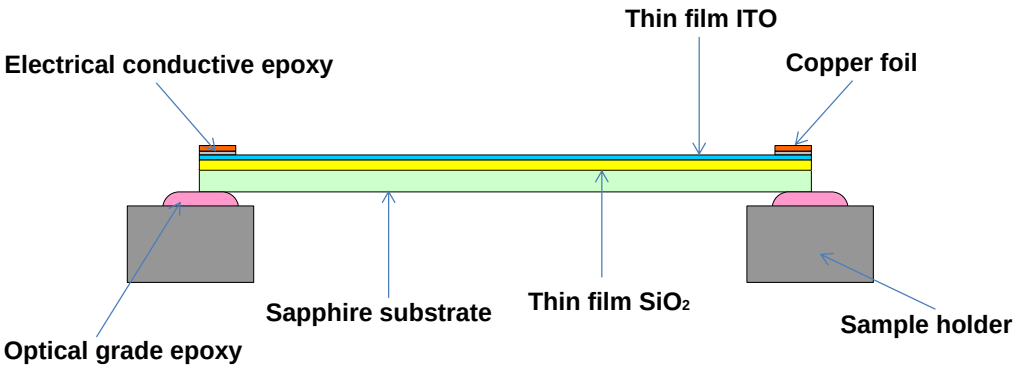

Fig. 8. Schematic diagram of heater assembly

The heater was made by coating a thin layer of Indium Tin Oxide (ITO) of approximately 190 nm in thickness on a 0.25 mm thick double-side polished sapphire substrate. A thin layer of SiO_2 coating with a thickness of about 650 nm was coated on the sapphire substrate to enhance the emissivity of ITO coating [75-76]. Plasma-Enhanced Chemical Vapor Deposition (PE-CVD) and Physical Vapor Deposition (PVD) nano-fabrication techniques were used to deposit the SiO_2 and ITO layers on the substrate, respectively.

Sapphire was chosen as substrate due to its high transmissivity in the optical and IR wavelength range (0.2-5.5 μm). ITO was chosen as heating element material because of its low transmissivity in the IR wavelength range and high transmissivity in the optical wavelength range. SiO_2 was chosen because of its high transmissivity in the optical wavelength range and ability to enhance emissivity [75-76]. These features allowed for the use of IR thermal imaging and high speed optical imaging techniques during heat transfer experiments. Due to the thin thickness (less than 1 μm) of the ITO-

SiO_2 bi-layer, the temperature drop across the bi-layer is assumed to be negligible. The IR camera was able to measure the temperature at the solid-liquid interface using the bi-layer substrate.

The dimensions of the sapphire substrate were 15 mm × 10 mm and the effective heating area was about 10 mm × 10 mm after two copper foil electrodes were attached to the edge of the heater surface. Power was supplied using a 1500 W power supply Lambda GEN600-2.6 with accuracy of about ± 0.6 V for voltage and ± 0.008 A for current, resulting an accuracy of heat flux of about 5% of rated value. The power supply was controlled by a computer through a serial communication port using Microsoft Hyper Terminal software. Heat flux values were calculated based on the power supplied to the heater after taking into account heat losses [54].

3.1.3. Data acquisition system

A high speed camera (Photron SA3) was used to capture the images of the droplet trains and droplet impingements given the high frequency of droplet generation and impingement events. The frame rate of the camera ranged from 60 fps (frames per second) with a resolution of 1024 × 1024 pixels to 60,000 fps with a reduced resolution of 128 × 16 pixels. High magnification zoom lenses (Navitar zoom 6000 series lenses) were used together with the camera to provide pixel pitch (i.e. pixel resolution) of 0.92-7.81 μm/pixel. The diameters of the droplets were measured by counting the number of pixels that completely fell within each droplet. Droplet velocities were calculated by taking into account inter-droplet spacing in the same droplet train, and droplet

impingement frequency [54]. Uncertainties of measured droplet diameter and droplet velocity are about 3%. Typical images for droplet property measurements are shown in Fig. 9.

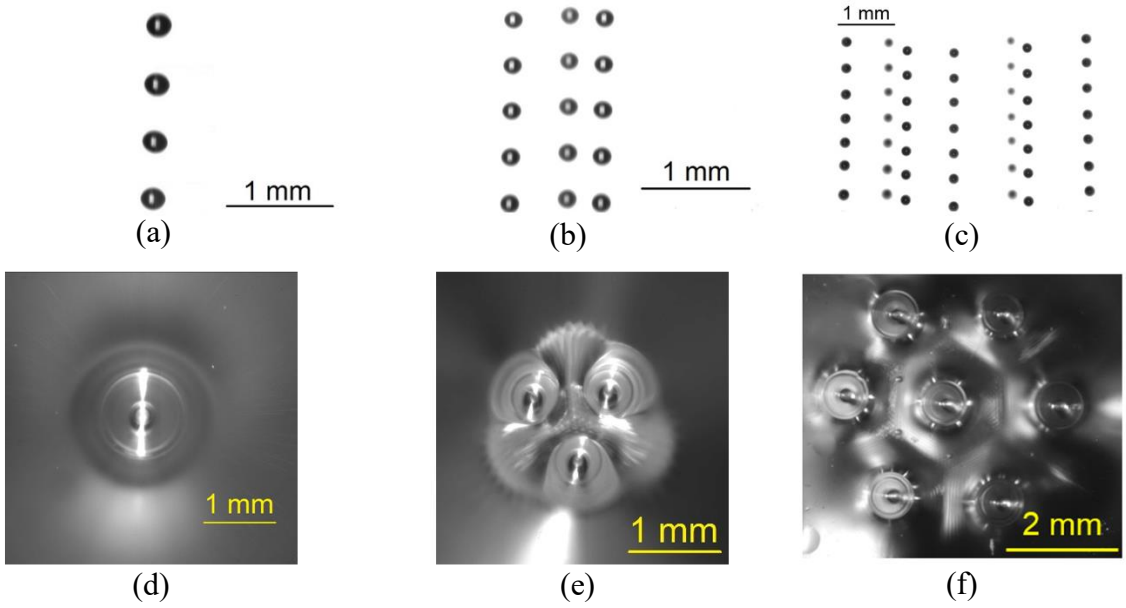

Fig. 9. Images of (a) single, (b) triangulated triple, and (c) hexagonal-arranged seven droplet trains and bottom view of (d) single, (e) triple and (f) hexagonal droplet train impingement

Angled and bottom views of the droplet train impingement process on the heater surface are shown in Fig. 10 and 11, respectively, as follows:

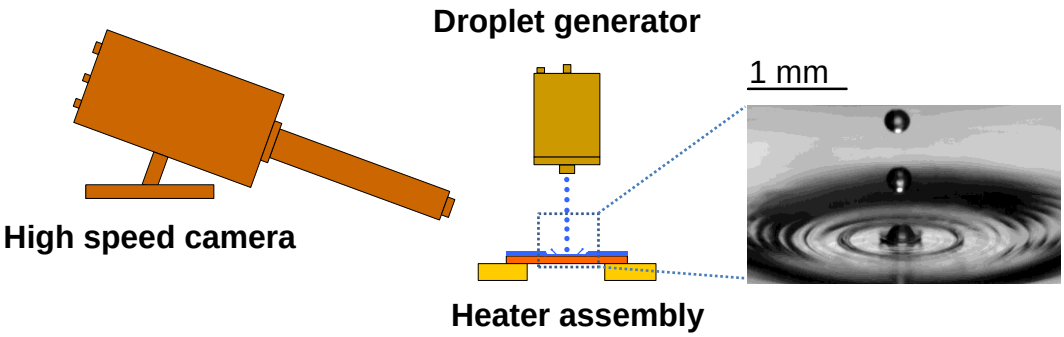

Fig. 10. Angled view of droplet train impingement

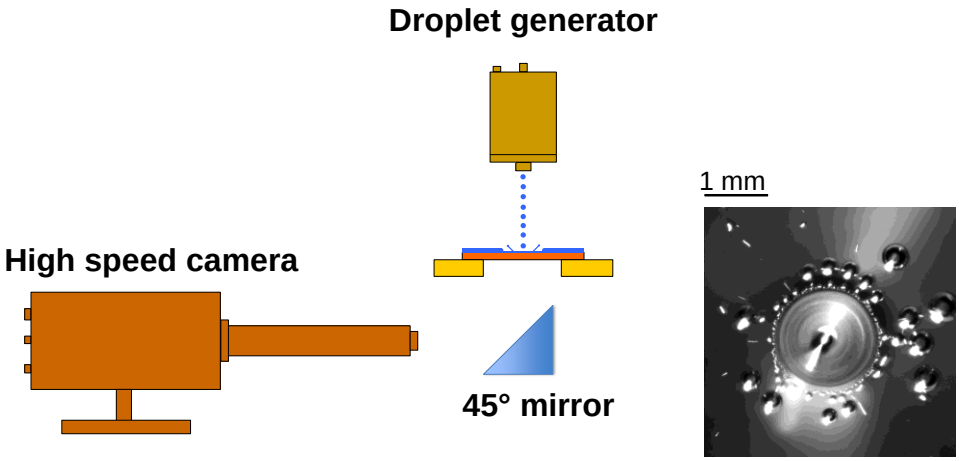

Fig. 11. Bottom view of droplet train impingement

As shown in Fig. 10, the high speed camera was placed at a tilted 20º view angle with respect to the horizontal plane to be able to observe the droplet impingement zone from above of the heater. In Fig. 11, a 45º mirror was placed below the heater to be able to observe droplet impingement dynamics during successive droplet impingements.

A polished stainless-steel rod with a curved surface was also used for crown propagation analysis for single droplet train impingement. The purpose of using a curved

surface was to avoid the accumulation of liquid outside the impact crater zone, which could block the view of the crown during the impingement process. The effects of surface curvature on crown propagation was found to be negligible (see Section 4.1.1 for detailed information about the droplet impingement process). A typical droplet-induced crown image is shown in Fig. 12.

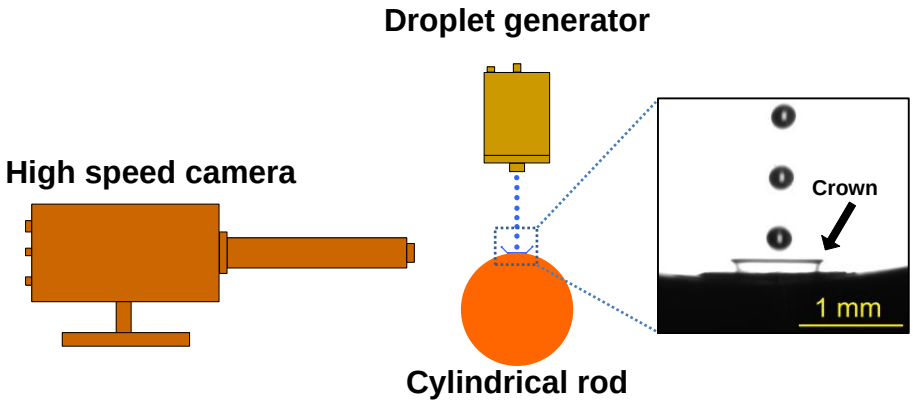

Fig. 12. Droplet-induced crown image

The surface temperatures of the heater were measured by using an IR camera (FLIR SC7650 E, with accuracy of temperature measurement of ± 1 ºC after calibration) located below the heater. The IR camera was calibrated following a detailed calibration process and recommendations found in the literature [77]. The spectrum range of the IR camera was 3.7-5.1 µm. which falls inside the IR wavelength range of the sapphire substrate (0.2-5.5 µm). The resolution of the IR camera was 640 × 510 pixels with a pixel pitch of 25 µm/pixel. When the temperature values within the area of interest were

steady, IR images were recorded at a speed of 60 fps (frames per second) for 3 s, resulting in 180 individual IR images. Given the high frequency of droplet impingement and relatively low frame rate of the IR camera, time-averaged temperature data were obtained by using developed MATLAB codes [54] for heat transfer analysis. Typical IR images are shown in Fig. 13. As shown in Fig. 13, heat transfer was most effective within the impact crater zone. Furthermore, impact crater zones are well-distinguished within the IR images due to lower surface temperatures.

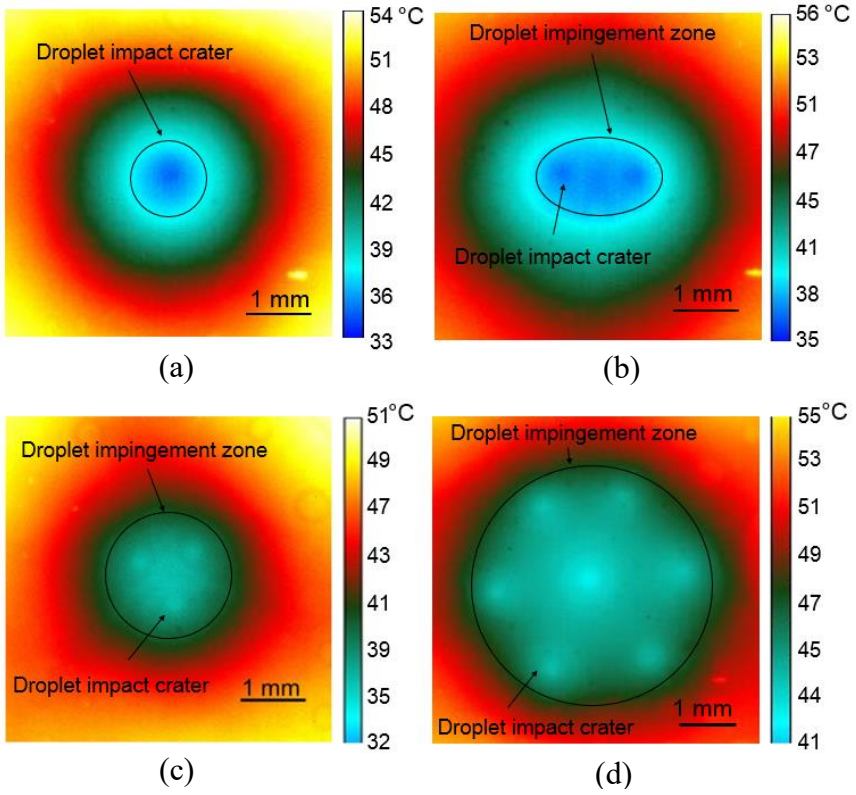

Fig. 13. IR images of heater surface under (a) single droplet train impingement, (b) double droplet train impingement, (c) triangulated triple droplet train impingement, and (d) hexagonal-arranged droplet train impingement at moderate heat flux conditions

3.2. Experimental uncertainty analysis

In this section, experimental uncertainties of surface temperature, heat flux and droplet properties, are presented and discussed, as shown below.

3.2.1. Emissivity and temperature measurement uncertainty analysis

In this study, IR emissivity of the heater was measured following a detailed process and recommendations described in Driggers [77]. Generally, emissivity of the heater was measured using a reference tape of known emissivity (3M vinyl tape Supper 88, ε_{ref} =0.95). The setup used for emissivity measurement is shown in Fig. 14. The specific steps of emissivity measurements are summarized as follows:

- Measure the IR digital counts from the surroundings (D_{sur}). This was done by placing a reflective aluminum foil within the field of view of the IR camera and capturing an IR image of the foil.
- Attach the reference tape to an aluminum block and place the heater adjacent to the tape. Heat the aluminum block, tape and heater in an oven so their temperature is at least 35 ºC higher than the ambient temperature.
- Take the heater, together with the tape and aluminum block out of the oven quickly. Place the heater and the tape within the field of view of the IR camera and capture an IR image of the heater and the tape. Measure the IR digital counts from the heater (D_{htr}) and the reference tape (D_{ref}).

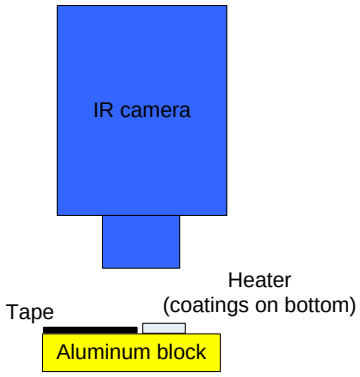

Fig. 14. Emissivity measurement setup

By using the methodologies described above, IR emissivity of the heater can be calculated using Equation 18 [77], as follows:

$$\varepsilon_{htr} = \frac{D_{htr} - D_{sur}}{D_{ref} - D_{sur}} \varepsilon_{ref} \tag{18}$$

The calculated emissivity of the heater is shown in Fig. 15.

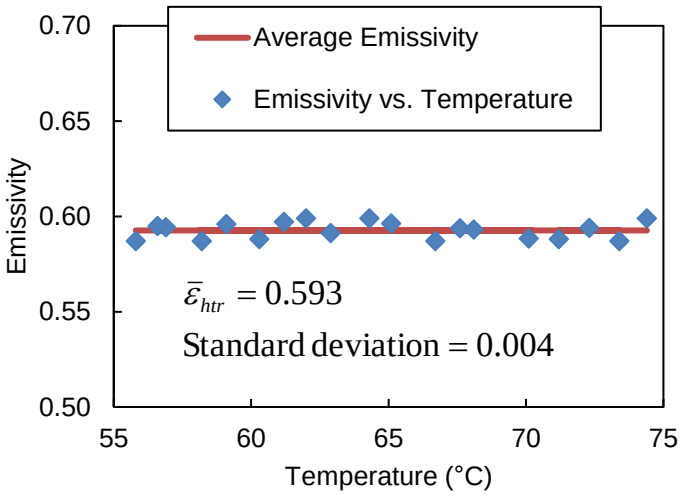

Fig. 15. Emissivity of heater at different temperatures

As shown in Fig. 15, the measured emissivity of the heater is almost constant within the temperature range of 55-75 ºC. Emissivity of the heater at lower temperatures (30-55 ºC) were not measured due to the limitations of the emissivity measurement methodology [77]. As described in Driggers [77], the target for emissivity measurements should be heated so its temperature is at least 35 ºC higher than the ambient temperature. In this work, it is assume that the emissivity of the heater is a constant within the temperature range of interest (30-65 ºC).

IR temperature measurement validation experiments were also conducted using a thin film thermocouple (OMEGA Type T Cement-On Surface Thermocouple, thickness = 13 μm, accuracy ± 1 ºC). The setup used for validation is shown in Fig. 16.

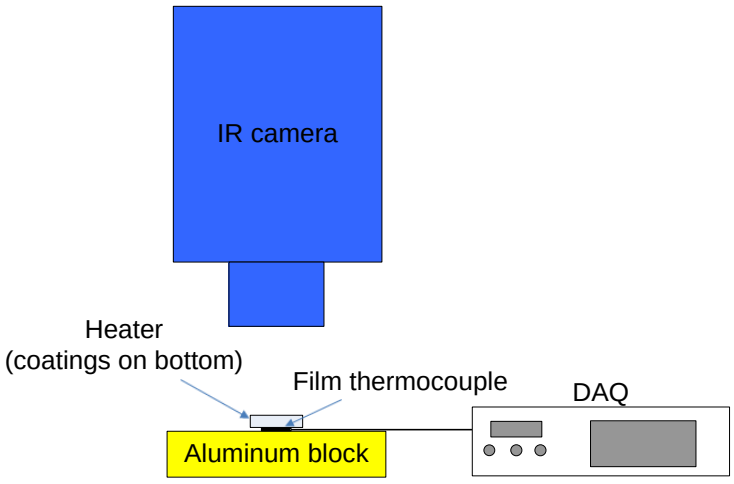

Fig. 16. Setup for IR temperature measurement validation

As shown in Fig. 16, the film thermocouple was placed between the heater and the aluminum block. The heater and aluminum block were heated in an oven to desired temperatures (30-65 ºC). Temperatures measured by using the film thermocouple and IR camera are shown in Table 2, as follows:

Table 2. Temperatures measured by film thermocouple and IR camera

Thermocouple (ºC)	IR camera (ºC)	Difference (ºC)
63.9	65.3	-1.4
62.8	64.3	-1.5
62.1	63.4	-1.3
58.1	59.5	-1.4
53.3	54.3	-1
50.4	51.5	-1.1
48.4	49.3	-0.9
46.0	46.6	-0.6
42.0	42.5	-0.5
39.4	40.1	-0.7
37.5	38.1	-0.6
36.5	37.1	-0.6

As shown in Table 2, the differences between temperature measurements by IR camera and thermocouple are within 1.5 ºC, which is very close to the uncertainties of both instruments (± 1 ºC). Moreover, the thermocouple readings were always lower than the IR readings, which may be attributed to the fin-effect of the thermocouple [78]. As a result, temperature measurements by the IR camera may be regarded as accurate.

In this study, each droplet impingement heat transfer experiment was repeated three times to obtain average temperature values. Standard deviations of the

measurements were about 0.5 ºC for each case considered. The temperature measurement accuracy of the IR camera was ± 1 ºC. As a result, the total uncertainty of temperature measurement was about ± 1.5 ºC.

3.2.2. Heat flux measurement and uncertainty analysis

Heat flux was calculated by taking into account the power supplied to the heater and heat losses to the surrounding [54], as follows:

$$q'' = \frac{\left(I \cdot V - q_{loss}\right)}{A_{htr}} \tag{19}$$

In Equation 19, *I* and *V* stand for the current and voltage supplied to the heater, A_{htr} is the area of the heater (10 mm ×10 mm) and q_{loss} is the heat losses to the surroundings. Heat losses were measured when no cooling liquid was applied to the heater. Averaged heater surface temperatures $\left(\overline{T}_{htr}\right)$ were measured to determine the heat losses. Fig. 17 shows a linear correlation of heat losses as a function of average heater surface temperature. In this work, heat losses are about 10% of total power input to the heater.

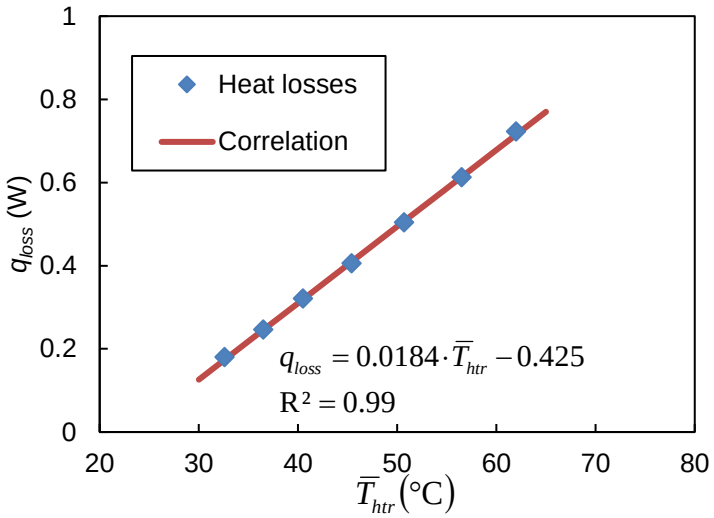

Fig. 17. Heat losses as a function of average heater surface temperature

The uncertainty of heat flux was determined using the methodology developed by Kline and McClintock [79], as follows:

$$E_{q''} = \sqrt{\left(\frac{\partial q''}{\partial I} \cdot E_I\right)^2 + \left(\frac{\partial q''}{\partial V} \cdot E_V\right)^2 + \left(\frac{\partial q''}{\partial \overline{T}_{htr}} \cdot E_{\overline{T}_{htr}}\right)^2} \quad (20)$$

In Equation 20, E_I is the uncertainty of current, E_V is the uncertainty of voltage and $E_{\overline{T}_{htr}}$ is the uncertainty of heater surface temperature. The values of E_I, E_V and $E_{\overline{T}_{htr}}$ are 0.008 A, 0.6 V, and 1.5 ºC, respectively. Based on Equation 20, $E_{q''}$ is about 5% of rated value.

3.2.3. Droplet properties measurement and uncertainty analysis

The image analysis tool from ImageJ software was used to measure the droplet properties, such as droplet diameter, droplet impingement velocity and droplet Weber

number. Pixel resolution was fixed at 3.94 μm/pixel for droplet properties measurement. Droplet diameter and impingement velocity were determined using Equations 21 and 22, respectively.

$$d_d = \sqrt{\frac{4 \cdot A_d}{\pi}} = \sqrt{\frac{\pi(a \cdot b)}{\pi}} = \sqrt{a \cdot b} \tag{21}$$

$$V_d = S_{in} \cdot f \tag{22}$$

In Equation 21, A_d stands for the projected area of droplet. a and b represent the length of the droplet in normal and horizontal directions, respectively. In Equation 22, S_{in} stands for inter-droplet spacing and f represents droplet impingement frequency. Definitions of a, b and S_{in} are shown in Fig. 18, as follows:

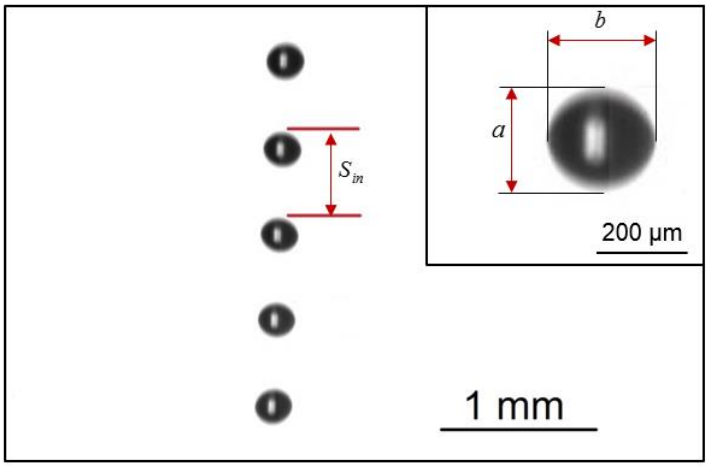

Fig. 18. Definitions of a, b and S_{in}

In this work, each droplet property measurement experiment was repeated for at least five times to obtain the average values of d_d and V_d. The experimental uncertainty of droplet diameter $\left(E_{d_d}\right)$ and droplet impingement velocity $\left(E_{V_d}\right)$ could be determined using Kline and McClintock method [79], as follows:

$$E_{d_d} = \sqrt{\left(\frac{\partial d_d}{\partial a} \cdot E_a\right)^2 + \left(\frac{\partial d_d}{\partial b} \cdot E_b\right)^2} \tag{23}$$

$$E_{V_d} = \sqrt{\left(\frac{\partial V_d}{\partial S_{in}} \cdot E_{S_{in}}\right)^2 + \left(\frac{\partial V_d}{\partial f} \cdot E_f\right)^2} \tag{24}$$

In Equation 23, E_a and E_b stand for the uncertainties of a and b, respectively. The values of E_a and E_b are about 8 μm. In Equation 24, $E_{s_{in}}$ and E_f represent the uncertainties of S_{in} and f, respectively. $E_{S_{in}}$ is about 15 μm and E_f equals to 10 Hz. Based on Equations 23 and 24, E_{d_d} and E_{V_d} are about 3% of rated values.

Droplet Weber number $\left(We = \frac{\rho d_d V_d^2}{\sigma}\right)$ and Reynolds number $\left(\mathrm{Re} = \frac{V_d d_d}{\nu}\right)$ were calculated based on droplet properties and thermal physical properties of HFE-7100. Uncertainties of We and Re were determined using Kline and McClintock method [79] while assuming ρ, σ and ν to be constant, as follows:

$$E_{We} = \sqrt{\left(\frac{\partial We}{\partial d_d} \cdot E_{d_d}\right)^2 + \left(\frac{\partial We}{\partial V_d} \cdot E_{V_d}\right)^2} \tag{25}$$

$$E_{\mathrm{Re}} = \sqrt{\left(\frac{\partial \mathrm{Re}}{\partial d_d} \cdot E_{d_d}\right)^2 + \left(\frac{\partial \mathrm{Re}}{\partial V_d} \cdot E_{V_d}\right)^2} \tag{26}$$

Based on Equations 25 and 26, the uncertainties of droplet Weber number and Reynolds number are about 5% of rated value.

3.2.4. Crown and crater diameters measurement and uncertainty analysis

The image analysis tool from ImageJ software was used to measure the diameters of time-dependent crown diameter and quasi-steady crater diameter. Pixel resolution was fixed at 3.94 μm/pixel for crown and crater measurement. Fig. 19 shows the definitions of crown rim diameter $\left(d_{c,rim}\right)$, maximum crown rim diameter $\left(d_{c,rim,\max}\right)$ and crater diameter $\left(d_{cra}\right)$.

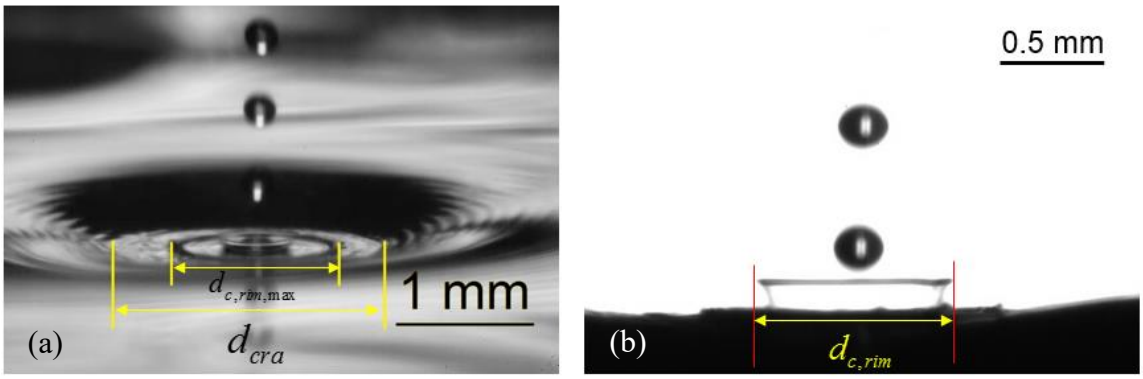

Fig. 19. Definitions of (a) $d_{c,rim,max}$, d_{cra} , and (b) $d_{c,rim}$

In this work, each crown and crater diameter measurement experiment was repeated for at least five times to obtain the average values. The uncertainties of $d_{c,rim,\max}$, d_{cra} and $d_{c,rim}$ are about 50 μm, 80 μm and 4 μm, respectively.

CHAPTER IV

RESULTS AND DISCUSSIONS*

In this chapter, experimental results of single and multiple droplet train impingements are presented and analyzed based on the study objectives and goals. Crown propagation dynamics induced by single droplet train impingement is presented. The effect of droplet-induced spreading-splashing transition on surface heat transfer is discussed and analyzed. Hydrodynamics and heat transfer induced by double and triangulated triple droplet train impingement are presented as well. Thermal performance of the hexagonal droplet train impingement arrays are analyzed and discussed as well. Comparison between circular jet impingement and droplet train impingement are also presented for various impingement patterns to understand the effects of high frequency droplet impingement on thermal performance.

4.1. Results and analysis of single droplet train impingement

In this section, results from single droplet train impingement experiments are reported and analyzed. The effects of single droplet train impingement on crown propagation dynamics, spreading-splashing transition and surface heat transfer are described and analyzed, as shown below.

---

* Parts of this chapter are reprinted from "Numerical and experimental investigations of crown propagation dynamics induced by droplet train impingement" by Taolue Zhang et al., 2016. *Intl. J. Heat & Fluid Flow*, 57, 24-33, Copyright [2016] by Elsevier, and "Effects of High Frequency Droplet Train Impingement on Spreading-Splashing Transition, Film Hydrodynamics and Heat Transfer" by Taolue Zhang et al., 2016. *J. Heat Transfer*, 138, 020902, Copyright [2016] by ASME.

4.1.1. Crown propagation dynamics induced by single droplet train impingement

Impinging droplets generated by the piezoelectric droplet generator were imaged using the high speed imaging system described in Section 3.1. Table 3 shows a summary of droplet properties, such as droplet diameter, droplet impingement velocity and droplet Weber number. Orifice diameter was fixed at 150 μm for all the cases shown in Table 3.

Table 3. Droplet properties used for crown propagation analysis

Input variables			Experimental values			
Case No.	Q (mL/h)	f (Hz)	d_d (μm)	V_d (m/s)	We	Re_{d_d}
1	165	6000	240 ± 6	3.23 ± 0.06	280 ± 13	1938 ± 60
2	180	6300	237 ± 7	3.52 ± 0.06	328 ± 15	2086 ± 71
3	195	6400	252 ± 5	3.77 ± 0.08	400 ± 19	2375 ± 69
4	210	6500	249 ± 5	3.99 ± 0.07	443 ± 18	2484 ± 66
5	225	7200	260 ± 7	4.45 ± 0.09	575 ± 28	2893 ± 97

As Table 3 shows, the droplet impingement frequency was relatively high and within the range of 6000-7200 Hz. Droplet diameter was about 250 μm. Droplet Weber number ranged from about 270 to 600.

Images for the investigation of the relationship between droplet-induced crater and crown are shown in Fig. 20. As it can be observed in Fig. 20, the droplet-induced crown propagates radially outward until it reaches a maximum diameter ($d_{c,rim,max}$), which corresponds to the inner ring marked in Fig. 20. After the crown reaches the maximum diameter, the liquid continues to flow radially outward but the fluid velocity keeps decreasing. A hydraulic jump forms due to the effects of lower fluid inertia and

surface tension, which originates at d_{cra}, as shown in Fig. 20. It should be noted that crown propagation and hydraulic jump are totally different phenomena. In crown propagation phenomena, inertia is the driving force while gravity and surface tension effects are relatively negligible. Furthermore, crown propagation is used to describe the motion of the capillary waves (i.e. lamella) within the impingement zone. By contrast, in the hydraulic jump zone, gravity and surface tension effects dominate as driving mechanisms, which occurs near the crater of the impingement zone. In this study, both phenomena have been observed experimentally during the high-frequency droplet impingement experiments.

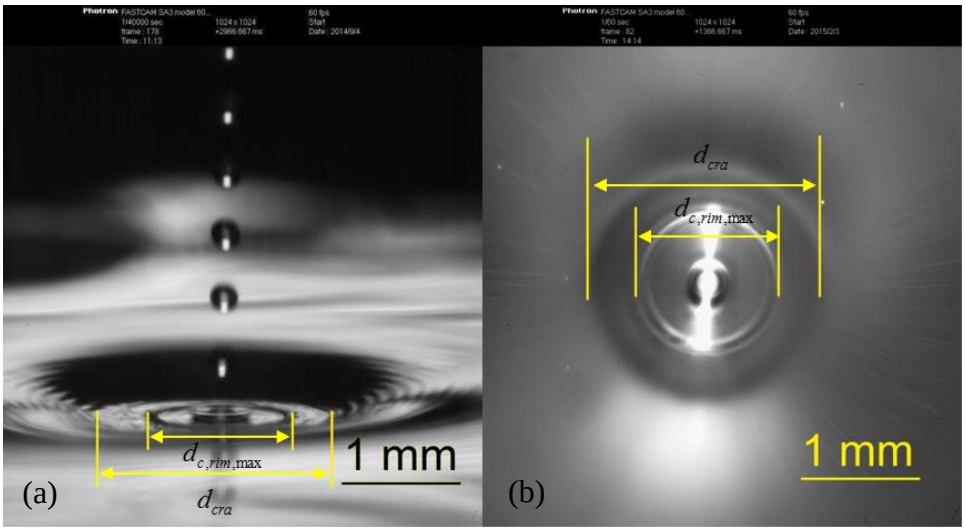

Fig. 20. (a) Angled view and (b) bottom view of single droplet train impingement at no heat flux condition

Fig. 21 shows the crater diameter as a function of maximum crown rim diameter. Measurement were made by using images like the one shown in Fig. 20. As it can be

observed in Fig. 21, crater diameter increases with droplet Weber number. Furthermore, crater diameter is almost proportional to maximum crown rim diameter, which indicates that crown propagation and crater formation induced by droplet train impingement are related to each other. As Fig. 20 shows, there is a region denoted by d_{cra} and $d_{c,rim,max}$, where the fluid seems to stagnate before reaching the hydraulic jump region.

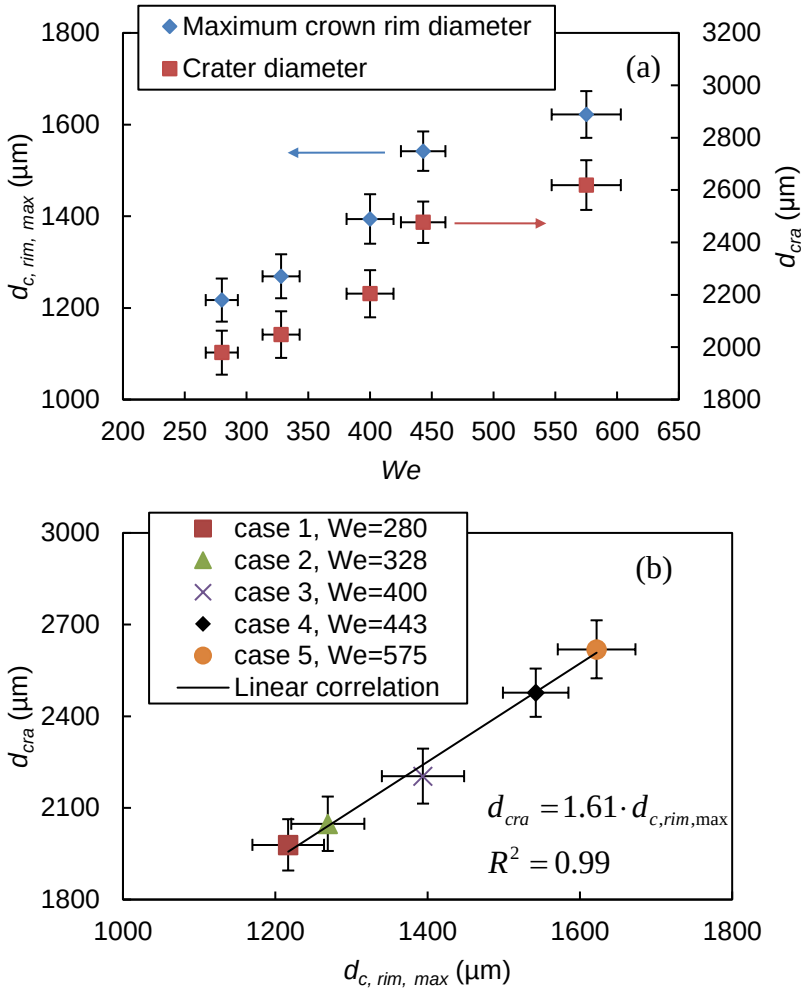

Fig. 21. (a) Crater diameter and maximum crown rim diameter as a function of Weber number, and (b) crater diameter as a function of maximum crown rim diameter at no heat flux condition

The effects of single droplet train impingement on crown propagation dynamics have also been investigated. Fig. 22 shows a group of crown propagation images at different phases during the droplet train impingement process.

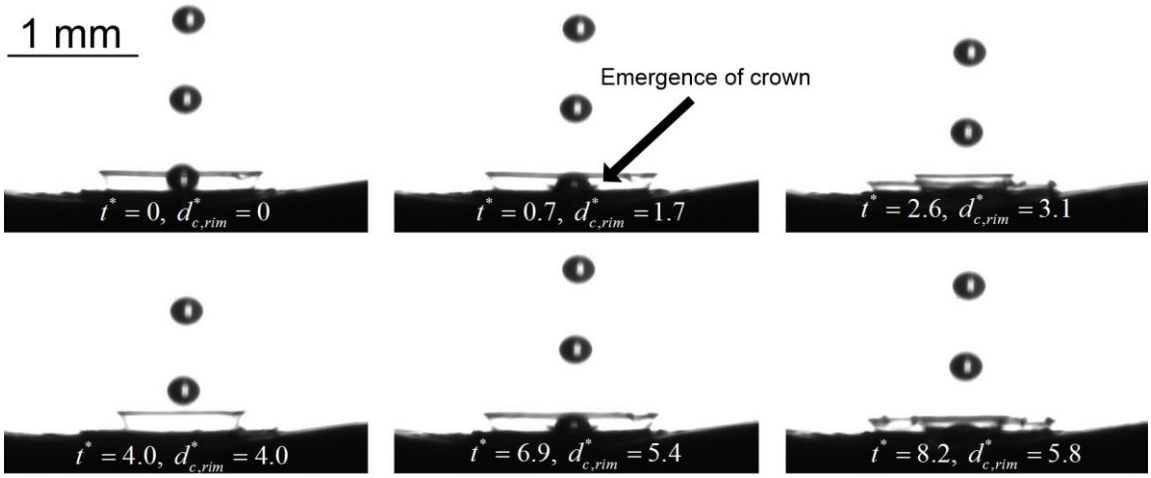

Fig. 22. Experimental crown images at different phases for case 4 in Table 3, *We* = 443

As it can be observed in Fig. 22, the time t^*=0 is defined as the moment when a droplet just touches or initially impacts the liquid film. At t^*=0.7, the crown starts to emerge and propagate radially. The diameter of the crown keeps increasing until it reaches a maximum value at about t^*=8.2. It should be noted that the shape of the crown may become irregular if splashing occurs.

As described in Section 3.1 (experimental setup section), experimental images for crown propagation analysis were captured by using the curved surface of a polished stainless steel rod (diameter = 19 mm). The purpose of using a curved surface was to avoid the accumulation of liquid outside the impact crater, which could block the view

of the crown. Since a curved surface was used for crown propagation analysis in the experiments, it became necessary to make sure that the effects of surface curvature on crown propagation were negligible. Fig. 23 shows the angled view of droplet train impingement on the curved surface of the rod.

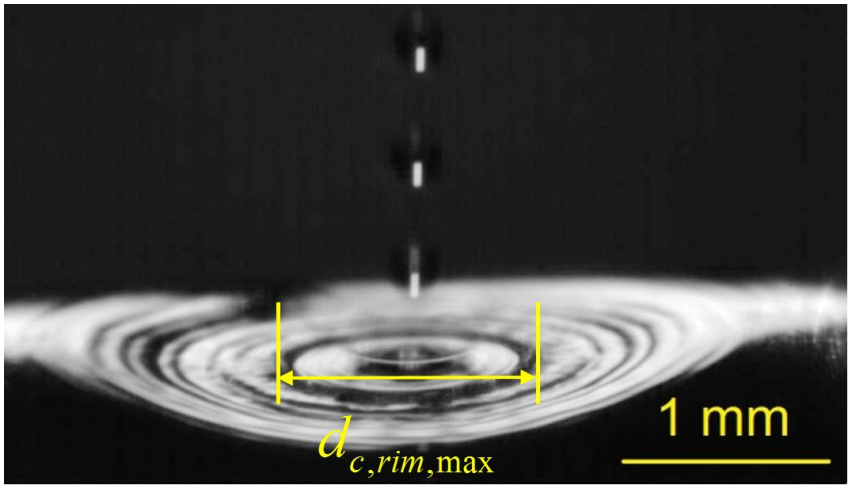

Fig. 23. Angled view of droplet train impingement on a curved surface for case 1 in Table 3, *We* = 280

As it can be observed in Fig. 23, droplet-induced crown propagates radially outward until reaches a maximum diameter ($d_{c,rim,max}$), which is similar to the crown propagation behavior observed on a flat surface. However, the liquid flow outside the region denoted by $d_{c,rim,max}$ is different from the liquid flow on a flat surface. The difference in liquid flow behavior outside the crown propagation region could be attributed to the effects of surface curvature, which avoids the accumulation of liquid

outside the crown propagation domain. However, the effects of surface curvature on crown propagation within $d_{c,rim,max}$ were found to be negligible, as described below.

Table 4 compares the maximum crown rim diameter on the translucent substrate and the curved surface, which were measured by using the images shown in Fig. 20 and 23, respectively. As shown in Table 4, the differences between maximum crown rim diameters are within 4%, which indicates that the effect of surface curvature on crown propagation is quite negligible. The effects of surface tension on crown propagation were not observed to be important due to the highly hydrophilic nature of HFE-7100 on both surfaces (static contact angle = 10º on both surfaces). However, surface tension effects may be significant if water or other liquid is used as working fluid.

Table 4. Maximum crown rim diameter measured on curved surface and translucent substrate

Case No.	Curved surface (μm)	Translucent substrate (μm)	% diff
1	1222 ± 51	1217 ± 47	- 0.4
2	1309 ± 44	1269 ± 48	3.1
3	1425 ± 43	1394 ± 54	2.2
4	1493 ± 46	1518 ± 43	-1.6
5	1651 ± 40	1622 ± 51	1.8

Fig. 24 shows the experimental and numerical crown propagation images, which the latter were obtained by Dr. Alvarado's student, Jayaveera Muthusamy. The simulations were performed using the Volume of Fluid method, which was developed by Hirt and Nichols [80]. ANSYS-Fluent was employed to simulate the droplet

impingement process due to its strong ability to solve thermal-physical problems [73-74]. Detailed descriptions of the numerical method used by Muthusamy can be found in reference [62]. The purpose of including the numerical work performed by J. Muthusamy is to provide supporting data to be able to revise the simplified Yarin and Weiss Model proposed by Yarin and Weiss [23].

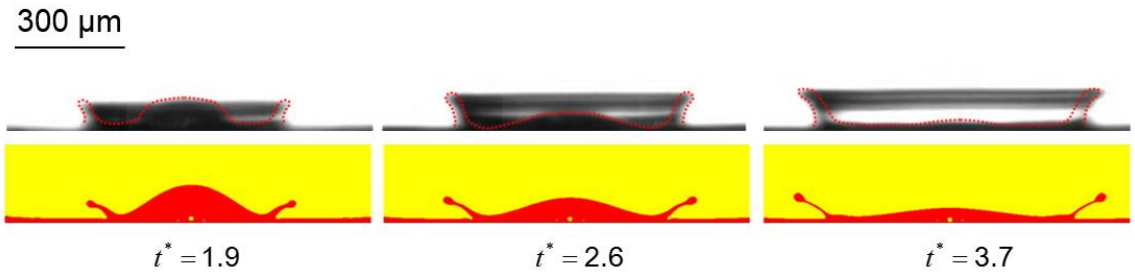

Fig. 24. Experimental crown propagation images and numerical images (from Muthusamy [62]) at different phases for case 1 in Table 3, *We* = 280

As shown in Fig. 24, reasonable agreement was reached between the simulations and the experiments in terms of liquid film morphology within the droplet-induce crown. However, for $t^* \geq 2.6$, there is a slight difference between the experimental and numerical droplet-induced crowns, which could be due to the limitations of the VOF model used to date by J. Muthusamy [62].

Fig. 25 shows the experimental time-dependent crown rim propagation curves and the corresponding numerical crown rim propagation curves. The experimental data were obtained by measuring the time-dependent crown rim diameter during five similar

crown propagation events. Uncertainty of the experimental crown rim diameter was about 4 μm (or about 0.02 for non-dimensional crown rim diameter). For the purpose of visual clarity, error bars have not been included in Fig. 25. Fitted curves and correlation equations with a mathematical form of $d^*_{c,rim} = K \cdot \left(t^*\right)^{0.5}$ are also shown in Fig. 25. As shown in Fig. 25, good agreement was reached between the numerical and experimental crown rim propagation curves, which indicate that the numerical simulations are accurate in predicting crown propagation dynamics. However, the numerical data seem slightly over-predict crown propagation diameter at $t^* > 4.0$, which is consistent with the observations made for Fig. 24. It should be noted that crown base diameter propagation curves based on numerical data have not been compared with experimental data. This is mainly because the crown base diameter is difficult to measure experimentally. As both graphs show, the *K* value is basically dependent on droplet Weber number. Table 5 shows the experimental *K* values for all the cases considered for crown propagation analysis. *K* is defined as the coefficient of crown propagation rate in this work. As shown in Table 5, the value of *K* increases with droplet Weber number.

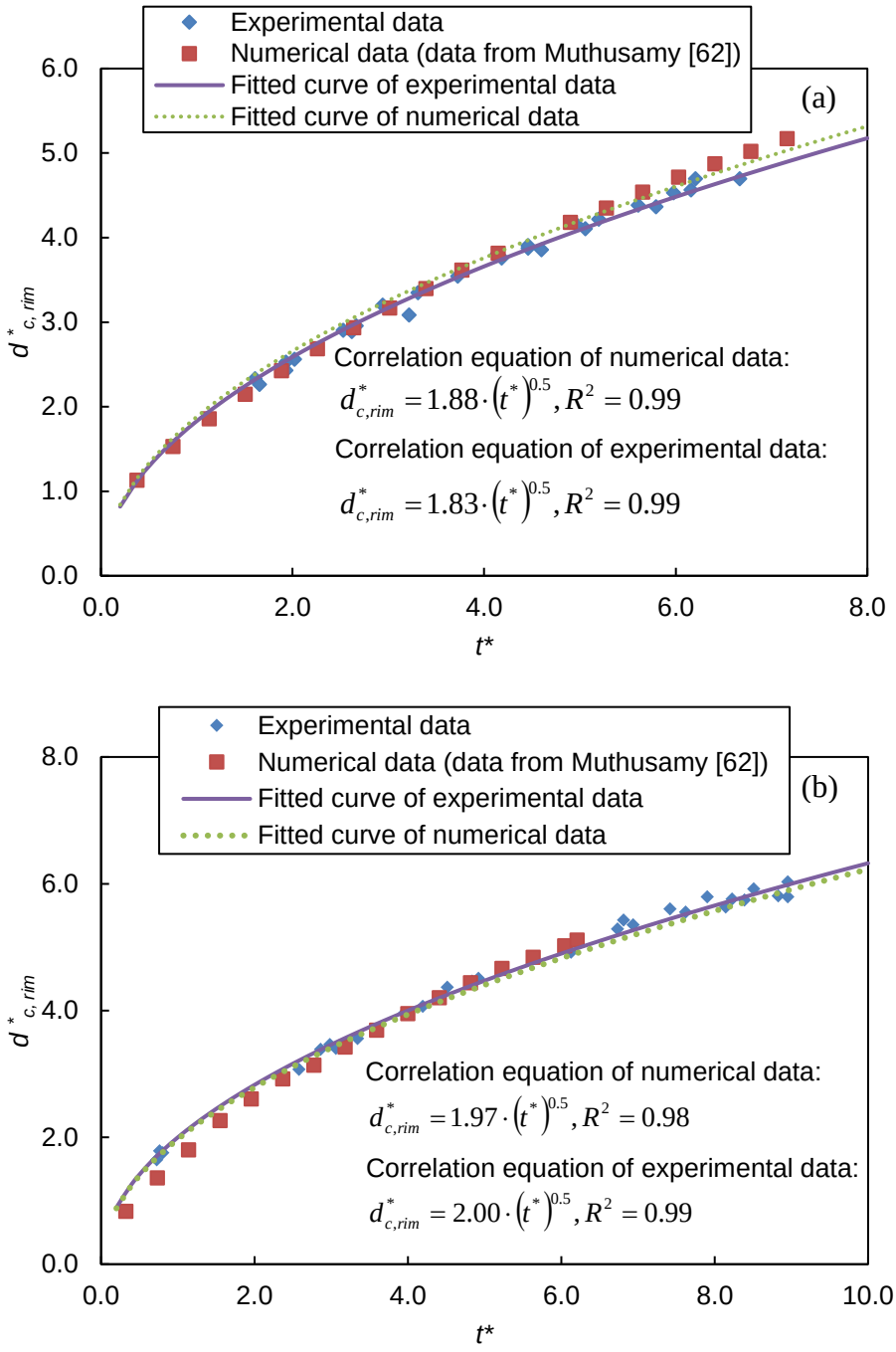

Fig. 25. Experimental crown rim propagation curves and comparison with numerical results by Muthusamy [62] for (a) case 1 in Table 3, *We* = 280 and (b) case 4 in Table 3, *We* = 443

Table 5. Experimental *K* values (i.e. coefficient of crown propagation rate) at different Weber numbers

Case No.	*Q* (mL/h)	*We*	*K*
1	165	280	1.83
2	180	328	1.92
3	195	400	1.93
4	210	443	2.00
5	225	575	2.01

The liquid film radial velocity distribution and liquid film thickness at the moment of initial spot formation (i.e. $t^* = 2.4$ for case 1 and $t^* = 2.6$ for case 4) were determined based on results by J. Muthusamy [62], as shown in Fig. 26. The initial spot formation is defined as the moment when crown base propagation velocity is equal to droplet impingement velocity [23, 26]. It can also be interpreted as the point when the vertical droplet momentum has been completely transformed to radial momentum within the liquid film.

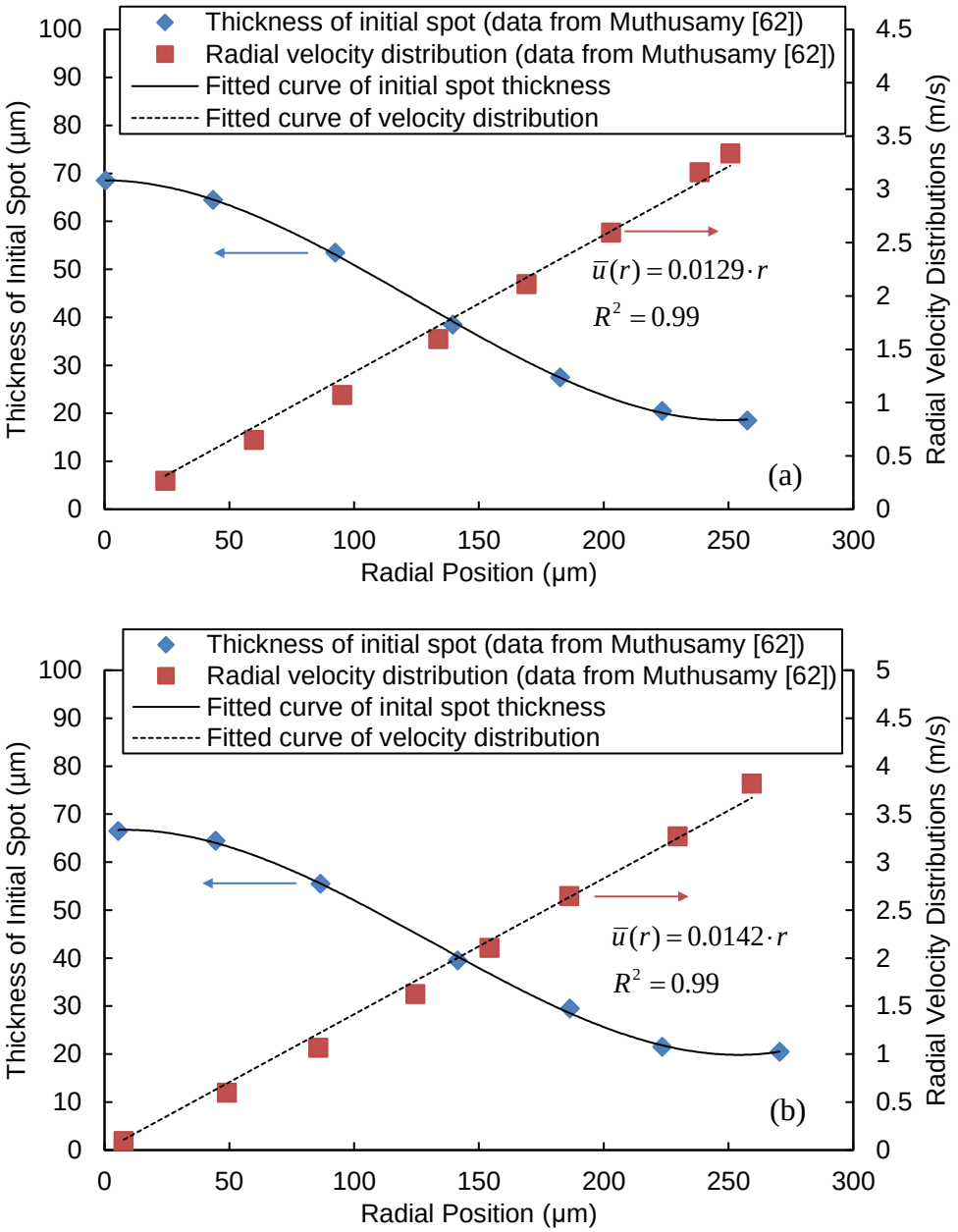

Fig. 26. Numerical liquid film thickness and radial velocity distribution within the initial spot [62] for (a) case 1 in Table 3, *We* = 280, t^* = 2.4, and (b) case 4 in Table 3, *We* = 443, t^* = 2.6

As shown in Fig. 26, the radial velocity distribution within the initial spot varies almost linearly between $\bar{u}(r) = 0$ at the center of impact to $\bar{u}(r) = V_d$ close to the crown base location, which agrees with the findings in Rieber and Frohn [26] and Shetabivash et al. [27]. As it can be seen in Fig. 26, the slope of velocity distribution depends on Weber number. A third-order polynomial equation was used to curve-fit the liquid film thickness within the initial spot, which was obtained numerically. For the cases shown in Fig. 26, the third-order polynomial equations are as follows:

$$h_{spot}(r) = 6\times10^{-6} r^3 - 0.0024\, r^2 + 0.0003\, r + 68.545,\ \mathrm{R}^2 = 0.99, We = 280 \quad (27)$$

$$h_{spot}(r) = 6\times10^{-6} r^3 - 0.0025\, r^2 + 0.0409\, r + 66.57,\ \mathrm{R}^2 = 0.99, We = 443 \quad (28)$$

As can be seen in Equations 27 and 28, the magnitude of the parameters depend on Weber number as well.

The average thickness of the initial spot was calculated based on the fitted equations (Equations 27 and 28) using Equation 29:

$$\bar{h}_{spot} = \frac{\int_0^R 2\pi \cdot r \cdot h_{spot}(r) dr}{\pi \cdot R^2} \quad (29)$$

In Equation 29, R is the radius of the initial spot formation (R=$d_{c,base}$ /2 at the moment of initial spot formation). Definition of crown base diameter can be found in reference [62] and are shown in Fig. 27.

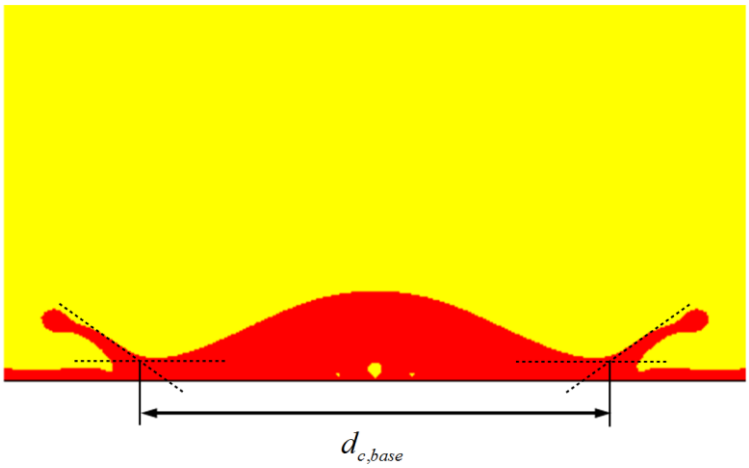

Fig. 27. Crown base diameter [62]

As shown in Fig. 27, two planes (or lines), which meet at the liquid-vapor interface, were used to determine the crown base diameter. A tangential line (or plane) with a slope of 0, which passes through the lowest point of the liquid-vapor interface, was used to determine the crown base diameter. The other tangential line is drawn parallel to the lamella side of the liquid crown at the point where it has the greatest slope value. The intersection point between both lines was used to determine crown base diameter. It should be noted that the definition of crown base diameter is not clear in Rieber and Frohn [26] and Shetabivash et al. [27]. Furthermore, in Rieber and Frohn [26] and Shetabivash et al. [27], it was found that the lamella side of the liquid crown is almost normal to the liquid film. However, in the present study, the angle between the lamella side and the horizontal plane is much smaller, as shown in Fig. 27. This is mainly due to changes in unperturbed liquid film thickness during successive impingement events, as described below.

The numerical data obtained by J. Muthusamy [62] indicate that at the moment of initial spot formation [23, 26], $\bar{h}_{spot}$ is about 30 μm while h_0 is about 10 μm. However, Rieber and Frohn [26] and Shetabivash et al. [27] found that $\bar{h}_{spot}$ is equal to h_0 at the moment of initial spot formation. This is because Rieber and Frohn [26] and Shetabivash et al. [27] studied the crown propagation induced by only a single droplet impact on thin liquid films. The value of h_0^* in Rieber and Frohn [26] and Shetabivash [27] is 0.116, where h_0^* is the non-dimensional unperturbed liquid film thickness (h_0 / d_d). However, in this study, h_0^* was much smaller due to the successive nature of the droplet impingement events, which lead to a thinner liquid film ($h_0^* \approx 0.04$). Table 6 summarizes the assumptions ($\bar{u}(r)$ equation and $\bar{h}_{spot}$ relation with h_0) made by different researchers when postulating a crown propagation model (i. e. YWM).

Table 6. Summary of assumptions made by different researchers to obtain a simplified Yarin and Weiss Model (i.e. crown propagation model)

Source	$\bar{u}(r)$	$\bar{h}_{spot}$	Droplet impingement condition
Yarin and Weiss [23]	Eq. 4	$\bar{h}_{spot} = h_0$	Droplet train impingement
Rieber and Frohn [26] and Shetabivash et al. [27]	Eq. 10	$\bar{h}_{spot} = h_0$	Single droplet impacting liquid film
Current work	Eq. 10	$\bar{h}_{spot} = 3h_0$	Droplet train impingement

Based on the velocity distribution within the liquid film, and its thickness within the initial spot, a new simplified YWM is proposed, as shown in Equation 30. Table 7 summarizes Equations 8, 12 and 30, which are the simplified YWM as proposed by different researchers, and lists the assumptions of each model.

$$d^*_{c,base} = \left[\frac{\sqrt{2} V_d^{1/2}}{6^{1/4} \left(\bar{h}_{spot}\right)^{1/4} \pi^{1/2} d_d^{1/4} f^{1/2}} \right] \left(t^*\right)^{1/2} \tag{30}$$

Table 7. Summary of simplified Yarin and Weiss Models used by different researchers

Source	Equation No.	Simplified YWM used	Assumptions
Yarin and Weiss [23]	8	$d^*_{c,base} = \left[\frac{2 V_d^{1/2}}{6^{1/4} h_0^{1/4} \pi^{1/2} d_d^{1/4} f^{1/2}} \right] \left(t^*\right)^{1/2}$	$\bar{h}_{spot} = h_0$
Rieber and Frohn [26] and Shetabivash et al. [27]	12	$d^*_{c,base} = \left[\frac{\sqrt{2} V_d^{1/2}}{6^{1/4} h_0^{1/4} \pi^{1/2} d_d^{1/4} f^{1/2}} \right] \left(t^*\right)^{1/2}$	$\bar{h}_{spot} = h_0$
Current work	30	$d^*_{c,base} = \left[\frac{\sqrt{2} V_d^{1/2}}{6^{1/4} \left(\bar{h}_{spot}\right)^{1/4} \pi^{1/2} d_d^{1/4} f^{1/2}} \right] \left(t^*\right)^{1/2}$	$\bar{h}_{spot} = 3h_0$

As shown in Table 7, Equation 12 can be obtained by simply dividing the right-hand side of Equation 8 by $2^{1/2}$. Similarly, Equation 30 can be obtained by dividing the right-hand side of Equation 12 by $3^{1/4}$. This clearly indicates that the only difference among the different YWM is a single factor or constant, which depends on values used for $\bar{h}_{spot}$ and the liquid film velocity distribution at the moment of initial spot formation.

Figure 28 shows the numerical crown base propagation curves and predictions given by different simplified YWM (Equations 8, 12 and 30) using h_0 and $\bar{h}_{spot}$ values of 10 µm and 30 µm, respectively, and the same droplet velocity, droplet diameter, impingement frequency as given in Table 3 (cases 1 and 4). As shown in Fig. 28, the simplified YWM given by Yarin and Weiss [23] (Equation 8) greatly over-predicts the time dependent crown base diameter. Rieber and Frohn [26] and Shetabivash et al. [27] reached similar conclusions when comparing their numerical crown base propagation curves with the predictions given by Yarin and Weiss [23]. This is mainly due to the assumptions associated with $\bar{u}_r$ proposed by Yarin and Weiss [23] (Equation 4) as explained in Section 2.2.2 (literature review section). Numerical results obtained by J. Muthusamy [62] are in good agreement with the predictions given by Rieber and Frohn [23] (Equation 12). However, the predictions given by Equation 12 consistently over-predicts time-dependent crown base diameter. This is because Equation 12 is based on the assumption that $\bar{h}_{spot}$ is equal to h_0. In this work, it has been determined that $\bar{h}_{spot}$ should be three times h_0 ($\bar{h}_{spot} = 3h_0$), based on the numerical results from J. Muthusamy [62]. As Fig. 27 shows, there is good agreement between the simplified YWM proposed in the current work (Equation 30) for different Weber number values.

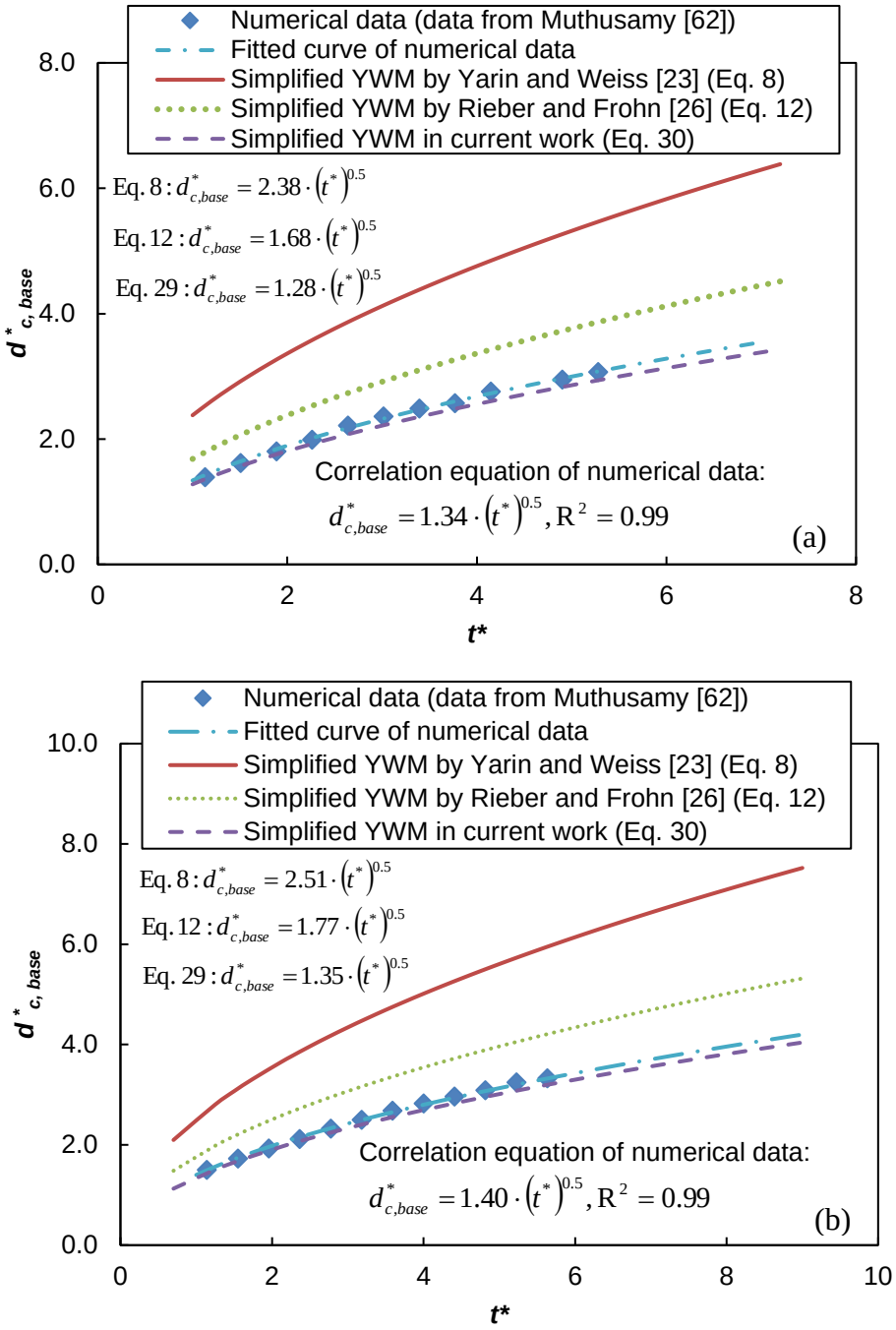

Fig. 28. Crown base propagation curves for (a) case 1 in Table 3, *We* = 280, and (b) case 4 in Table 3, *We* = 443, and predictions given by different crown propagation models

4.1.2. Spreading-splashing transition and surface heat transfer induced by single droplet train impingement

In this section, the effects of single droplet train impingement on spreading-splashing transition and surface heat transfer are presented and discussed. Droplet-induced spreading-splashing transition was investigated by adjusting droplet Weber number while holding flow rate a constant, as described below.

Droplet impingement experiments were conducted to determine droplet properties, such as droplet diameter (d_d), droplet impingement velocity (V_d) and droplet Weber number (We). Uncertainties of droplet properties were determined using the Kline and McClintock method [79], as described in Section 3.2. Table 8 shows a summary experimental droplet properties used for spreading-splashing transition analysis.

Table 8. Droplet properties for spreading-splashing transition analysis at a fixed flow rate of 165 mL/h

	Input variables		Experimental values				
Case No.	f (Hz)	d_{orf} (μm)	d_d (μm)	V_d (m/s)	V_d^*	We	Re_{d_d}
1	5,000	160	261 ± 8	2.99 ± 0.07	14.2 ± 0.3	262 ± 18	1948 ± 67
2	6,000	150	240 ± 6	3.23 ± 0.06	14.3 ± 0.2	280 ± 13	1938 ± 60
3	7,000	140	234 ± 7	3.75 ± 0.08	15.6 ± 0.2	368 ± 18	2187 ± 72
4	7,500	130	235 ± 6	4.31 ± 0.06	17.5 ± 0.3	489 ± 26	2527 ± 98
5	15,000	100	182 ± 6	6.46 ± 0.11	20.2 ± 0.3	850 ± 31	2938 ± 120

As shown in Table 8, experiments were performed at a fixed flow rate condition (165 mL/h). A set of orifice plates with different orifice diameters (d_{orf}) were used to be

able to vary droplet Weber number over a wide range of experimental conditions. Non-dimensional droplet impingement velocity (V_d^*) was determined based on Equation 13 $\left(\left(V_d^* \right)_{crt} = \left(\frac{V_d \rho^{1/4}}{\sigma^{1/4} \nu^{1/8} f^{3/8}} \right)_{crt} \right)$, which is described in Section 2.2.3 (literature review section).

Hydrodynamics of droplet-induced spreading-splashing transition have been investigated and analyzed experimentally. High speed images were taken from different angles to observe the droplet-induced spreading-splashing transition phenomena at a fixed flow rate condition. Fig. 29 shows the spreading-splashing transition phenomena at a fixed flow rate of 165 mL/h, when no heat was applied.

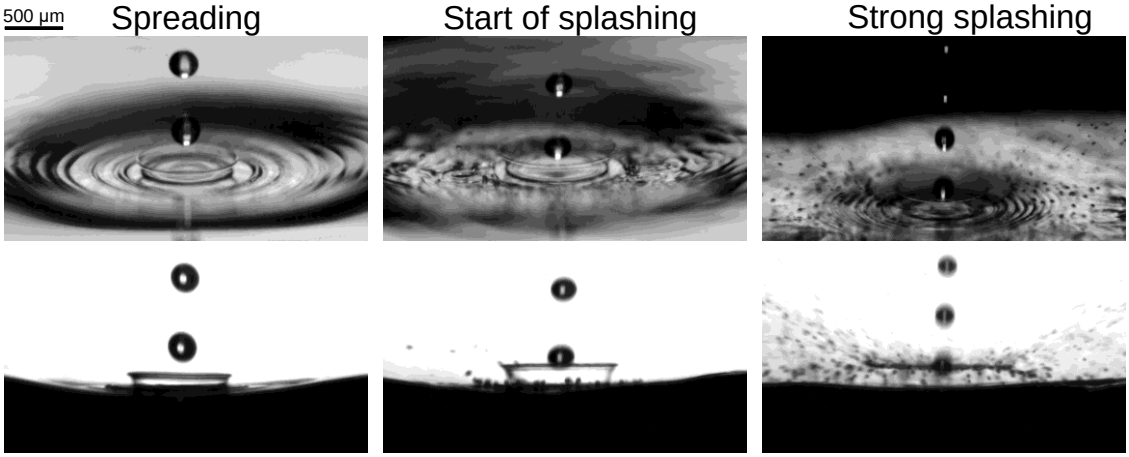

(a) Case 1, *We*=262 (b) Case 4, *We*=489 (c) Case 5, *We*=850

Fig. 29. Angled and side views of spreading-splashing transition phenomena at a fixed flow rate of 165 mL/h

As it can be observed in Fig. 29, droplet-induced crown propagation transition phenomena from spreading to splashing were observed by increasing droplet Weber number. As shown in Fig. 29 (a), droplet-induced crown spreads smoothly without the emergence of secondary droplets at a low droplet Weber number condition (Case 1 in Table 8, We = 262). At a droplet Weber number of 489, secondary droplets emerged from the crown's rim during the late crown propagation phases, which can be categorized as splashing. In this study, start of splashing was observed at a V_d^* value of 17.5 (Table 8, case 4), which is in good agreement with the empirical correlation proposed by Yarin and Weiss [23] (Equation 13 in Section 2.2.3). At a high droplet Weber number of 850, much more secondary droplets were observed during the crown propagation process. Furthermore, break-up of the crown was also observed at a high droplet Weber number of 850, which is similar to the results shown in Wang and Chen [30].

Fig. 30 shows the side views of droplet-induced crown splashing process for case 4 in Table 8. As shown in Fig. 30, the shape of the droplet-induced crown was regular and axis-symmetric during the early phases ($t^* < 5$). However, cusps start to emerge and develop during the intermediate phases ($5 < t^* < 8.5$). It was also observed that the cusps distributed almost uniformly around the free rim of the crown. During the late phases ($t^* > 8.5$), fingering, detachment and secondary droplets (i. e. splashing) were observed on the free rim of the crown.

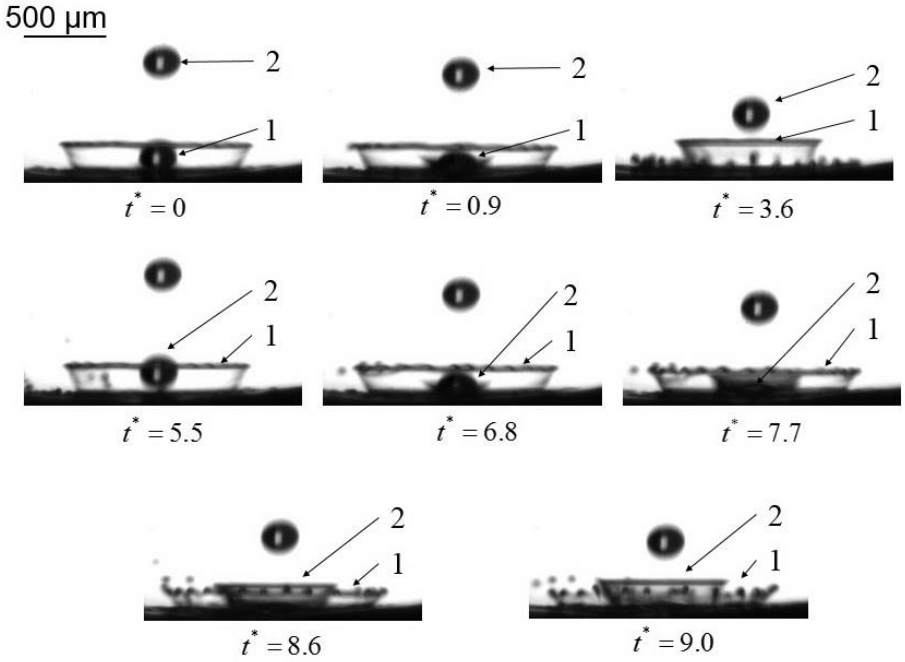

Fig. 30. Side view of splashing dynamics for case 4 in Table 8, *We* = 489

Table 9 shows the number of cusps (which become fingers and spikes at later phases) observed on the crown's rim as well as the number of cusps predicted by the Plateau-Rayleigh instability theory [32-33]. In Table 9, uncertainties of experimental values were obtained by calculating the standard deviation associated with five measurements. Uncertainties of predicted values were obtained based on Equation 15 and error propagation analysis [79]. As Table 9 shows, a reasonable agreement was reached between the experimental and predicted values. This indicates that the Plateau-Rayleigh instability theory [32-33] can be used to explain the crown splashing phenomena induced by successive droplet-liquid film interactions. Rieber and Frohn [26] and Zhang et al. [34] also claimed that Plateau-Rayleigh instability theory can be

used to explain the splashing phenomena induced by droplet-liquid film interactions. Rieber and Frohn [26] determined the number of cusps during droplet-induced splashing process numerically. They [26] found that their numerical values of the number of cusps agree well with the predicted values given by Equation 15. Zhang et al. [34] measured the spectrum of perturbations growing on droplet-induced crown experimentally, as shown schematically in Fig. 31. Zhang et al. [34] found that their experimental peak wavelength values agree well with the predicted values given by Plateau-Rayleigh instability theory [32-33].

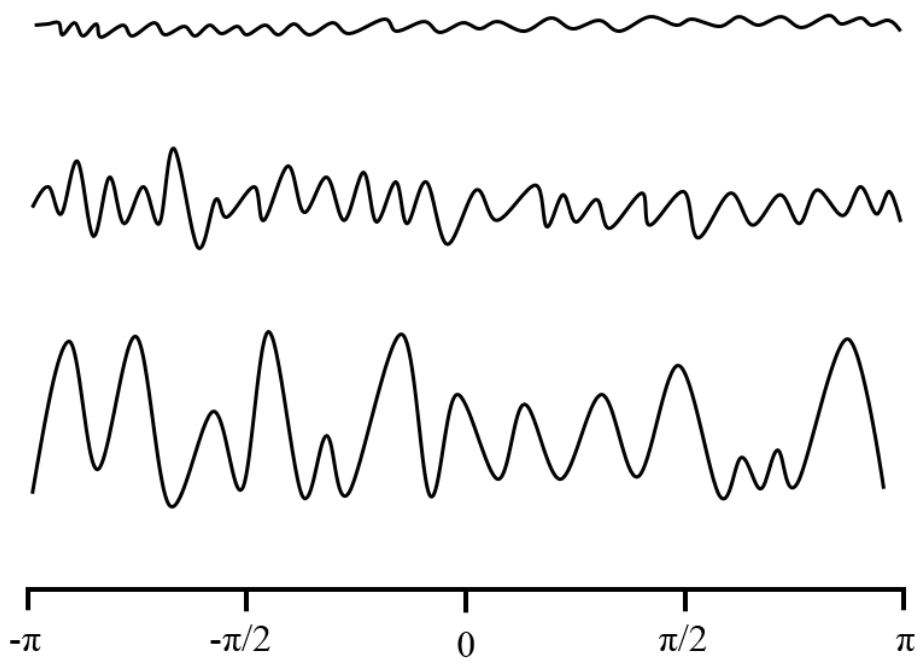

Fig. 31. Schematic diagram of the spectrum of perturbation growing on crown's rim [34], time increases from top to bottom

Yoon et al. [35] evaluated the applicability of different instability theories (Rayleigh-Taylor, Plateau-Rayleigh and Kelvin-Helmholtz instabilities) for droplet-induced splashing phenomena. Droplet-dry surfaces interactions and droplet-liquid pool interactions were considered in Yoon et al. [35], in which they claimed that fingers observed for the droplet-liquid pool interactions may not be due to the Plateau-Rayleigh instability mechanism. Yoon et al. [35] also claimed that the finger formation for droplet-solid wall interactions and droplet-liquid pool interactions can be explained in terms of shear-driven Kelvin-Helmholtz instability. However, their observations were limited to drop-pool conditions, where the depth of the pool is much larger than the droplet diameter considered in this study. In this study, the droplet diameter-liquid film thickness ratio varied in the range of 2 to 13, which suggests that surface tension effects should be taken into account in the formation of spikes and secondary droplets that have limited interactions with the thin liquid film, as explained in greater detail below.

Liu et al. [36] studied the droplet-induced splashing phenomena on dry surfaces experimentally. Liu et al. [36] claimed that the ultrathin air film trapped under the expanding liquid front triggers splashing and stated that Kelvin-Helmholtz instability provides only a mechanism for the rim formation at the edge. However, their observations reveal that rim and liquid sheet rupture during the latter stages of the droplet impingement process may involve other mechanisms such as Plateau-Rayleigh instability [36].

It should be noted that Yoon et al. [35] considered splashing when droplet impact dry surfaces and deep liquid pools. Liu et al. [36] considered splashing when droplet

impact on dry surfaces only. In contrast, Rieber and Frohn [26] and Zhang et al. [34] considered splashing when droplets impact on liquid films, which is consistent with the current work.

The different claims about the driving mechanism of droplet-induced splashing could be due to the complexity of splashing phenomena. As described above, droplet could impact on dry surfaces, liquid films or liquid pools. The associated physical mechanism at different impingement conditions could be different.

Table 9. Number of cusps at different phases

Case No.	t^*	n_{cusp}	
		Experimental	Predicted (Eq. 15)
Case 4 in Table 7	6.8	23 ± 2	28 ± 4
	7.7	28 ± 3	29 ± 4
	8.6	25 ± 2	31 ± 4

The effects of spreading-splashing transition on heat transfer were also investigated to understand the relationship between hydrodynamics and heat transfer behavior. Heat transfer experiments were conducted under the same conditions as shown in Fig. 29.

Fig. 32 shows the optical and IR images of droplet impingement zone at different heat flux and droplet Weber number conditions. The yellow and black ellipses in Fig. 32 represent the extent of the crater diameter in the optical and IR images, respectively.

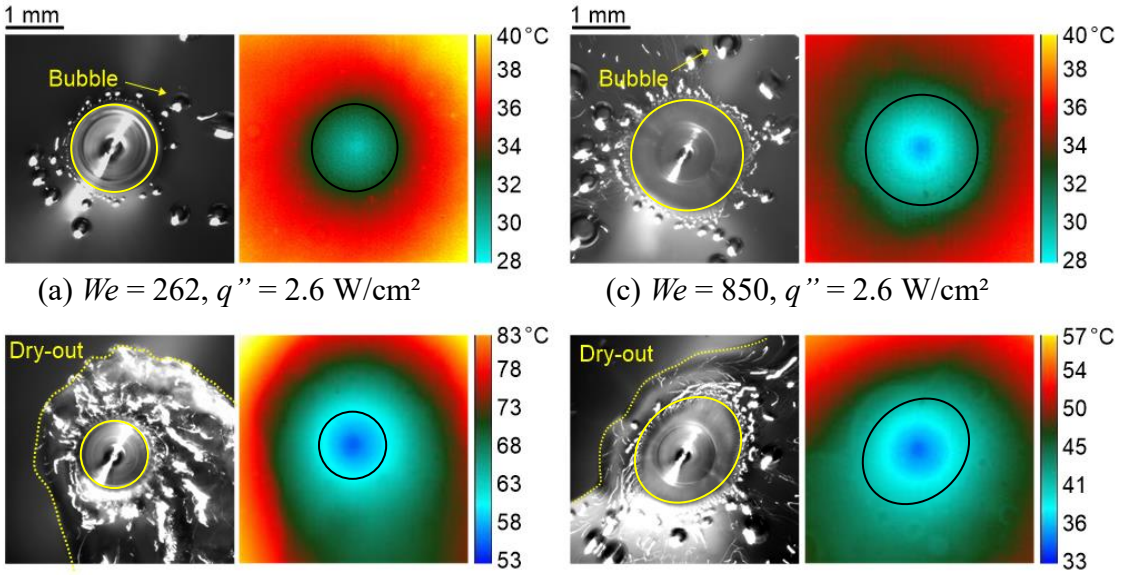

Fig. 32. Optical and IR images of droplet impingement zone for different heat flux and droplet Weber number conditions

As shown in Fig. 32, the droplet-induced liquid film could spread all over the heater surface at a heat flux of 2.6 W/cm². Dissolved air bubbles were observed outside the impact craters at a heat flux of 2.6 W/cm², as shown in Fig. 32(a) and 32(c). Nucleate boiling and asymmetric dry-out were observed outside the impact craters at a heat flux of 4.8 W/cm², as shown in Fig. 32 (b). A similar asymmetric dry-out was observed when circular jets impinged on hydrophobic surfaces, as revealed by Maynes et al. [81]. In the current work, the heater surface is hydrophilic to the cooling liquid at room temperature. However, as shown in Chandra and Avedisian [82] and Qiu et al. [83-85], the heater surface could depict apparent high contact angle to the cooling liquid at high surface temperatures, which lead to bubble nucleation and growth resulting in an apparent

thicker liquid film. The asymmetric dry-out observed in the current work could be due to changes in apparent contact angle when surface temperature increases. Furthermore, it was observed that crater diameter decreases with heat flux, as depicted in Fig. 32(a) and 32(b). Fig. 33 through 35 show the effects of heat flux on crater diameter (d_{cra}), maximum crown rim diameter ($d_{c,rim,max}$) and the temperature at the location of maximum crown rim diameter ($T(r = r_{c,rim,max})$).

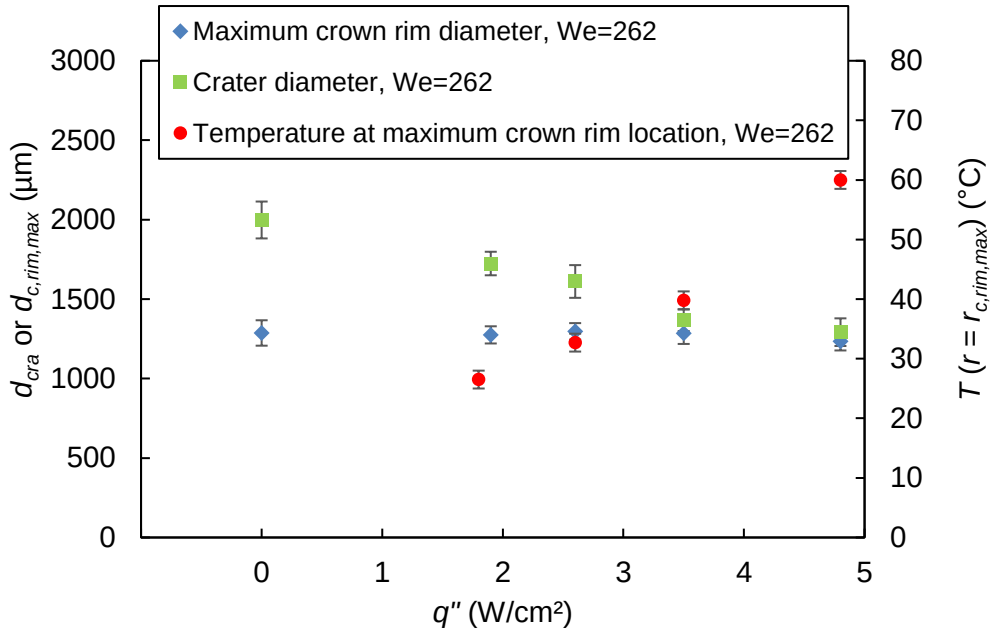

Fig. 33. Effects of heat flux on crater diameter, maximum crown rim diameter and temperature at maximum crown rim location, *We* = 262, *Q*=165 mL/h

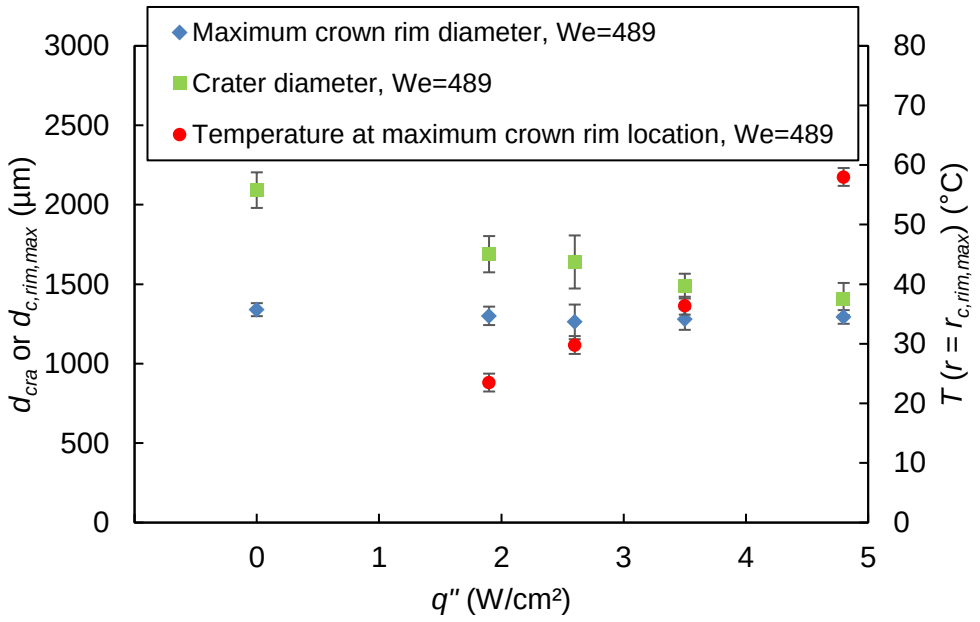

Fig. 34. Effects of heat flux on crater diameter, maximum crown rim diameter and temperature at maximum crown rim location, *We* = 489, *Q*=165 mL/h

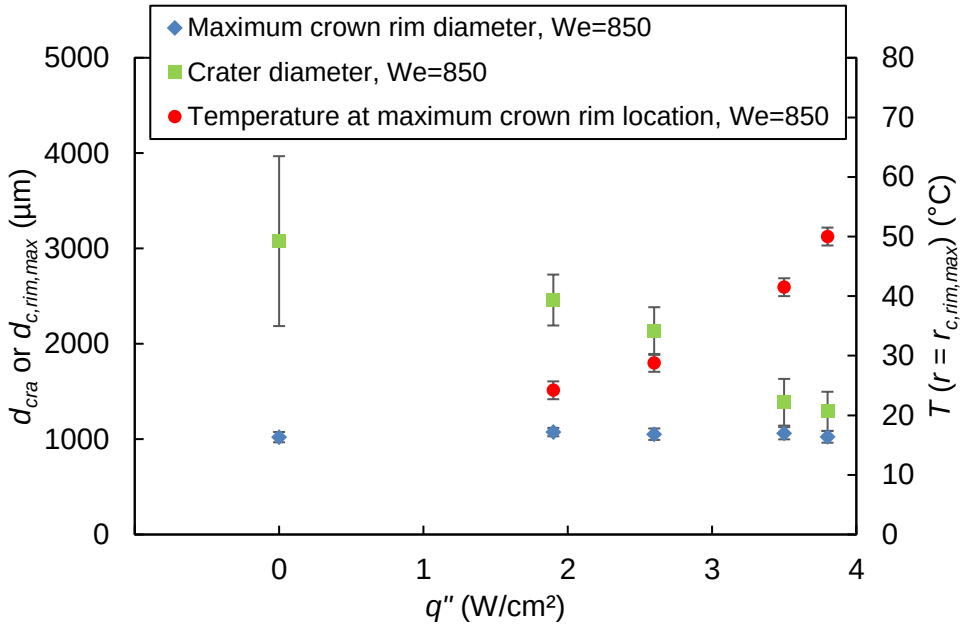

Fig. 35. Effects of heat flux on crater diameter, maximum crown rim diameter and temperature at maximum crown rim location, *We* = 850, *Q*=165 mL/h

As shown in Fig. 33 through 35, crater diameter decreases with heat flux at different droplet Weber number conditions, which is consistent with the results shown in Soriano et al. [55]. The reduction of crater diameter with heat flux can be attributed to the formation of dissolved air bubbles, vigorous nucleate boiling and formation of dry out area surrounding the impact crater zone [55], which confines the extension of the crater. At high Weber number, the crater diameter fluctuates more than at low Weber number, as shown in Figures 35 and 33-34, respectively. The crater diameter fluctuation is associated with the instabilities present during the rigorous splashing process. In contrast, the maximum crown rim diameter was found to be relatively independent of heat flux, which could be due to the high fluid inertia during the crown propagation process. Temperature measurements show that surface temperature was lower than the saturation point (61 °C) at the maximum crown rim location. This indicates that single phase forced convection was the primary heat transfer mechanism within the crown propagation region even at high heat flux conditions [55].

The effects of spreading-splashing transition phenomena on heat transfer were investigated by measuring the time-averaged surface temperatures within the droplet impingement zone. Fig. 36 shows the heat-flux surface temperature curves at different droplet Weber number conditions. As shown in Fig. 36, the heat flux-surface temperature curves are relatively linear before the start or on-set of dry-out, which indicates that single phase forced convection was the primary heat transfer mechanism. However, a sharp increase in surface temperature was observed when dry-out appeared on the heater surface. Furthermore, it was found that higher Weber number was more

favorable for heat transfer at low heat flux conditions (q'' < 3 W/cm²). However, strong splashing (*We* = 850) was unfavorable for heat transfer at high heat flux conditions (q'' > 3 W/cm²). This could be attributed to the instability of the liquid film under strong splashing conditions, which lead to the onset of dry-out even at lower heat flux values. In summary, results show that droplet Weber number plays significant roles in droplet-induced film hydrodynamics and heat transfer performance.

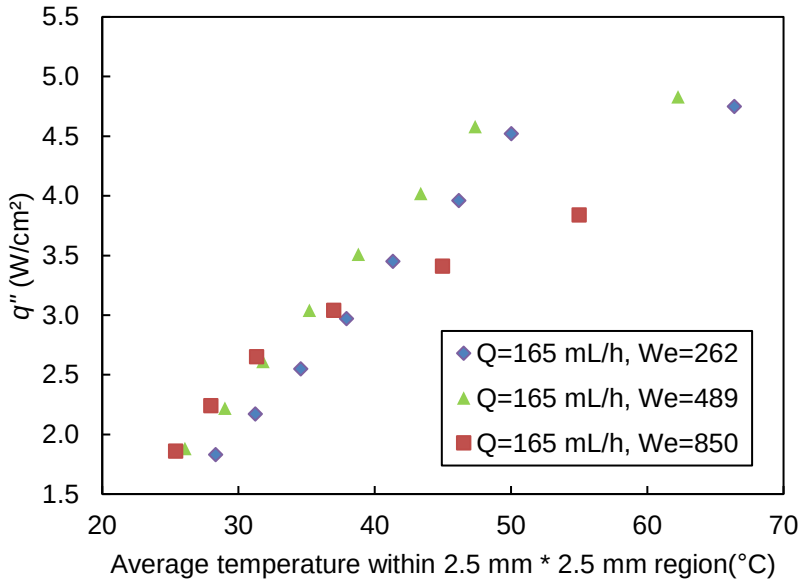

Fig. 36. Effects of droplet Weber number on heat transfer performance at a fixed flow rate of 165 mL/h

Fig. 37 shows the temperature profiles across the impact craters at different heat flux and droplet Weber number conditions. As shown in Fig. 37(a), higher droplet Weber number leads to lower temperature distribution at a heat flux of 2.6 W/cm². Furthermore, at a heat flux of 2.6 W/cm², dry-out area was not observed for all the cases considered. However, at a heat flux of 3.5 W/cm², dry-out area appeared on the heater surface for the strong splashing case only (*We*=850). The emergence of dry-out area leads to a higher surface temperature distribution, as shown in Fig. 37(b). Furthermore, temperature profile becomes asymmetric due to the emergence of an asymmetric dry-out area.

The experimental local Nusselt number profiles for single droplet train impingement were obtained based on the methodologies described in Soriano et al. [55]. Nusselt numbers were calculated at different radial positions using local surface temperatures ($T(r)$), initial droplet temperature (T_0), orifice diameter (d_{orf}) and heat flux value (q'') [55], as follows:

$$Nu_{d_{orf}}(r) = \frac{q''}{T(r) - T_0} \frac{d_{orf}}{k_l} \tag{31}$$

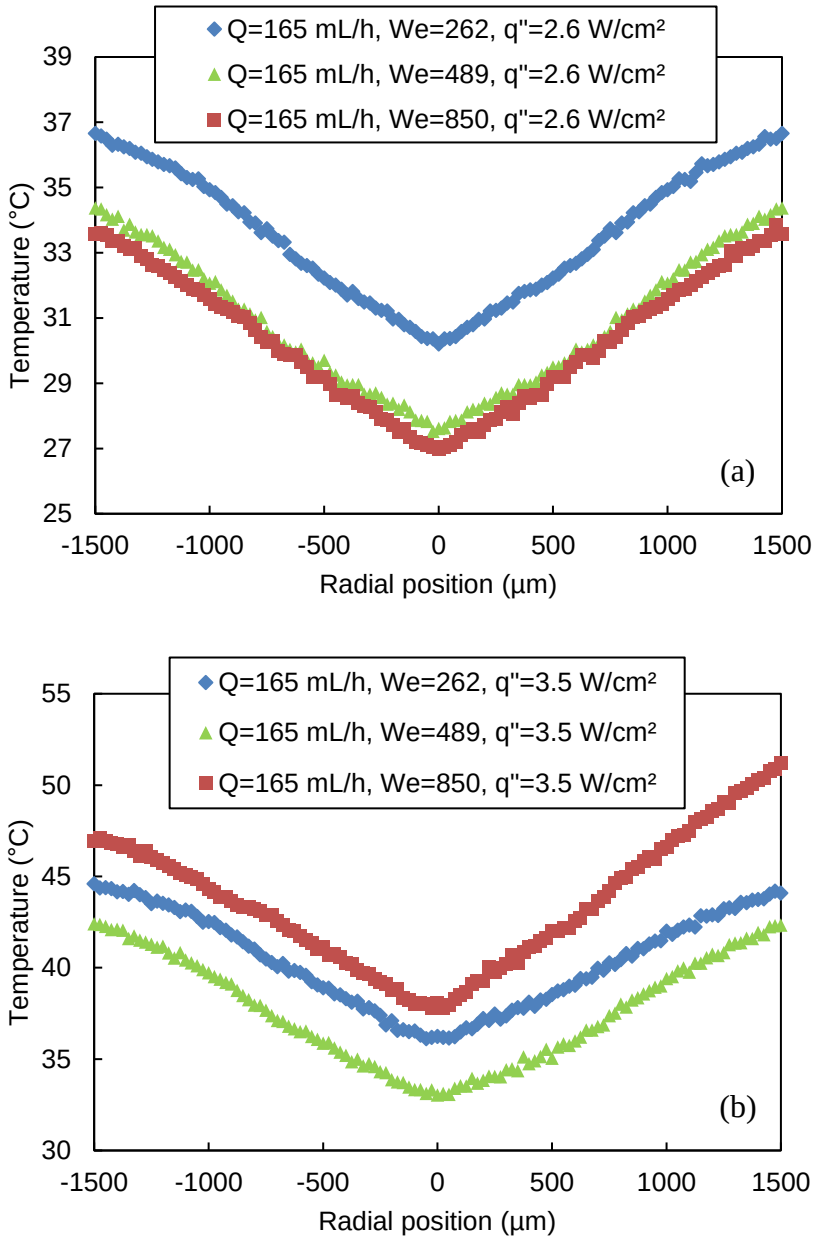

Fig. 37. Effects of droplet Weber number on temperature distribution at (a) *q"*=2.6 W/cm² and (b) *q"*=3.5 W/cm²

Fig. 38 shows the Nusselt number profiles and the predictions given by Nusselt number correlations for three single droplet train impingement cases (cases 1, 4 and 5 in Table 8). Nusselt number correlations were obtained based on the methodologies described in Soriano et al. [55], using the following formulation:

$$Nu_{d_{orf}}(r) = A\,\mathrm{Re}_{d_{orf}}^{1/2}\,\mathrm{Pr}^{1/3},\ 0 \le r/d_{orf} \le 1 \tag{32}$$

$$Nu_{d_{orf}}(r) = A\,\mathrm{Re}_{d_{orf}}^{1/2}\,\mathrm{Pr}^{1/3}\left(\frac{d_{orf}}{r}\right)^{b},\ r/d_{orf} > 1 \tag{33}$$

$$\mathrm{Re}_{d_{orf}} = \frac{V_d \cdot d_{orf}}{\nu}$$
$$\mathrm{Re}_{d_{orf}} = \mathrm{Re}_{d_d} \cdot \frac{d_{orf}}{d_d} \tag{34}$$

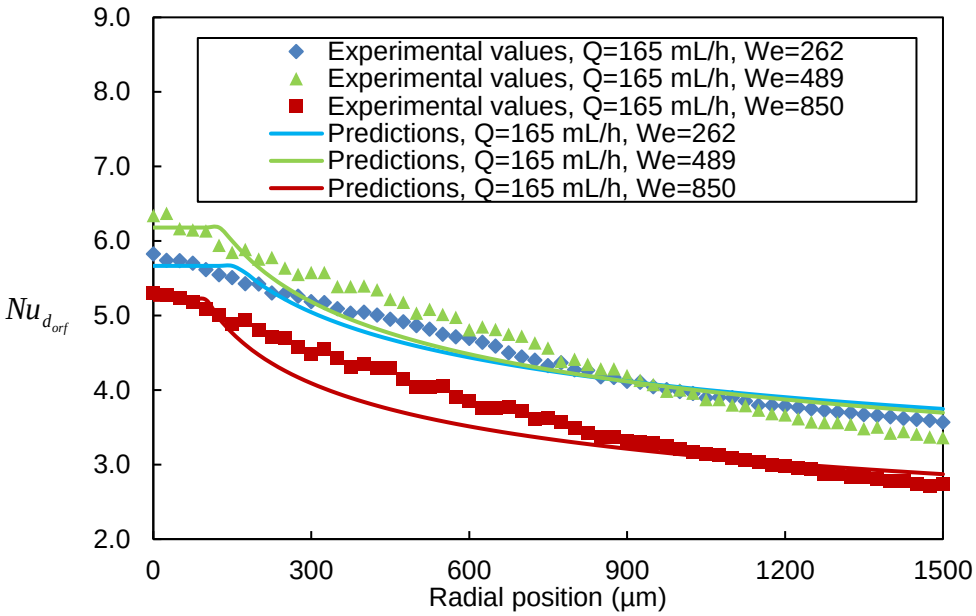

Fig. 38. Experimental Nusselt number profiles and predictions given by Nusselt number correlations for single droplet train impingement using orifice diameter as characteristic length

The values of coefficients *A* and *b* in Equations 31 and 32, and R^2 values of the correlations are shown in Table 10, as follows:

Table 10. Local Nusselt number correlation coefficients in Equations 31 and 32

Q (mL/h)	*f* (Hz)	d_{orf} (μm)	*We*	$\mathrm{Re}_{d_{orf}}$	Impingement regime	*A*	*b*	R^2
165	5000	160	262	1194	Spreading	0.0756	0.18	0.95
165	7500	130	489	1398	Start of splashing	0.0762	0.21	0.90
165	15000	100	850	1614	Strong splashing	0.0598	0.22	0.89

As Table 10 shows, the coefficients of *A* and *b* depend on impingement regime and droplet Weber number. It should be noted that the Nusselt numbers correlations shown in Fig. 38 and Table 10 were obtained using orifice diameter (d_{orf}) as characteristic length. However, the three cases considered in Fig. 38 and Table 10 used different orifice diameters. In order to compare the convective heat transfer performance of different impingement regimes, it is necessary to use the same characteristic length. Fig. 39 shows the Nusselt number profiles using the length of the heater (L_{heater} = 10 mm) as characteristic length. Nusselt numbers in Fig. 39 were calculated using Equation 35, as follows:

$$Nu_{L-heater} = \frac{L_{heater}}{d_{orf}} Nu_{d_{orf}}(r)$$
$$Nu_{L-heater} = \frac{q''}{T(r) - T_0} \frac{L_{heater}}{k_l} \quad (35)$$

The Nusselt number correlations in Fig. 39 were obtained using Equations 36 and 37, as follows:

$$Nu_{L-heater}(r) = \frac{L_{heater}}{d_{orf}} Nu_{d_{orf}}(r) = B\,\mathrm{Re}_{d_{orf}}^{1/2}\,\mathrm{Pr}^{1/3}, 0 \le r/d_{orf} \le 1 \quad (36)$$

$$Nu_{L-heater}(r) = \frac{L_{heater}}{d_{orf}} Nu_{d_{orf}}(r) = B\,\mathrm{Re}_{d_{orf}}^{1/2}\,\mathrm{Pr}^{1/3}\left(\frac{d_{orf}}{r}\right)^{b}, \; r/d_{orf} > 1 \quad (37)$$

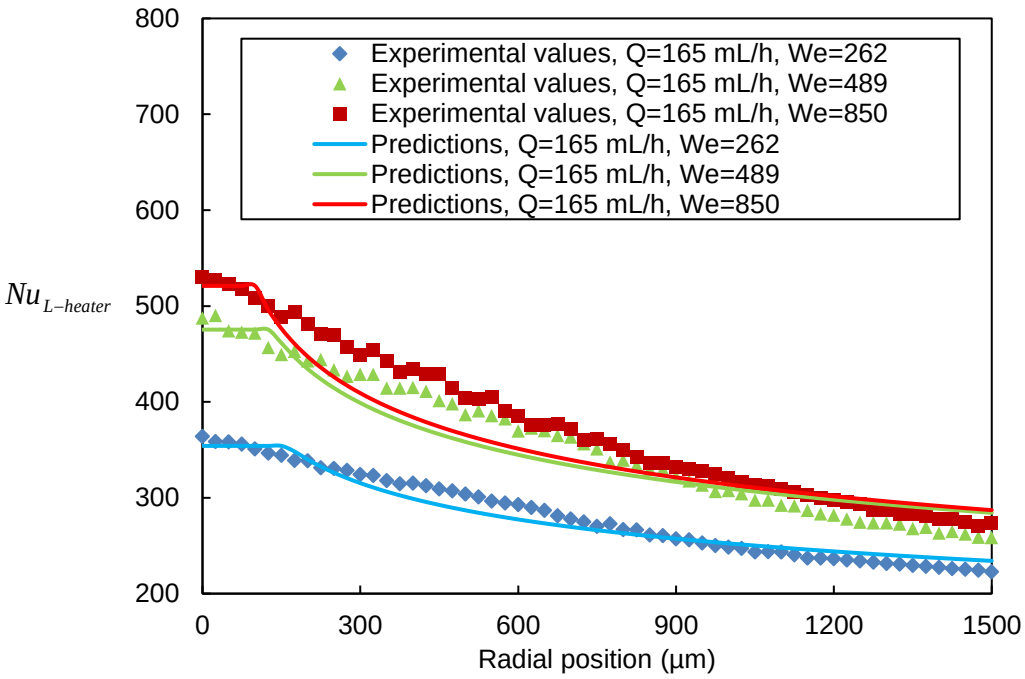

Fig. 39. Experimental Nusselt number profiles and predictions given by Nusselt number correlations for single droplet train impingement using heater length as characteristic length

The values of coefficients *B* and *b* in Equations 35 and 36 are shown in Table 11, as follows:

Table 11. Local Nusselt number correlation coefficients in Equations 35 and 36

Q (mL/h)	f (Hz)	d_{orf} (μm)	We	$\mathrm{Re}_{d_{orf}}$	Impingement regime	B	b	R^2
165	5000	160	262	1194	Spreading	4.72	0.18	0.95
165	7500	130	489	1398	Start of splashing	5.86	0.21	0.90
165	15000	100	850	1614	Strong splashing	5.98	0.22	0.89

As shown in Fig. 39 and Table 11, local Nusselt number increases with droplet Weber number, which could be due to the higher momentum of impinging droplets at higher droplet Weber number conditions, even though all cases had the same flowrate. Furthermore, the exponent on radial position (i.e. coefficient *b*) increases with Weber number, which indicates that Nusselt number decays faster with radial position at higher Weber number conditions. Moreover, Table 11 shows that the correlation coefficient decreases slightly with Weber number because of the randomness associated with the splashing process, which is consistent with previous studies [55]. The decrease of the correlation coefficient is associated with the stochastic nature of splashing and its effects on convective heat transfer [55].

4.2. Results and analysis of double droplet train impingements

In this sub-section, the results of double droplet train impingement experiments are discussed, including the effects of impact spacing on droplet-induced hydrodynamics and surface heat transfer. Table 12 shows a summary of experimental conditions and variables for double droplet train impingement. Orifice diameter was fixed at 150 μm for the cases shown in Table 12.

Table 12. Experimental conditions and variables for double droplet train impingement

Input variables		Experimental values				
Q (mL/h)	f (Hz)	d_d (μm)	V_d (m/s)	We	Re_{d_d}	S (mm)
2*135=270	4000	259 ± 8	2.79 ± 0.05	226 ± 10	1809 ± 90	0.65–2
2*165=330	6000	242 ± 9	3.40 ± 0.05	312 ± 15	2054 ± 121	0.65–2
2*195=390	7000	240 ± 8	4.02 ± 0.07	434 ± 20	2415 ± 133	0.65–2

As shown in Table 12, flow rate of the cooling liquid varied from 2*135 (270 mL/h) to 2*195 mL/h (390 mL/h). For each flow rate considered, a wide range of impact spacings (0.65-2 mm) were used in the experiments. The effects of impact spacing on droplet-induced hydrodynamics and surface heat transfer are presented below.

Fig. 40 shows the images of double droplet train impingement at different impact spacings. As shown in Fig. 40, a hump was formed between impact craters due to the interactions caused by the impinging droplet streams. At a high impact spacing of 2 mm, the interactions or fluid collisions were observed to be weak, resulting in a relatively low hump. However, at a low impact spacing of 0.65 mm, the interactions were stronger and a much higher hump could be observed.

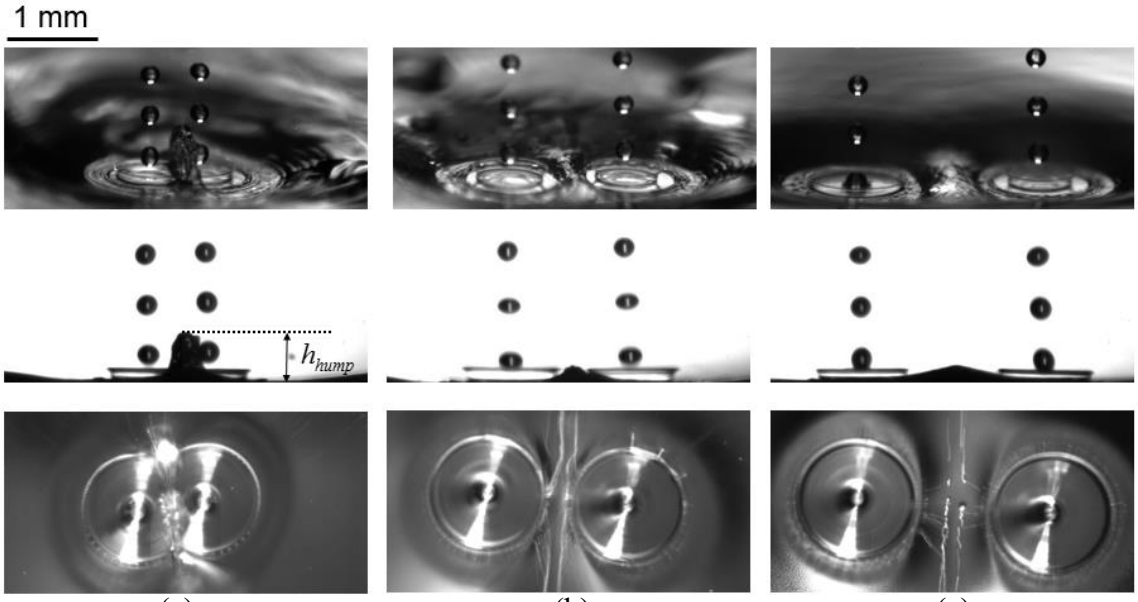

Fig. 40. Double droplet train impingement at impact spacing of (a) 0.65 mm, (b) 1.45 mm and (c) 2 mm, all images were captured at Q =2*165 mL/h, We = 312

Fig. 41 shows a schematic diagram of crown interactions at different impact spacing conditions. As shown in Fig. 41(a), droplet-induced crowns do not interact with each other directly when impact spacing (S) is greater than the maximum crown rim diameter ($d_{c,rim,max}$). When S is lower than $d_{c,rim,max}$, crowns interact with each other directly during the crown propagation process, as shown in Fig. 41(c).

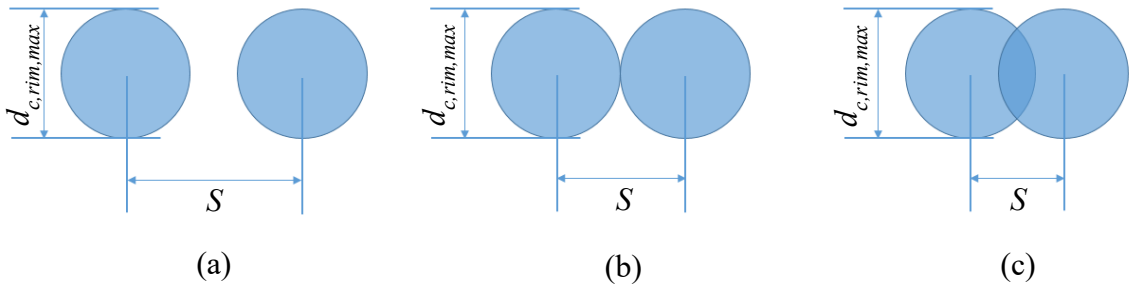

Fig. 41. Schematic diagram of crown interactions at different impact spacing conditions

Table 13 and Fig. 42 show the hump height at different impact spacing and flow rate conditions. Maximum crown rim diameter ($d_{c,rim,max}$) , which was defined in Section 4.1.1, is shown in Table 13 and Fig. 42 as reference. As shown in Table 13 and Fig. 42, the hump height decreases with impact spacing, which is consistent with the results shown in Li et al. [86, 87] and Raman et al. [88]. Furthermore, hump height was almost a constant when impact spacing was higher than $d_{c,rim,max}$. When impact spacing is lower than $d_{c,rim,max}$, a drastic increase in hump height was observed due to the high fluid inertia during droplet stream-induced interaction process. Moreover, when S is lower than $d_{c,rim,max}$, the hump height fluctuates more than at higher impact spacing conditions. The higher fluctuations of hump height can be associated with the vigorous development process of the adjacent crowns at low impact spacing conditions (i.e. $S < d_{c,rim,max}$).

Table 13. Hump height at different impact spacing conditions

Q (mL/h)	We	$d_{c,rim,max}$ (μm)	h_{hump} ($S = S_{min}$)[a] (μm)	h_{hump} ($S = d_{c,rim,max}$) (μm)	h_{hump} ($S = S_{max}$)[b] (μm)
135	226	1109 ± 35	378 ± 44	137 ± 22	101 ± 11
165	312	1222 ± 51	551 ± 67	144 ±20	128 ± 12
195	434	1425 ± 43	1035 ± 163	163 ± 28	126 ± 9

[a] S_{min} = 0.65 mm, $S_{min} < d_{c,rim,max}$ for all the cases considered
[b] S_{max} = 2 mm, $S_{max} > d_{c,rim,max}$ for all the cases considered

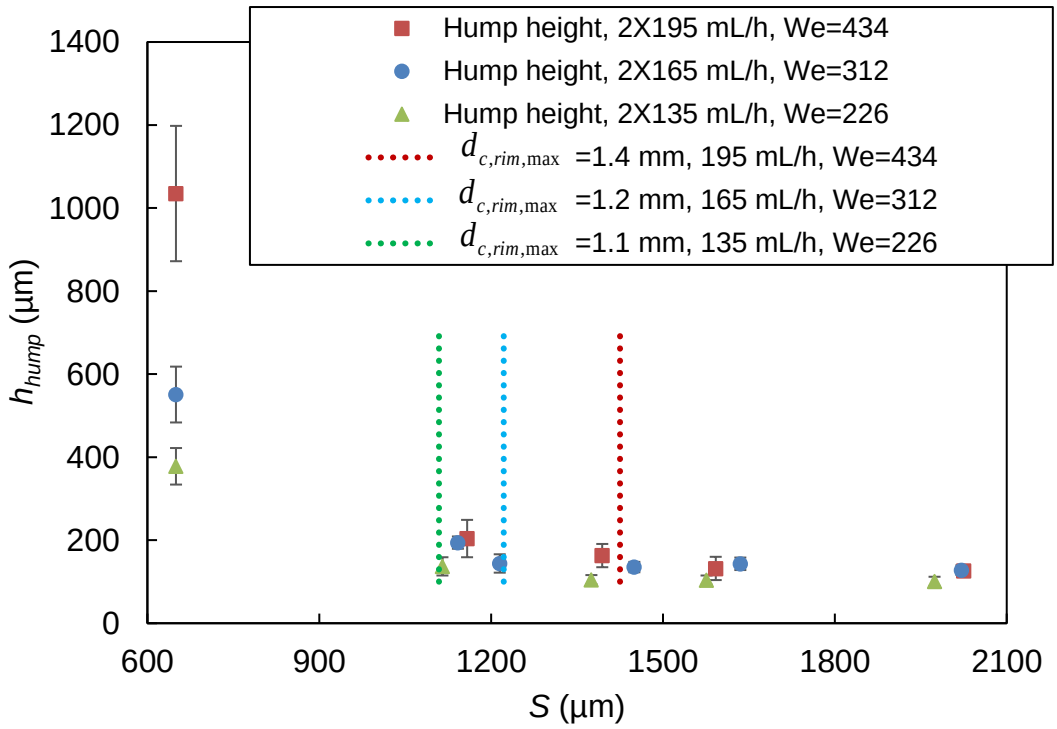

Fig. 42. Effects of impact spacing on hump height for double droplet train impingement

The effects of impact spacing on surface temperature have also been investigated for double droplet train impingement. Average temperatures were measured on a straight line ($\overline{T}_{line}$) as shown in Fig. 43. The straight line used to determine average temperatures

connects the two center points of droplet stream impingement. Fig. 44 through 46 show the effects of impact spacing on heat transfer performance at fixed flow rate conditions.

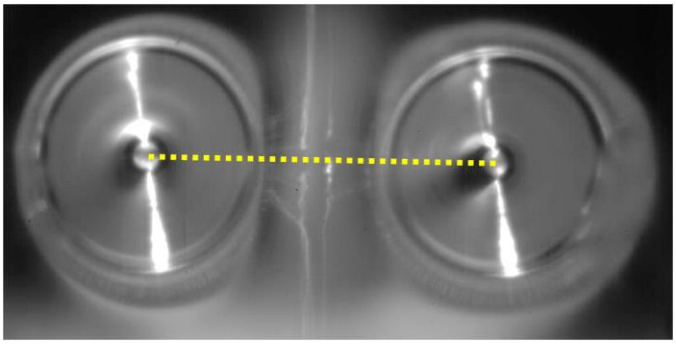

Fig. 43. Location of straight line for temperature measurement

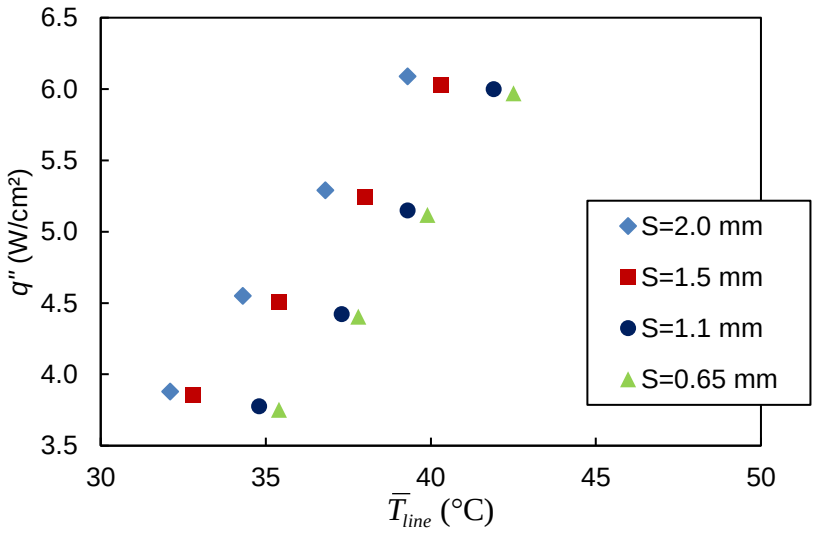

Fig. 44. Effects of impact spacing on heat transfer performance for double droplet train impingement at flow rate of 2*135 mL/h, *We* = 226

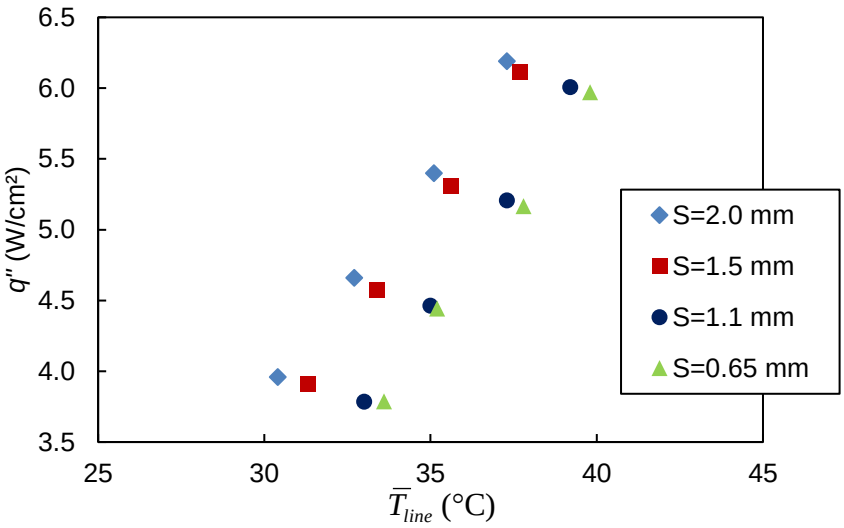

Fig. 45. Effects of impact spacing on heat transfer performance for double droplet train impingement at flow rate of 2*165 mL/h, *We* = 312

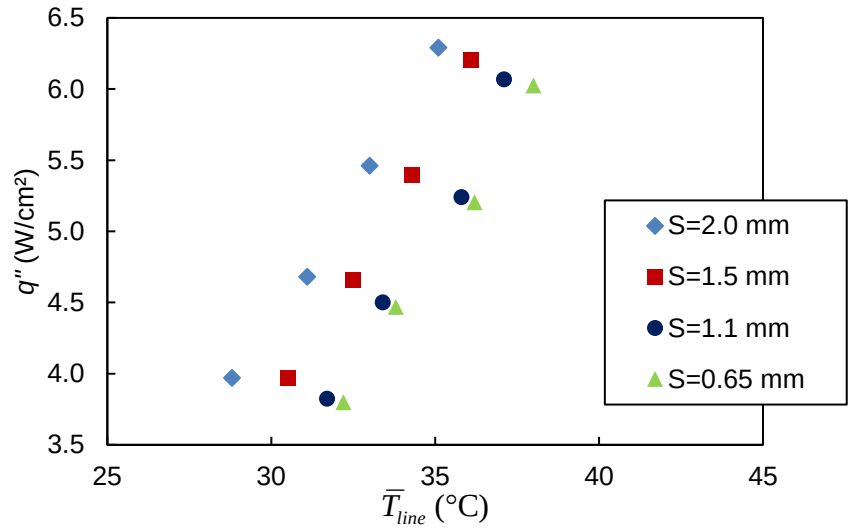

Fig. 46. Effects of impact spacing on heat transfer performance for double droplet train impingement at flow rate of 2*195 mL/h, *We* = 434

As shown in Fig. 44 through 46, at fixed flow rate conditions, higher impact spacing leads to better heat transfer performance for double droplet train impingement. The results are consistent with the findings in Tsai [52] and Zhang et al. [53]. The heat transfer results indicate that for double droplet train impingement, crater formation should not be disturbed to enable better heat transfer performance.

Fig. 47 through 49 show the temperature profiles across two impact craters at different impact spacing and flow rate conditions. In Fig. 47 through 49, position of "0" stands for the mid-point between two impact craters. As shown in Fig. 47 through 49, higher impact spacing leads to lower surface temperature distribution both locally and globally, which is consistent with the results shown in Tsai [52] and Zhang et al. [53]. Furthermore, temperature distribution is relatively uniform between impact craters, specifically at low spacing, which indicates that crater interactions lead to effective fluid mixing inside and outside the impact craters, leading to a uniform surface temperature distribution. However, greater spacing leads to lower temperature profiles as seen in Fig. 47 through 49, which suggests that hump height plays a significant role in terms of local heat transfer behavior. As shown in Table 13 and Fig. 42, higher impact spacing leads to a lower hump height, which allows more fluid to be in direct contact with the heater surface during the heat transfer process. Nevertheless, lower impact spacing leads to a higher hump height, which may reduce the liquid usage efficiency for surface cooling.

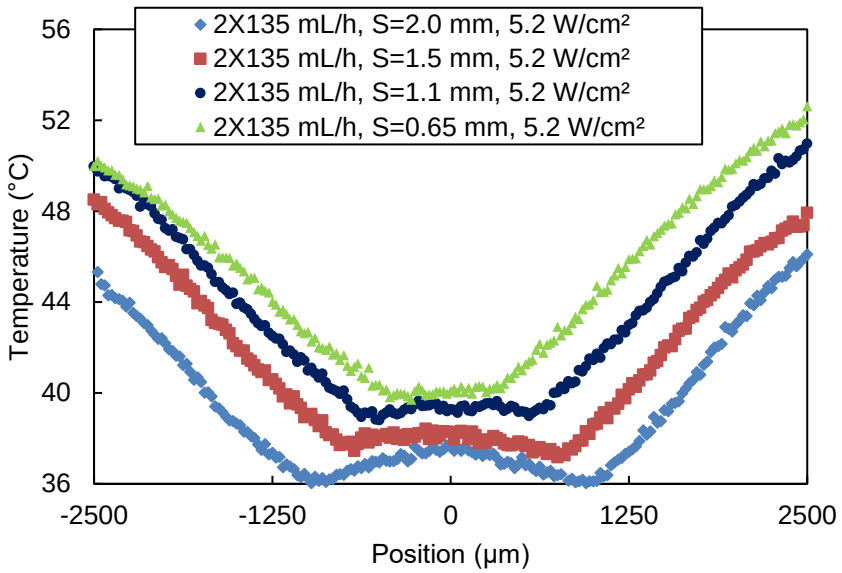

Fig. 47. Effects of impact spacing on surface temperature distribution at flow rate of 2*135 mL/h, *We* = 226

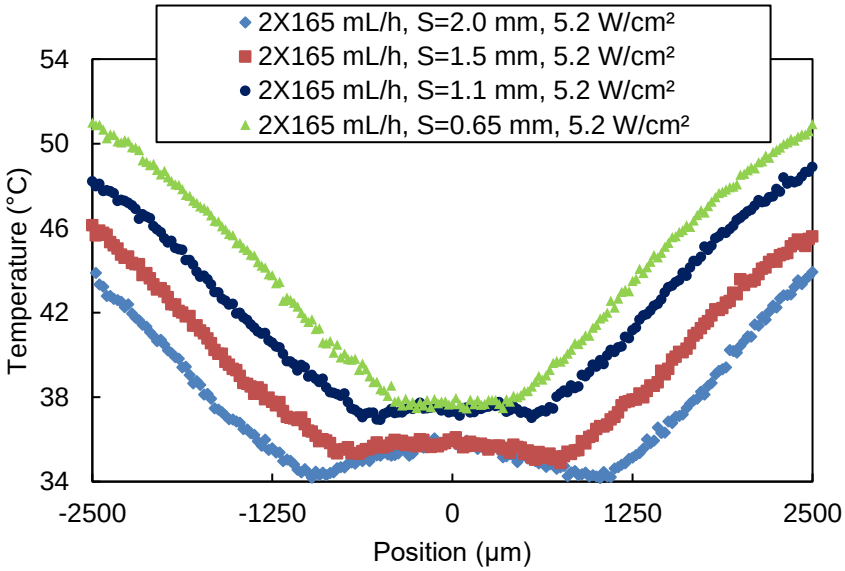

Fig. 48. Effects of impact spacing on surface temperature distribution at flow rate of 2*165 mL/h, *We* = 312

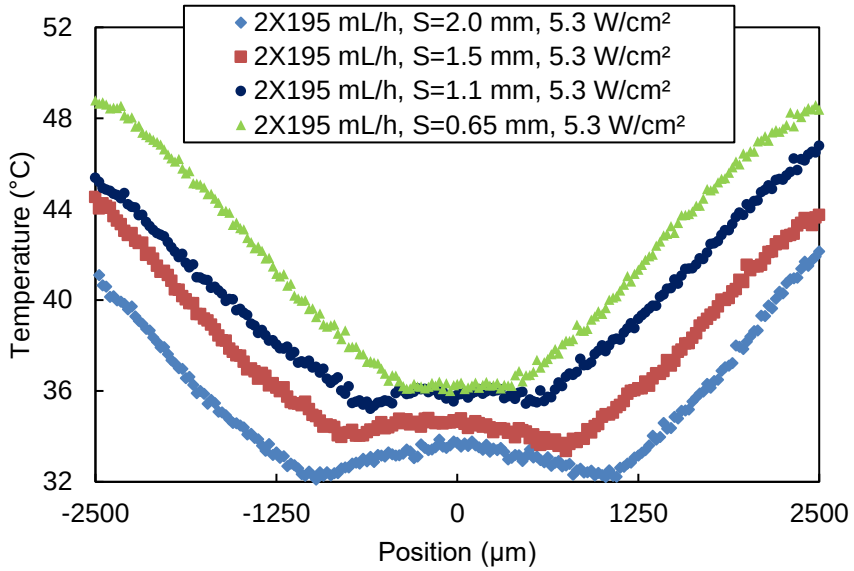

Fig. 49. Effects of impact spacing on surface temperature distribution at flow rate of 2*195 mL/h, *We* = 434

The effects of impact spacing and flow rate on Nusselt number were investigated using average local surface temperature ($\overline{T}_{line}$), initial droplet temperature (T_0), droplet diameter (d_d) and heat flux value (q''), as follows:

$$\overline{Nu}_{d_d} = \frac{q''}{\left(\overline{T}_{line} - T_0\right)} \cdot \frac{d_d}{k_l} \tag{38}$$

Nusselt number correlations were obtained using similar mathematical forms as described in references [89-91] for multiple circular jet impingement cooling, as follows:

$$\overline{Nu}_{d_d} = K \cdot \mathrm{Pr}^{1/3} \cdot \mathrm{Re}_{d_d}^{a} \cdot \exp\left(b\frac{S}{d_d}\right) \tag{39}$$

In Equation 38, the exponent of 1/3 for Prandtl number was chosen because only one fluid was tested in the current study. Furthermore, Soriano et al. [55] have shown

that Nu scales well with $Pr^{1/3}$ in droplet train impingement heat transfer experiments. Based on regression analysis, the following equation for double droplet train impingement is proposed:

$$\overline{Nu}_{d_d} = 0.0231 \cdot \mathrm{Pr}^{1/3} \cdot \mathrm{Re}_{d_d}^{0.6993} \cdot \exp\left(0.05192 \cdot \frac{S}{d_d}\right), \mathrm{R}^2 = 0.96 \quad (40)$$

It is worth noting that Equation 40 takes into account the combined effects of crown propagation dynamics within each impingement zone and the hump height outside the impingement zone as spacing is increased. Fig. 50 shows the effects of non-dimensional impact spacing (S/d_d) on Nusselt number for double droplet train impingement. As shown in Fig. 50, a good agreement was reached between experimental data and the predictions given by Equation 40. Furthermore, Nusselt number profile tend to shift upwardly when droplet Reynolds number increases, which indicates that droplet Reynolds number is a significant factor for droplet-induced convective heat transfer. Moreover, at fixed flow rate (or droplet Reynolds number) conditions, Nusselt number increases with impact spacing. The results further validate that impact spacing plays a significant role in droplet train impingement cooling.

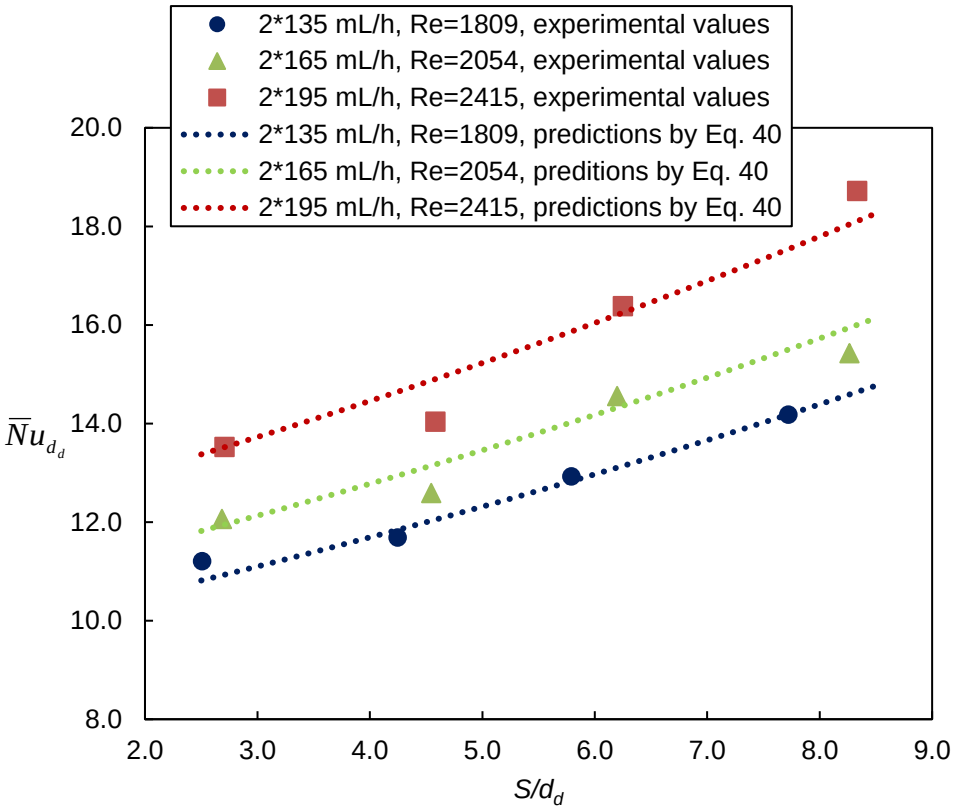

Fig. 50. Effects of non-dimensional impact spacing and droplet Reynolds number on Nusselt number for double droplet train impingement

4.3. Results and analysis of triangulated droplet train impingement

In this sub-section, the results of triangulated droplet train impingement experiments are presented. The effects of horizontal impact spacing and droplet Weber number on droplet-induced surface jet flows and heat transfer are discussed. Table 14 shows a summary of experimental conditions and variables for triangulated droplet train impingement. The schematic diagram of the triangulated impingement pattern and the definition of impact spacing (S) are shown in Fig. 51.

Table 14. Experimental conditions and variables for triangulated triple droplet train impingement

Experimental variables	Range
Flow rate per droplet train, Q (mL/h)	70-97
Droplet impingement frequency, f (Hz)	6500-7100
Orifice diameter, d_{orf} (μm)	100
Horizontal impact spacing, S (mm)	0.7-1.5
Droplet diameter, d_d (μm)	175-190
Droplet impingement velocity, V_d (m/s)	2.73-3.77
Droplet Weber number, $We = \frac{\rho d_d V_d^2}{\sigma}$	143-302
Droplet Reynolds number, $Re_{d_d} = \frac{V_d d_d}{\nu}$	1191-1785

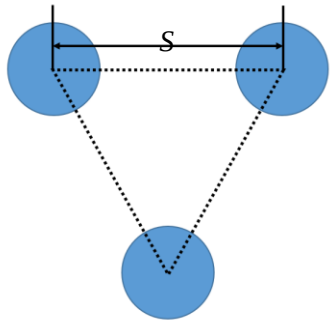

Fig. 51. Schematic diagram of triangulated impingement pattern

As shown in Table 14, the droplet impingement frequency was in the range of 6500 to 7100 Hz for each droplet train. Droplet diameter and droplet velocity were in the range of 175-190 μm and 2.73-3.77 m/s, respectively. Five horizontal impact spacings, namely 0.7, 0.9, 1.1, 1.3 and 1.5 mm, were used in the experiments. The experimental conditions considered in the current work were able to induce a wide range of surface jet flow conditions, as described below.

High speed images were taken from below of the heater to observe the surface jet flows induced by the triangulated droplet train impingement. Fig. 52 shows a group of surface jet flow images with different flow rate and impact spacing when no heat was applied.

As shown in Fig. 52, surface jet liquid flows were observed among impact craters. Furthermore, at low flow rate and high impact spacing conditions, the surface jet flows were observed to be laminar, as show in Fig. 52(d), 52(g) and 52(h). For the laminar surface jet cases, surface jet flows among the impact craters seemed to be unperturbed by the surrounding impact craters. Furthermore, laminar surface jet flows seemed to be well-delineated due to the low flow velocity. However, at high flow rate and low impact spacing conditions, the surface jet flows were found to be chaotic, as shown in Fig. 52(b), 52(c) and 52(f). A transitional region between laminar and chaotic surface jet flows was identified by adjusting flow rate and impact spacing, as shown in Fig. 52(a), 52(e) and 52(i). Fig. 53 shows a schematic diagram of the surface jet flow transition that occurs when flow rate and impact spacing are varied.

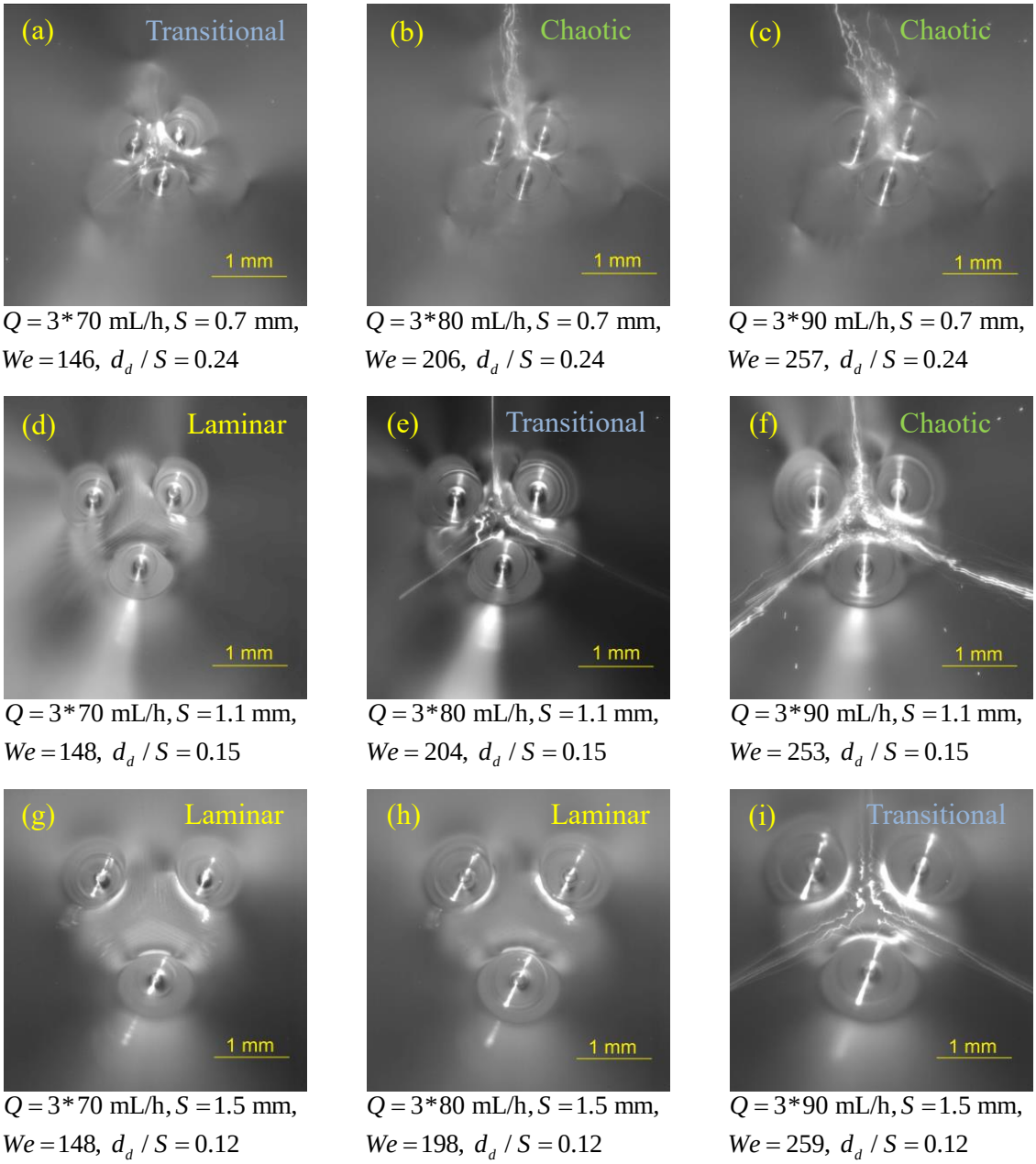

$Q = 3*70$ mL/h, $S = 0.7$ mm, $We = 146$, $d_d / S = 0.24$

$Q = 3*80$ mL/h, $S = 0.7$ mm, $We = 206$, $d_d / S = 0.24$

$Q = 3*90$ mL/h, $S = 0.7$ mm, $We = 257$, $d_d / S = 0.24$

$Q = 3*70$ mL/h, $S = 1.1$ mm, $We = 148$, $d_d / S = 0.15$

$Q = 3*80$ mL/h, $S = 1.1$ mm, $We = 204$, $d_d / S = 0.15$

$Q = 3*90$ mL/h, $S = 1.1$ mm, $We = 253$, $d_d / S = 0.15$

$Q = 3*70$ mL/h, $S = 1.5$ mm, $We = 148$, $d_d / S = 0.12$

$Q = 3*80$ mL/h, $S = 1.5$ mm, $We = 198$, $d_d / S = 0.12$

$Q = 3*90$ mL/h, $S = 1.5$ mm, $We = 259$, $d_d / S = 0.12$

Fig. 52. Bottom view of triangulated droplet train impingement when heat was not applied

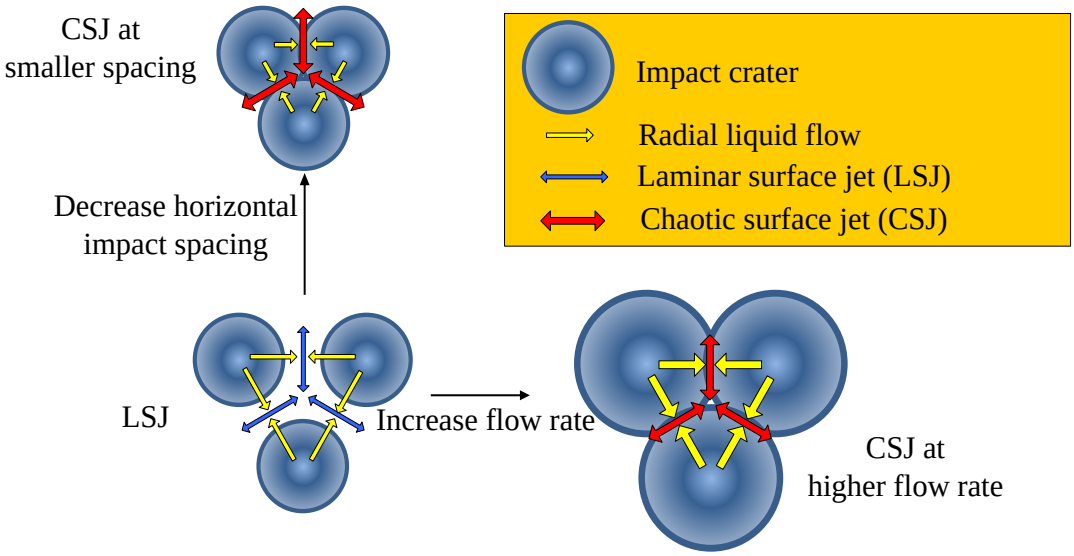

Fig. 53. Schematic diagram of surface jet flow transition

As illustrated in Fig. 53, surface jet flows are produced by the interactions among the radial liquid flows emanating from the droplet impingement zones and the impact craters themselves. When the flow rate is low or the impact spacing is high, the interactions among the radial liquid flows from the different impact craters are observed to be weak, leading to laminar surface jet flows. However, by increasing flow rate or decreasing horizontal impact spacing, the interactions of radial liquid flows from different impact craters become stronger, leading to chaotic surface jet flows. A similar transition behavior has been seen when two normal impinging circular liquid jets interact, which leads to the formation of two contiguous hydraulic jumps, as illustrated in Kate et al. [92]. Kate et al. [92] claimed that chaotic fluid flows form when the spacing between two impinging liquid jets is lower than the hydraulic jump diameter, while laminar fluid flows form when the spacing is greater than the hydraulic jump diameter.

A map for surface jet flow transition based on non-dimensional impact spacing (d_d/S) and droplet Weber number (We) has been developed, as shown in Fig. 54. In Fig. 54, laminar, chaotic and transitional surface jet flows have been identified based on visual observations. An empirical correlation has been postulated, which is capable of predicting the transition between laminar and chaotic surface jet flows. The correlation takes the following mathematical form: $(d_d/S) \cdot We^n$ = constant, where n is 0.97 and the value of constant is 28. The R^2 value of the correlation is 0.94, which means the correlation is accurate and credible in terms of predicting and denoting the transition region. It should be noted that the identification of the laminar, transitional and chaotic surface jet flows is based on visual observations only. The postulated correlation uses Weber number instead of Reynolds number because Weber number takes into account properties such as surface tension, which is important in the assessment of the dynamics of the hydraulic jump region. Moreover, the correlation is only valid for high frequency HFE-7100 droplet impingement because only one liquid was been used in this study.

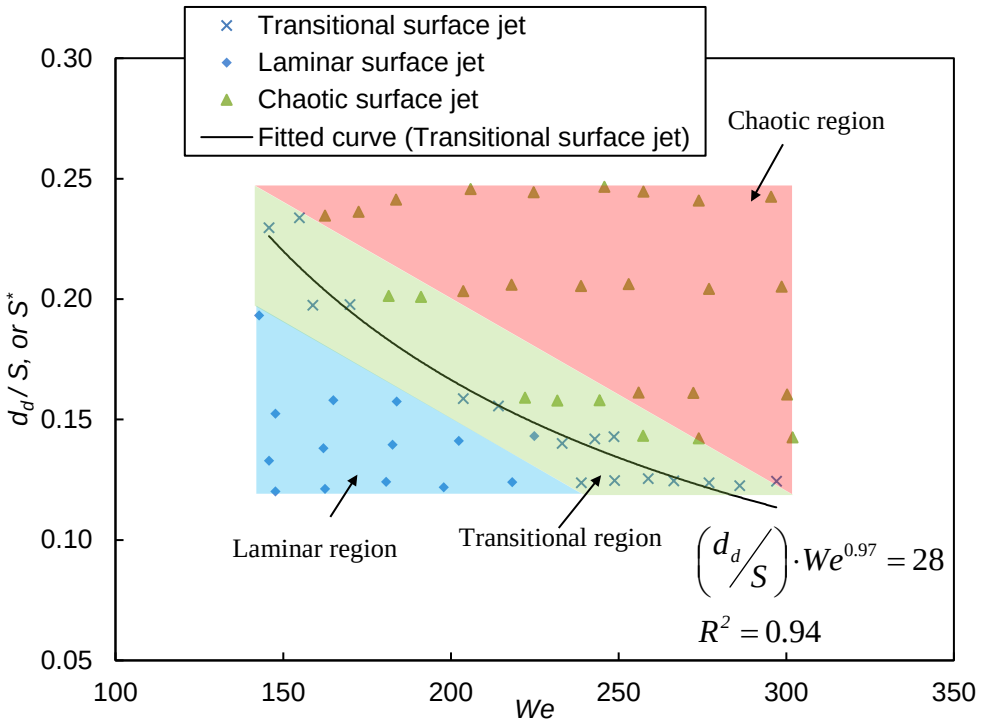

Fig. 54. Map of surface jet flow transition

The effects of impact spacing on surface temperature have also been investigated for triangulated droplet train impingement. Average temperatures were measured on a triangulated area ($\overline{T}_{tri}$), as shown in Fig. 55. The three vertexes of the triangulated area coincide with the three center points of droplet impingement. Fig. 56 through 58 show the effects of impact spacing on heat transfer performance at fixed flow rate conditions.

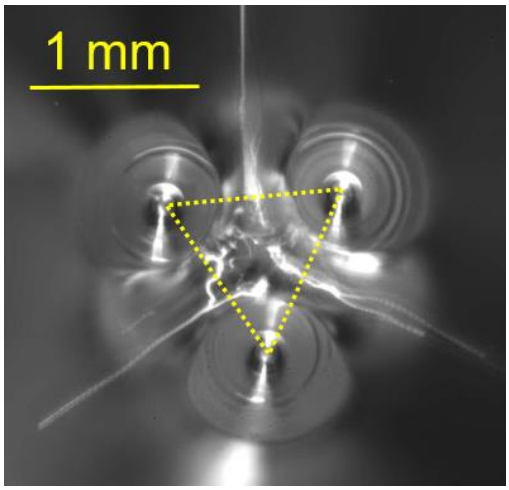

Fig. 55. Location of triangulated area for temperature measurement

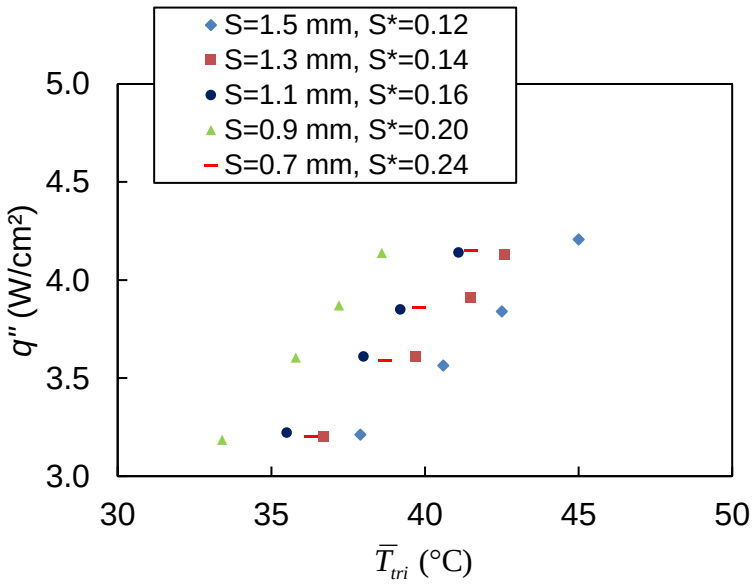

Fig. 56. Effects of impact spacing on heat transfer performance at a flow rate of 3*70 mL/h, *We* = 150, *Re* = 1200

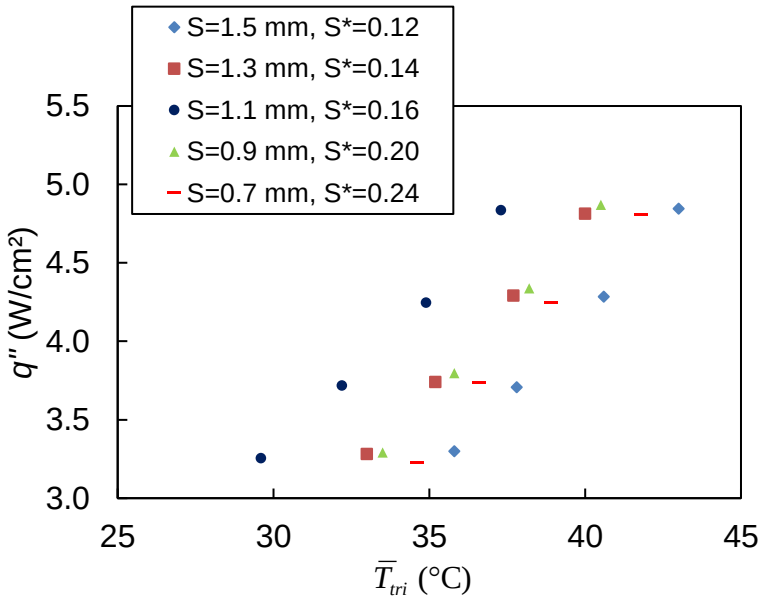

Fig. 57. Effects of impact spacing on heat transfer performance at a flow rate of 3*80 mL/h, *We* = 200, *Re* = 1450

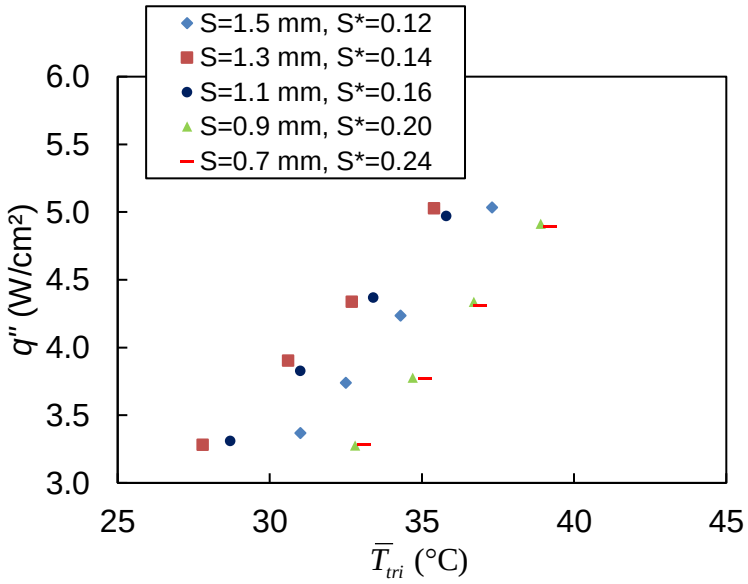

Fig. 58. Effects of impact spacing on heat transfer performance at a flow rate of 3*90 mL/h, *We* = 250, *Re* = 1640

As shown in Fig. 56 through 58, impact spacing plays a significant role in heat transfer performance at fixed flow rate conditions. For instance, at a flow rate of 3*70 mL/h, an impact spacing of 0.9 mm leads to the optimum heat transfer performance as seen in Fig. 56. However, when flow rate increases to 3*80 and 3*90 mL/h, the optimum heat transfer performance is seen at an impact spacing of 1.1 mm and 1.3 mm, respectively, as shown in Fig. 57 and 58. These data indicate that at a fixed flow rate, horizontal impact spacing should be carefully selected to achieve optimum heat transfer performance for triangulated droplet train impingement.

It should be noted that neither weak laminar surface jet (We = 150, S^* = 0.12) nor strong chaotic surface jet (We = 250, S^* = 0.24) lead to optimum heat transfer performance at fixed flow rate conditions, as seen in Fig. 56 and 58, respectively. Table 15 shows the values of S^* on the surface jet transition boundary curve and those that lead to optimum heat transfer performance at Weber number of 150, 200 and 250. As shown in Table 15, the relative difference between the value of S^* on the surface jet transition boundary curve and the values of S^* that lead to optimum heat transfer are within 10 %, which indicates that optimum heat transfer cases should be as close as possible to the surface jet transition region (as depicted in Fig. 54) for triangulated droplet train impingement.

Table 15. Comparison of values of S^* on the surface jet transition boundary curve and S^* for optimum heat transfer performance

Q (mL/h)	We	S^* on the transition boundary curve $\left(S^* \cdot We^{0.97} = 28\right)$	S^* value for optimum heat transfer performance	% difference
3*70	150	0.216	0.195	-9.7
3*80	200	0.166	0.159	-4.2
3*90	250	0.134	0.143	6.7

Fig. 59 through 61 show the effects of impact spacing on surface temperature distribution for triangulated droplet train impingement. The position of "0" represents the midpoint between two adjacent impact craters. From Fig. 59 through 61, optimum heat transfer cases (3*70 mL/h and S = 0.9 mm, 3*80 mL/h and S = 1.1 mm, 3*90 mL/h and S = 1.3 mm) depicts the lowest temperature distributions, which is consistent with the results shown in Fig 56 through 58. Furthermore, temperature profiles are relatively flat within the droplet impingement regions. The uniform temperature distributions can be attributed to the formation of surface jet flows among impact craters, which lead to an effective fluid and thermal mixing mechanism.

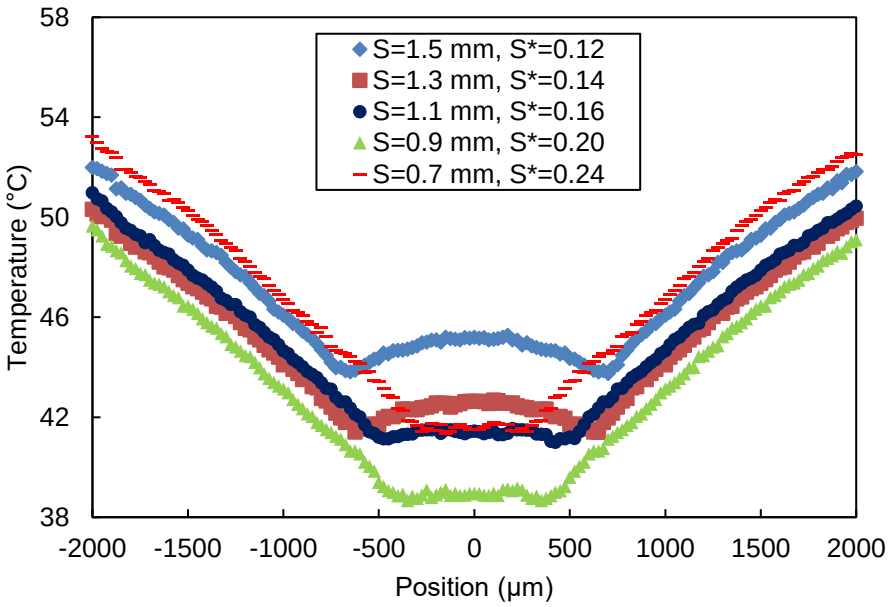

Fig. 59. Effects of impact spacing on temperature distribution for triangulated droplet train impingement at a flow rate of 3*70 mL/h, *We* = 150, *q''* = 4.1 W/cm²

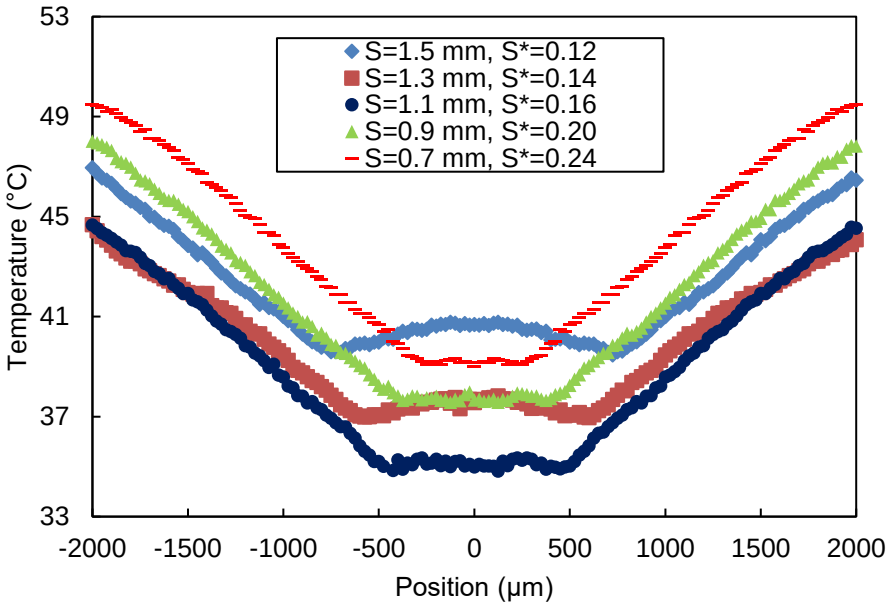

Fig. 60. Effects of impact spacing on temperature distribution for triangulated droplet train impingement at a flow rate of 3*80 mL/h, *We* = 200, *q''* = 4.3 W/cm²

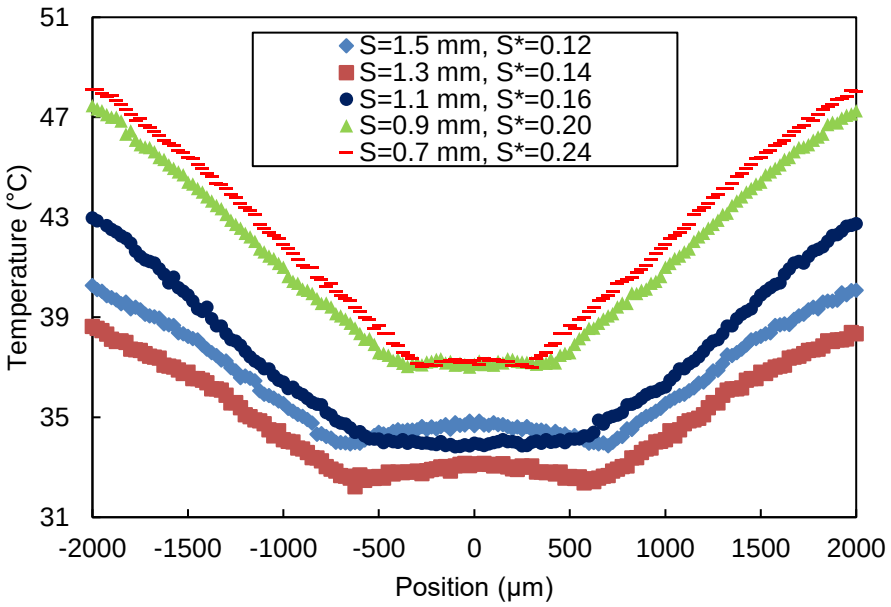

Fig. 61. Effects of impact spacing on temperature distribution for triangulated droplet train impingement at a flow rate of 3*90 mL/h, *We* = 250, *q''* = 4.3 W/cm²

The effects of impact spacing and flow rate on Nusselt number were investigated using average local surface temperature ($\overline{T}_{tri}$), initial droplet temperature (T_0), droplet diameter (d_d) and heat flux value (q''), as follows:

$$\overline{Nu}_{d_d} = \frac{q''}{\left(\overline{T}_{tri} - T_0\right)} \cdot \frac{d_d}{k_l} \tag{41}$$

The experimental Nusselt number values at different flow rate and impact spacing conditions are shown in Fig. 62. As shown in Fig. 62, at a fixed flow rate condition, the experimental Nusselt number peaks at a specific value of S/d_d. Furthermore, when flow rate increases, the position of the peak (i.e. value of S/d_d) shifts

to the right. Based on the experimental observations, the experimental Nusselt number data have been fitted using a Gaussian equation, as follows:

$$\overline{Nu}_{d_d} = K \cdot \mathrm{Pr}^{1/3} \cdot \mathrm{Re}_{d_d}^{a} \cdot \exp\left[-\left(\frac{\frac{S}{d_d} - b \cdot \mathrm{Re}_{d_d}{}^{c}}{d} \right)^2 \right] \tag{42}$$

In Equation 41, the exponent of 1/3 for Prandtl number was chosen because only one fluid was tested in the current study. Furthermore, Soriano et al. [55] have shown that *Nu* scales with $Pr^{1/3}$ in their droplet train impingement heat transfer experiments. A Gaussian equation was used to take into account the effect of spacing on heat transfer because of the transitional nature of surface flows seen in Fig. 52. Based on regression analysis, the following equation for triangulated droplet train impingement is proposed:

$$\overline{Nu}_{d_d} = 2.86\mathrm{e}^{-5} \cdot \mathrm{Pr}^{1/3} \cdot \mathrm{Re}_{d_d}^{1.6} \cdot \exp\left[-\left(\frac{\frac{S}{d_d} - 0.0035 \cdot \mathrm{Re}_{d_d}{}^{1.0276}}{5.403} \right)^2 \right], \mathrm{R}^2 = 0.92 \tag{43}$$

The predictions given by Equation 43 are also shown in Fig. 62. As shown in Fig. 62, a good agreement was reached between experimental data and the predictions given by Equation 43. Furthermore, the Nusselt number profile shifts upward when droplet Reynolds number increases, which indicates that droplet Reynolds number is a significant factor for droplet-induced convective heat transfer. Moreover, at fixed flow rate (or droplet Reynolds number) conditions, there is an optimum impact spacing for Nusselt number values. Fig. 62 also shows that for achieving the highest (peak) Nusselt number value, the spacing among the adjacent droplet streams should increase as well to

avoid unfavorable chaotic flow conditions on the surface. The results further validate that impact spacing plays a significant role in droplet train impingement cooling.

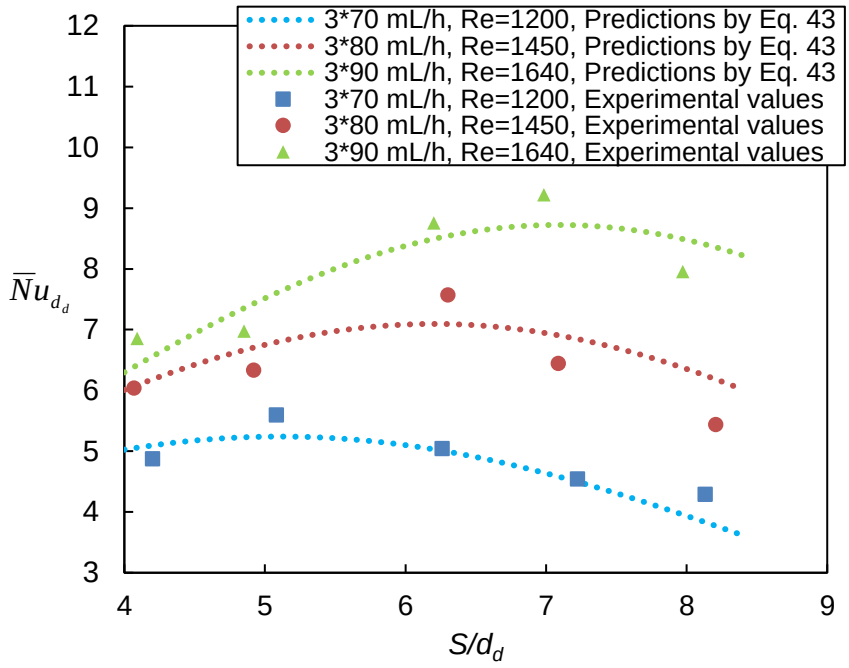

Fig. 62. Effects of impact spacing and droplet Reynolds number on Nusselt number for triangulated droplet train impingement

4.4. Results and analysis of hexagonal droplet train impingement arrays

In this section, the results of hexagonal droplet train impingement arrays experiments are presented and analyzed, including the effects of impact spacing and impingement pattern on droplet-induced hydrodynamics and surface heat transfer. Two impingement patterns are considered in this section, namely, a hexagonal arrangement with six and seven droplet impingement streams or trains. Fig. 63 shows a schematic diagram of the two impingement patterns considered in this section.

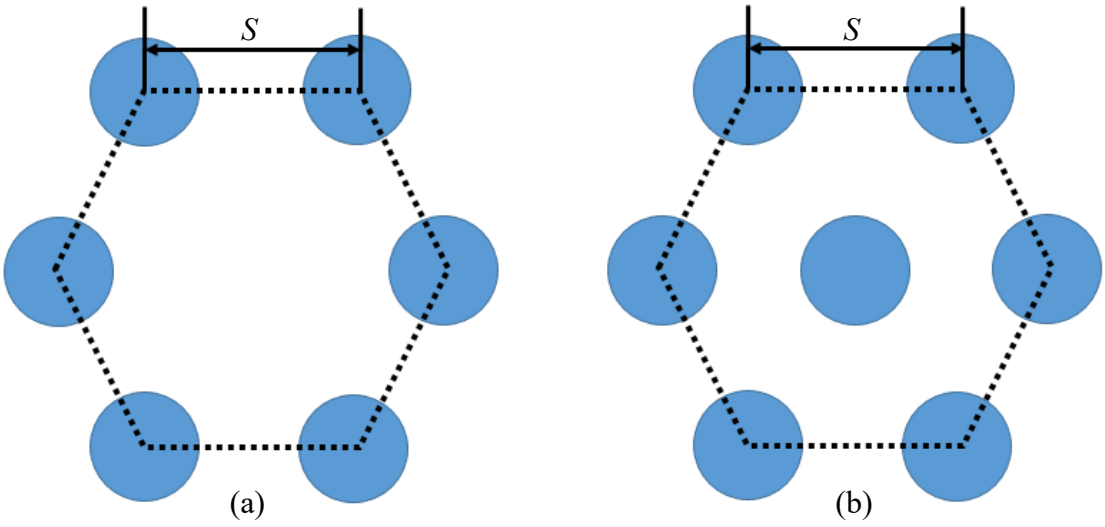

Fig. 63. Schematic diagram of a hexagonal arrangement with (a) six and (b) seven droplet trains

Droplet impingement experiments were conducted to determine droplet properties, such as droplet diameter, droplet impingement frequency and droplet Weber number. Table 15 and 16 show the experimental conditions and variables for a hexagonal arrangement with six and seven droplet trains, respectively.

Table 16. Experimental conditions and variables for a hexagonal arrangement with six droplet trains

Experimental variables	Range
Flow rate per droplet train, Q (mL/h)	70-100
Droplet impingement frequency, f (Hz)	5500-8000
Orifice diameter, d_{orf} (μm)	100
Horizontal impact spacing, S (mm)	0.7-1.8
Droplet diameter, d_d (μm)	186-192
Droplet impingement velocity, V_d (m/s)	2.73-3.94
Droplet Weber number, $We = \frac{\rho d_d V_d^2}{\sigma}$	157-324
Droplet Reynolds number, $Re_{d_d} = \frac{V_d d_d}{\nu}$	1287-1837

Table 17. Experimental conditions and variables for a hexagonal arrangement with seven droplet trains

Experimental variables	Range
Flow rate per droplet train, Q (mL/h)	70-100
Droplet impingement frequency, f (Hz)	5500-8000
Orifice diameter, d_{orf} (μm)	100
Horizontal impact spacing, S (mm)	0.7-1.75
Droplet diameter, d_d (μm)	186-192
Droplet impingement velocity, V_d (m/s)	2.71-3.90
Droplet Weber number, $We = \frac{\rho d_d V_d^2}{\sigma}$	156-316
Droplet Reynolds number, $Re_{d_d} = \frac{V_d d_d}{\nu}$	1284-1829

As shown in Table 16 and 17, flow rate of the cooling liquid varied from 70 to 100 mL/h for each droplet train. For each flow rate considered, a wide range of impact spacings (0.7-1.8 mm for a hexagonal arrangement of six droplet trains, 0.7-1.75 mm for a hexagonal arrangement of seven droplet trains) were used in the experiments. The effects of impact spacing and impingement pattern on droplet-induced hydrodynamics and surface heat transfer are presented below.

High speed images were taken from below of the heater to observe the surface flows induced by a hexagonal arrangement with six and seven droplet trains. Fig. 64 shows a group of surface flow images with different impact spacings and impingement patterns. As shown in Fig. 64, surface jet flows were observed among the impact craters. Furthermore, surface jet flows become more chaotic when flow rate increases or impact spacing decreases, which is consistent with triangulated droplet train impingement results (Section 4.3).

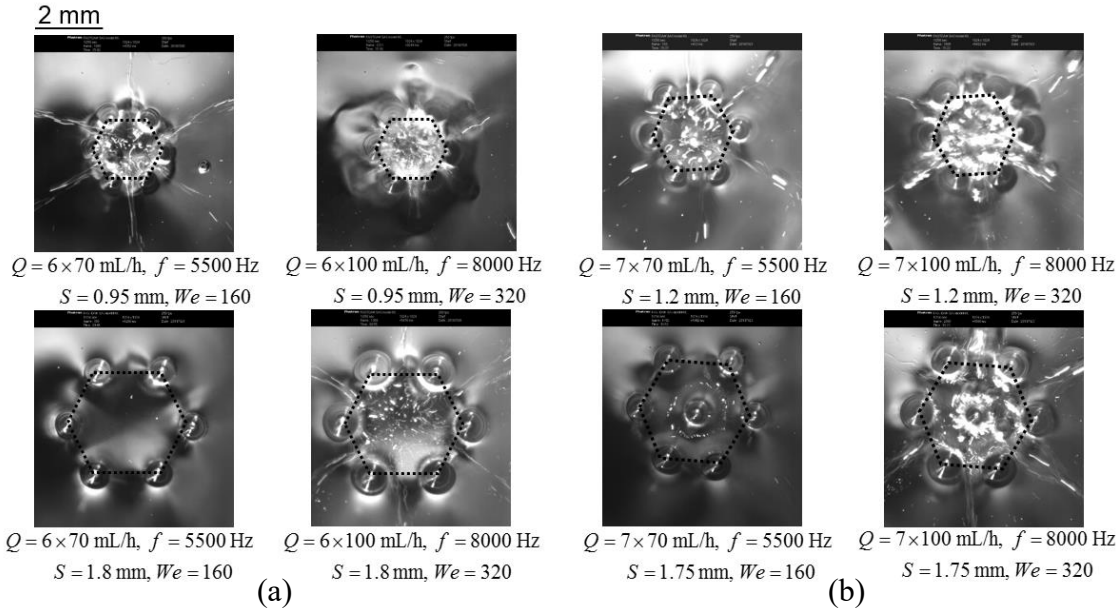

Fig. 64. Bottom view of a hexagonal arrangement with (a) six and (b) seven droplet trains at different impact spacing and flow rate conditions

The effects of impact spacing on surface temperature have also been investigated for a hexagonal arrangement with six and seven droplet trains. Average temperatures

were measured on a hexagonal area ($\overline{T}_{hex}$), as shown by the dash lines denoting the hexagonal area in Fig. 63 and 64. The six vertexes of the hexagonal area coincide with the six center points of droplet impingement. Fig. 65 through 68 show the effects of impact spacing on heat transfer performance for a hexagonal arrangement with six and seven droplet trains.

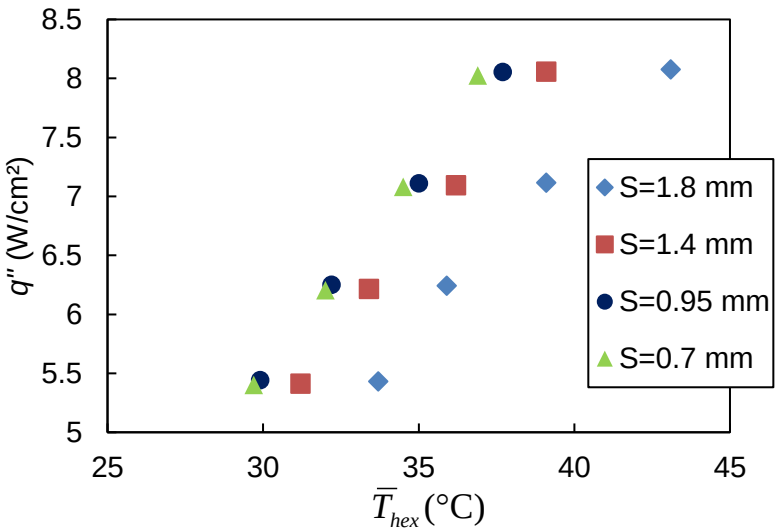

Fig. 65. Effects of impact spacing on heat transfer performance for a hexagonal arrangement with six droplet trains, Q = 6*80 mL/h, We = 210

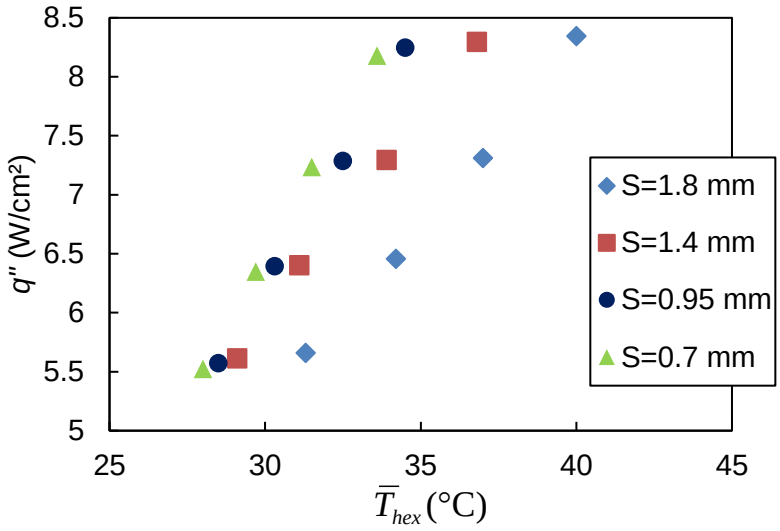

Fig. 66. Effects of impact spacing on heat transfer performance for a hexagonal arrangement with six droplet trains, Q = 6*100 mL/h, We = 320

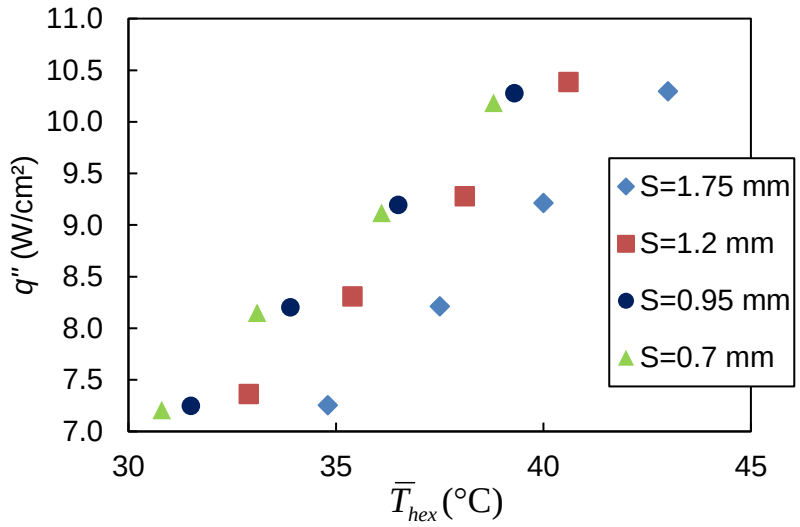

Fig. 67. Effects of impact spacing on heat transfer performance for a hexagonal arrangement with seven droplet trains, Q = 7*80 mL/h, We = 210

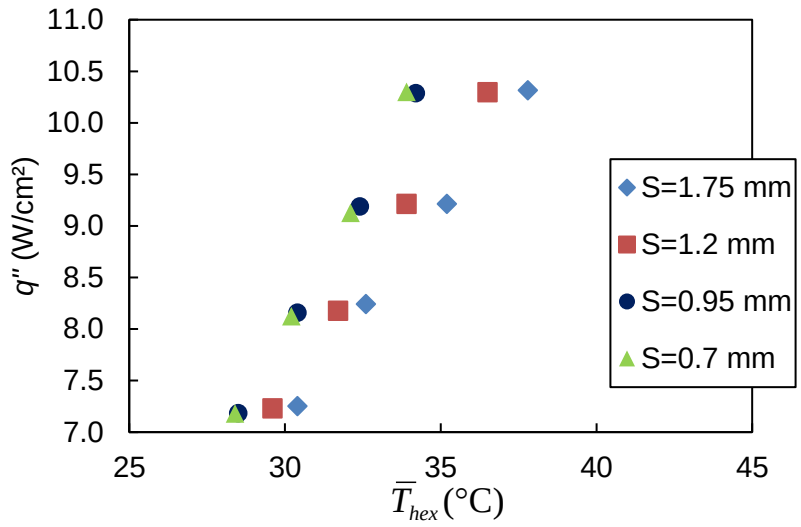

Fig. 68. Effects of impact spacing on heat transfer performance for a hexagonal arrangement with seven droplet trains, Q = 7*100 mL/h, We = 320

As shown in Fig 65 through 68, at fixed flow rate conditions, lower impact spacing leads to better heat transfer performance for a hexagonal arrangement with six and seven droplet trains. Similar heat transfer characteristics have been observed for micro-jet array impingement cooling, as illustrated in Fabbri and Dhir [91]. Fabbri and Dhir [91] claimed that lower impact spacing leads to higher Nusselt number for micro-jet array impingement cooling. Fabbri and Dhir [91] also found that Nusselt number decreases exponentially with impact spacing.

It should be noted that the heat transfer characteristics of double, triple and hexagonal droplet train impingement arrays are different because of the hydrodynamic nature of the surface flows outside each impingement zone. As shown in Section 4.2,

higher impact spacing for double droplet train impingement was found to be more favorable for heat transfer. For triangulated droplet train impingement, it was found that there is an optimum impact spacing for heat transfer. However, for hexagonal droplet train impingement arrays, it was found that lower impact spacing is more favorable for heat transfer within the impingement zone. The different heat transfer characteristics for different impingement patterns are due to the different flow fields within the droplet-induced liquid film.

Fig. 69 through 72 show the temperature profiles across two diagonal impact craters for a hexagonal arrangement with six and seven droplet trains. In Fig. 69 through 72, the position of "0" represents the geometric center of the impingement patterns.

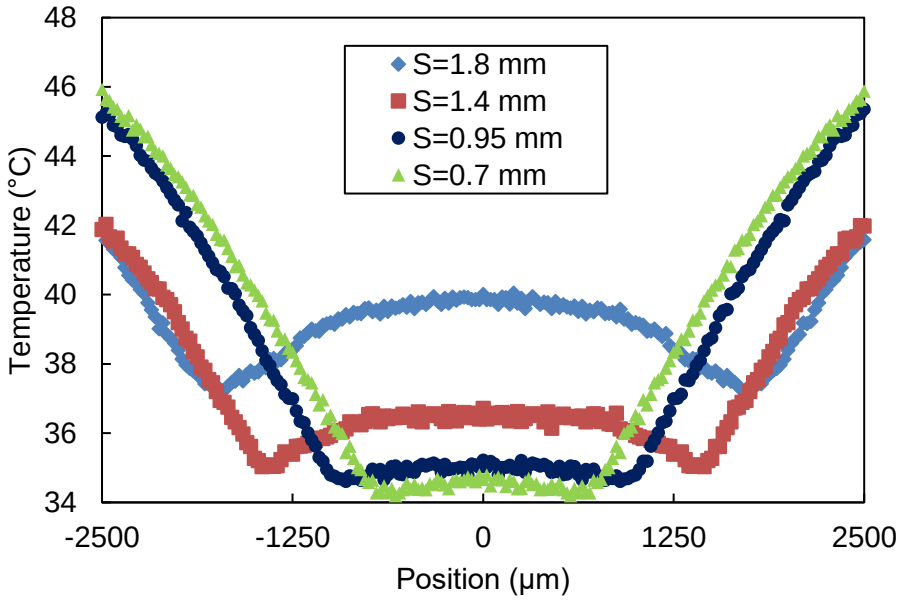

Fig. 69. Effects of impact spacing on temperature distribution for a hexagonal arrangement with six droplet trains, *q"* = 7.1 W/cm², *Q* = 6*80 mL/h, *We* = 210

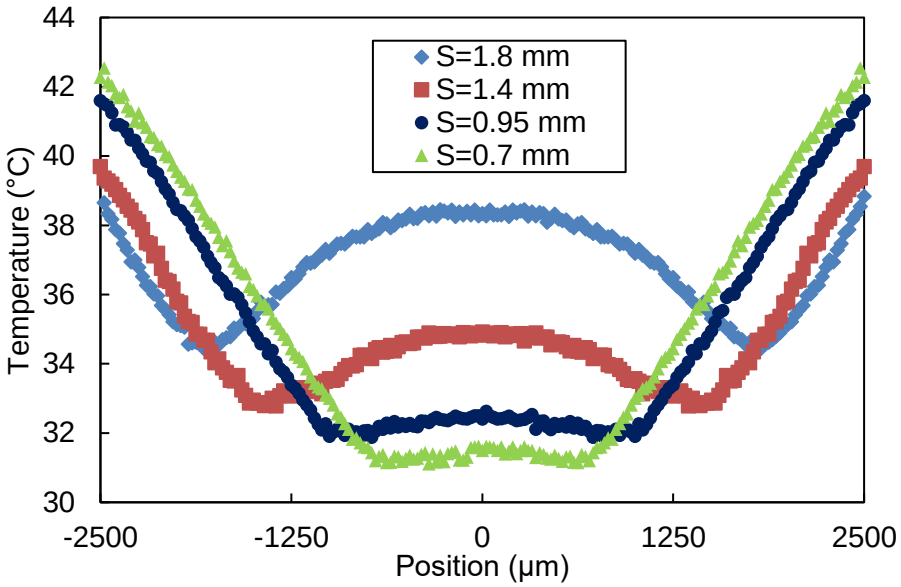

Fig. 70. Effects of impact spacing on temperature distribution for a hexagonal arrangement with six droplet trains, q'' = 7.3 W/cm², Q = 6*100 mL/h, We = 320

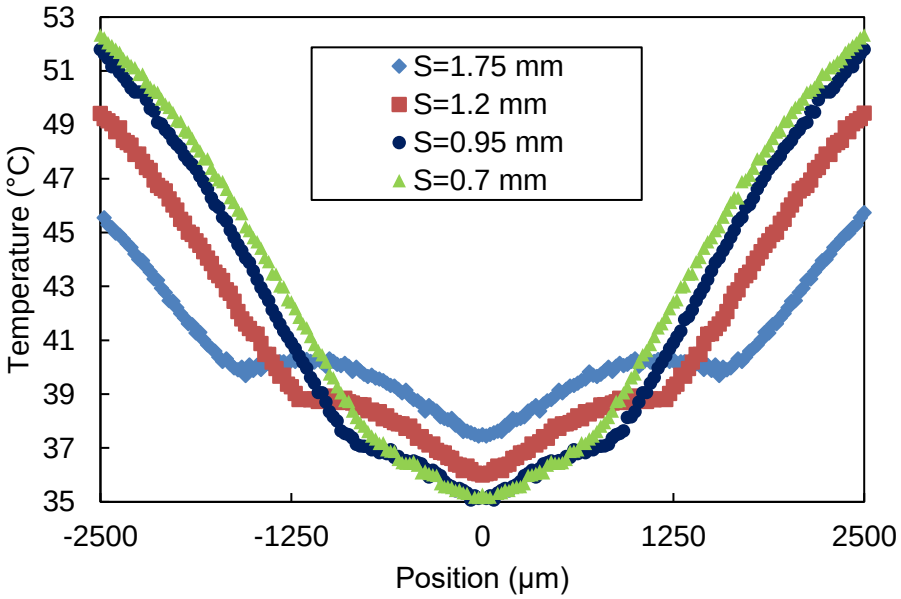

Fig. 71. Effects of impact spacing on temperature distribution for a hexagonal arrangement with seven droplet trains, q'' = 9.2 W/cm², Q = 7*80 mL/h, We = 210

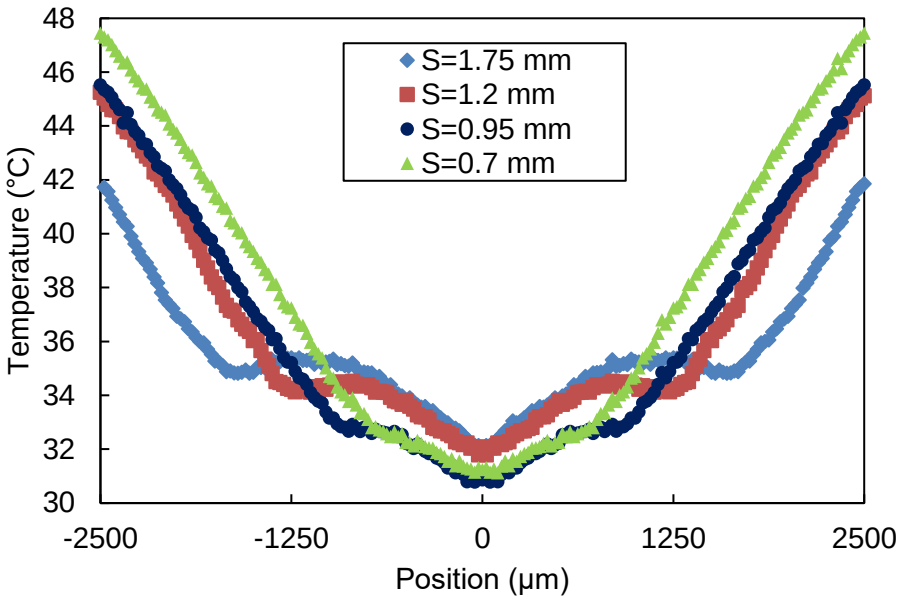

Fig. 72. Effects of impact spacing on temperature distribution for a hexagonal arrangement with seven droplet trains, q'' = 9.2 W/cm², Q = 7*100 mL/h, We = 320

As shown in Fig. 69 through 72, lower impact spacing leads to better heat transfer performance locally (i.e. within the droplet impingement zone), which is consistent with the results shown in Fig. 65 through 68. Furthermore, higher impact spacing leads to lower surface temperatures globally (i.e. outside the droplet impingement zone), which could be attributed to a more uniform distribution of liquid across the surface at higher impact spacing conditions. In Fig. 69 and 70, higher surface temperatures were observed in the central area of the impingement zone for a hexagonal arrangement with six droplet trains, specifically at high impact spacing conditions (S = 1.8 and 1.4 mm). The higher surface temperatures could be attributed to the accumulation of heated liquid in the central area. Nevertheless, for a hexagonal arrangement with seven droplet trains, the lowest surface temperature always coincide

with the geometric center of the impingement zone, as shown in Fig. 71 and 72. The results indicate that impingement pattern plays a significant role in surface temperature distribution.

The effects of impact spacing and flow rate on Nusselt number were investigated using average surface temperature ($\overline{T}_{hex}$), initial droplet temperature (T_0), droplet diameter (d_d) and heat flux value (q''), as follows:

$$\overline{Nu}_{d_d} = \frac{q''}{\left(\overline{T}_{hex} - T_0\right)} \cdot \frac{d_d}{k_l} \tag{44}$$

Nusselt number correlations were obtained using similar mathematical forms as described in reference [89-91] for circular jet impingement arrays, as follows:

$$\overline{Nu}_{d_d} = K \cdot \mathrm{Pr}^{1/3} \cdot \mathrm{Re}_{d_d}^{a} \cdot \exp\left(b \frac{S}{d_d}\right) \tag{45}$$

In Equation 44, the exponent of 1/3 for Prandtl number was chosen because only one fluid was tested in the current study. Furthermore, Soriano et al. [55] have shown that Nu scales with $\mathrm{Pr}^{1/3}$ in droplet train impingement heat transfer experiments. Based on regression analysis, Equations 46 and 47 are proposed for a hexagonal arrangement with six and seven droplet trains, respectively, as follows:

$$\overline{Nu}_{d_d} = 3.905 \times 10^{-3} \cdot \mathrm{Pr}^{1/3} \cdot \mathrm{Re}_{d_d}{}^{1.042} \cdot \exp(-0.05236 \frac{S}{d_d}), \mathrm{R}^2 = 0.96 \tag{46}$$

$$\overline{Nu}_{d_d} = 3.507 \times 10^{-4} \cdot \mathrm{Pr}^{1/3} \cdot \mathrm{Re}_{d_d}{}^{1.386} \cdot \exp(-0.04242 \frac{S}{d_d}), \mathrm{R}^2 = 0.98 \tag{47}$$

Fig. 73 and 74 show the effects of non-dimensional impact spacing (S/d_d) on Nusselt number for a hexagonal arrangement with six and seven droplet trains,

respectively. As shown in Fig. 73 and 74, a good agreement was reached between experimental data and the predictions given by Equations 46 and 47. Furthermore, at fixed flow rate conditions, Nusselt number decreases with impact spacing, which is consistent with the results shown in Fabbri and Dhir [91] for micro jet array impingement cooling. The results further validate that impact spacing plays a significant role in multiple droplet train impingement cooling.

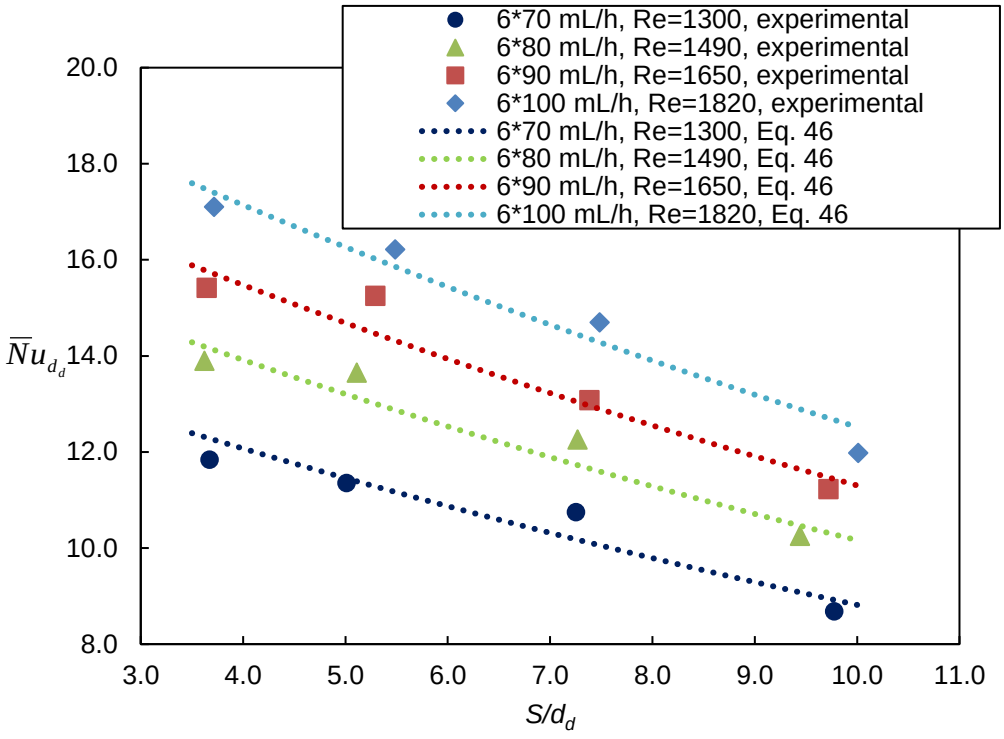

Fig. 73. Effects of impact spacing on Nusselt number for a hexagonal arrangement with six droplet trains

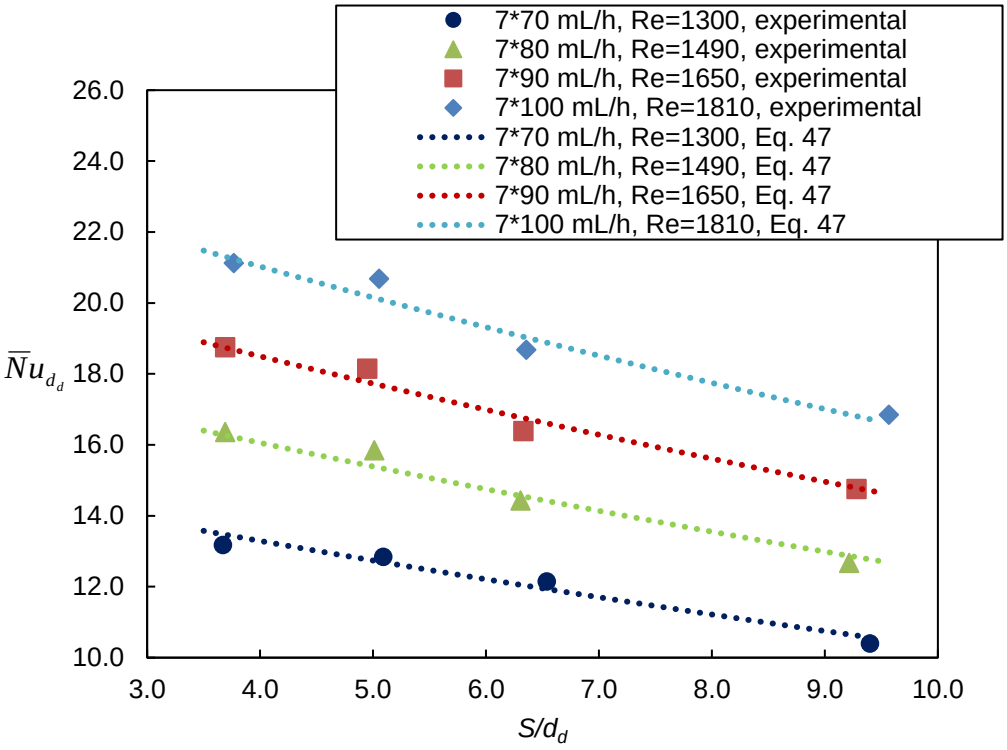

Fig. 74. Effects of impact spacing on Nusselt number for a hexagonal arrangement with seven droplet trains

4.5. Comparison between circular jet impingement cooling and droplet train impingement cooling

In this section, comparisons between circular jet impingement and droplet train impingement are presented. Various impingement patterns, such as single, double, triple and hexagonal-arranged jets are considered in this section. Results show that droplet train impingement leads to better heat transfer performance for various impingement patterns, as described below.

4.5.1. Comparison between single circular jet impingement and single droplet train impingement

In this sub-section, comparisons between single circular jet impingement and single droplet train impingement are analyzed and discussed. Table 18 shows the experimental conditions and variables considered in this section. Orifice diameter (d_{orf}) was fixed at 150 µm for all the cases shown in Table 18.

Table 18. Experimental conditions and variables for the comparison between single droplet train and single circular jet impingement, d_{orf} =150 µm

Input variable	Experimental values							
	Droplet train					Circular jet		
Q (mL/h)	f (Hz)	d_d (µm)	V_d (m/s)	Re_{d_d}	We	d_j (µm)	V_j (m/s)	Re_j
165	6000	240	3.23	1938	280	150	2.59	970
180	6300	237	3.52	2086	328	150	2.83	1058
195	6400	252	3.77	2375	400	150	3.07	1147
210	6500	249	3.99	2484	443	150	3.30	1235
225	7200	260	4.45	2893	575	150	3.54	1323

As shown in Table 18, comparisons between single droplet train impingement and single circular jet impingement were performed at fixed flow rate and fixed orifice diameter conditions. Properties of the droplet trains are exactly the same as shown in Table 3 (Section 4.1.1), which were used for droplet-induced crown propagation analysis. It was found that the diameter of the circular jet (d_j) is equal to orifice diameter (d_{orf}) for all the cases considered. Circular jet velocity (V_j) and circular jet Reynolds number (Re_j) were calculated using Equations 48 and 49, as follows:

$$V_j = \frac{4 \cdot Q}{\pi \cdot \left(d_j\right)^2} \tag{48}$$

$$\mathrm{Re}_j = \frac{V_j \cdot d_j}{\nu} \tag{49}$$

The Reynolds number for each droplet impingement case was calculated using Equation 34. Hydrodynamics of the circular jet impingement have been investigated experimentally. Specifically, crater diameter was measured experimentally and calculated using Equations 50 and 51, which were proposed by Bohr et al. [93] and Bush and Aristoff [94] for circular jet impingement, respectively, as follows:

$$d_{cra} = 1.46 \cdot \left(\frac{Q}{2\pi}\right)^{5/8} \nu^{-3/8} g^{-1/8} \tag{50}$$

$$\frac{d_{cra} \cdot g \cdot H_{out}^2 \cdot d_j^2}{8Q^2} \cdot \left(1 + \frac{4}{B_o}\right) + \frac{d_j^2}{4\pi^2 \cdot d_{cra} \cdot H_{out}} = 0.01676 \cdot \left[\left(\frac{d_{cra}}{d_j}\right)^3 \cdot \frac{2}{\mathrm{Re}_j} + 0.1826\right]^{-1} \tag{51}$$

In Equation 51, H_{in} and H_{out} are the film thickness inside and outside the impact crater, respectively. $B_o = \rho \cdot g \cdot d_{cra} \cdot \left(H_{out} - H_{in}\right)/\sigma$ is the Bond number of the hydraulic jump. H_{in} and H_{out} were measured using the methodologies developed by Soriano [54], which were based on total internal reflection method. Table 19 shows the values of H_{in} and H_{out} for circular jet impingement. As shown in Table 19, H_{in} is about 15 μm (± 2 μm) and H_{out} is about 88 μm (± 2 μm) for different Reynolds numbers.

Table 19. Film thickness inside and outside impact craters for circular jet impingement

Q (mL/h)	Re_j	H_{in} (μm)	H_{out} (μm)
165	970	14	86
180	1058	15	87
195	1147	18	90
210	1235	15	88
225	1323	12	87
Average values (μm)		15	88
Standard deviation (μm)		2	2

Fig. 75 shows the bottom view of the impact craters for single circular jet impingement and the comparison with droplet train impingement.

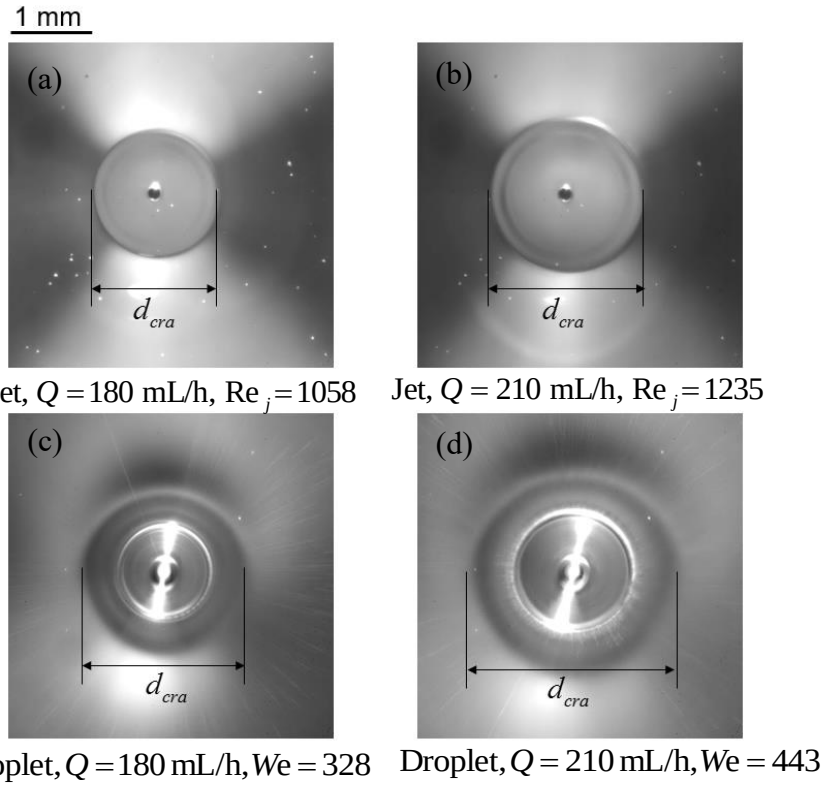

Fig. 75. Bottom view of circular jet impingement and droplet train impingement without heat transfer

As shown in Fig. 75, impact craters were formed for both droplet train impingement and circular jet impingement cases. Furthermore, it was observed that droplet train impingement leads to higher crater diameter at fixed flow rate conditions as seen in Fig. 76. Fig. 76 and Table 20 show the experimental values for crater diameter for droplet train impingement and circular jet impingement cases, and the predictions given by Equations 50 and 51.

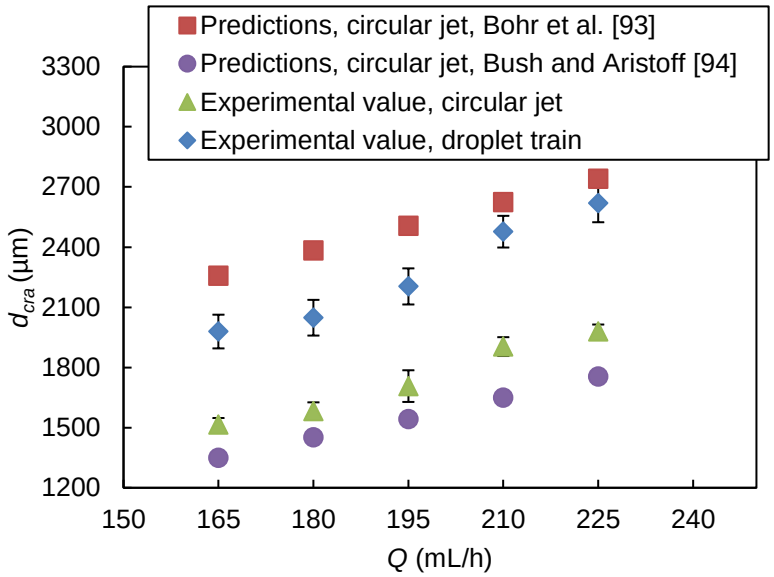

Fig. 76. Crater diameter for droplet train and circular jet impingement, and comparison with the predictions given by Bohr et al. [93] and Bush and Aristoff [94]

Table 20. Crater diameter for droplet train and circular jet impingement

Input variable	Theoretical values for circular jet, $d_{cra,\,th}$ (μm)		Experimental values for circular jet and droplet train			
			Jet			Droplet
Q (mL/h)	Eq. 50	Eq. 51	$d_{cra,\,exp}$ (μm)	Relative error, $(d_{cra,\,th} - d_{cra,\,exp})/d_{cra,\,exp}$ (%)		$d_{cra,\,exp}$ (μm)
				Eq. 50	Eq. 51	
165	2257	1350	1516	49	-11	1979
180	2383	1452	1583	51	-8	2048
195	2506	1542	1707	47	-10	2204
210	2625	1650	1904	38	-13	2477
225	2740	1755	1980	38	-11	2619

As shown in Fig. 76 and Table 20, droplet train impingement leads to higher crater diameter than circular jet impingement at fixed flow rate conditions. This suggests that the periodic nature of droplet train impingement is more favorable in terms of extending the thin film region. Furthermore, it was found that the model proposed by Bohr et al. [93] (i.e. Equation 50) greatly over-predicts the jet-induced crater diameter. However, predictions given by the model proposed by Bush and Aristoff [94] (i.e. Equation 51) agree well with the experimental data. It should be noted that Equation 50 does not take into account surface tension effects. On the other hand, Equation 51 takes into account surface tension effects within the hydraulic jump region. The results indicate the surface tension is a significant factor in the formation of hydraulic jump for micro scale circular jet impingement. From Fig.76 and Table 20, it can be observed that droplet impingement leads to greater crater diameter by up to 30%. The increase in crater diameter can be attributed to higher droplet velocity when compared to the velocity of the fluid jet, which results in greater momentum.

Comparisons of the heat transfer performance induced by single circular jet and droplet train impingement have also been performed. Figure 77 and 78 compare the heat transfer performance of single circular jet and droplet train impingement at fixed flow rate conditions.

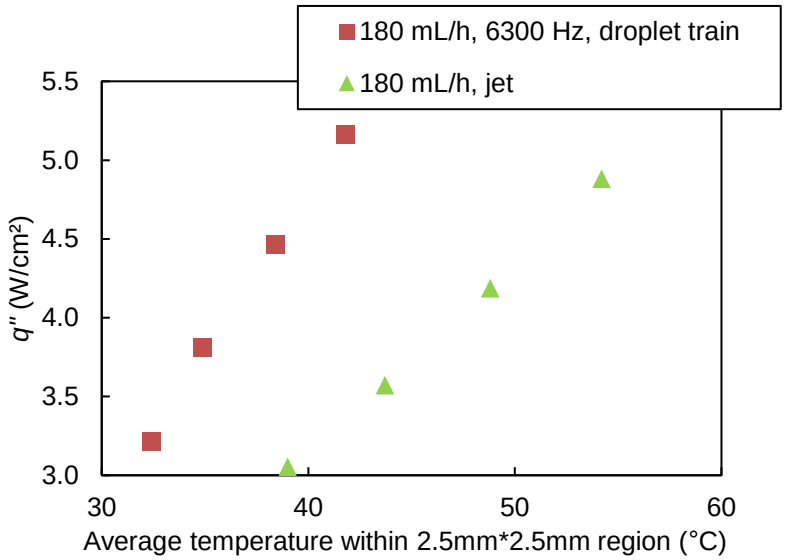

Fig. 77. Comparison of heat transfer performance for single droplet train and circular jet impingement, *Q*=180 mL/h

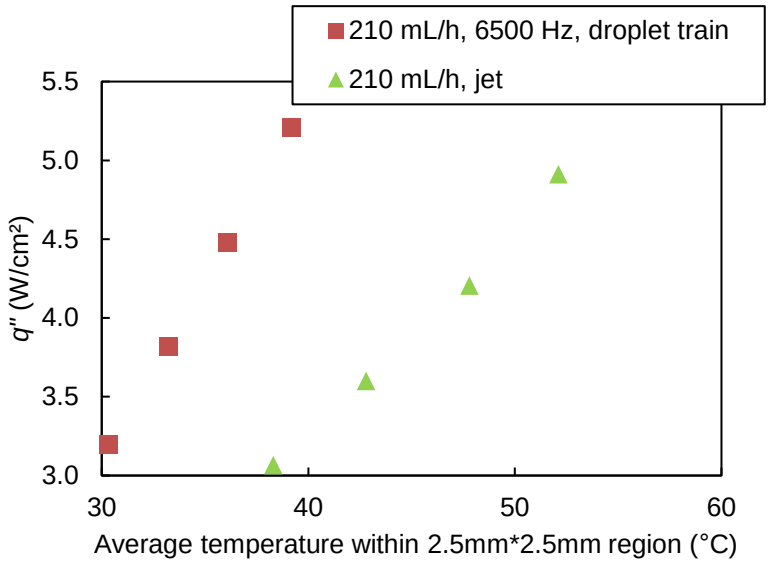

Fig. 78. Comparison of heat transfer performance for single droplet train and circular jet impingement, *Q*=210 mL/h

As shown in Fig. 77 and 78, droplet train impingement leads to better heat transfer performance at fixed flow rate conditions. The heat transfer results suggest that the periodic droplet-induced crown propagation leads to a more effective mixing of the cooling liquid, which improves the liquid usage efficiency during the heat transfer process [59]. The results clearly indicate that the sweeping motion of the propagating droplet is capable of suppressing the thermal boundary layer growth seen in laminar micro-jet cases, when the flowrate is held constant [59, 60], which explains the enhanced thermal performance seen in Fig. 77 and 78.

Fig. 79 and 80 show the temperature profiles across impact craters for single droplet train and single circular jet impingement.

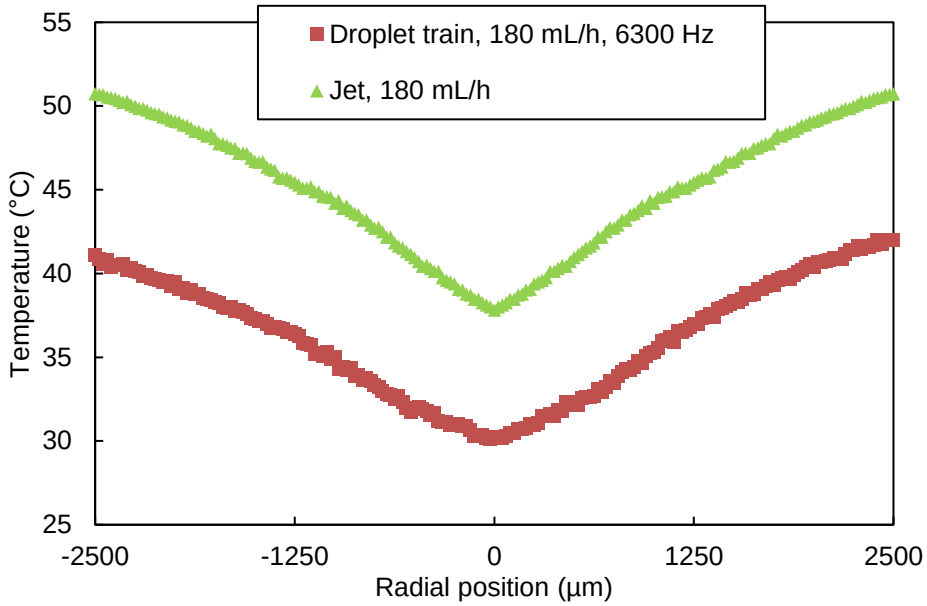

Fig. 79. Temperature distribution across impact craters for single droplet train and circular jet impingement at a flow rate of 180 mL/h, q''=3.7 W/cm²

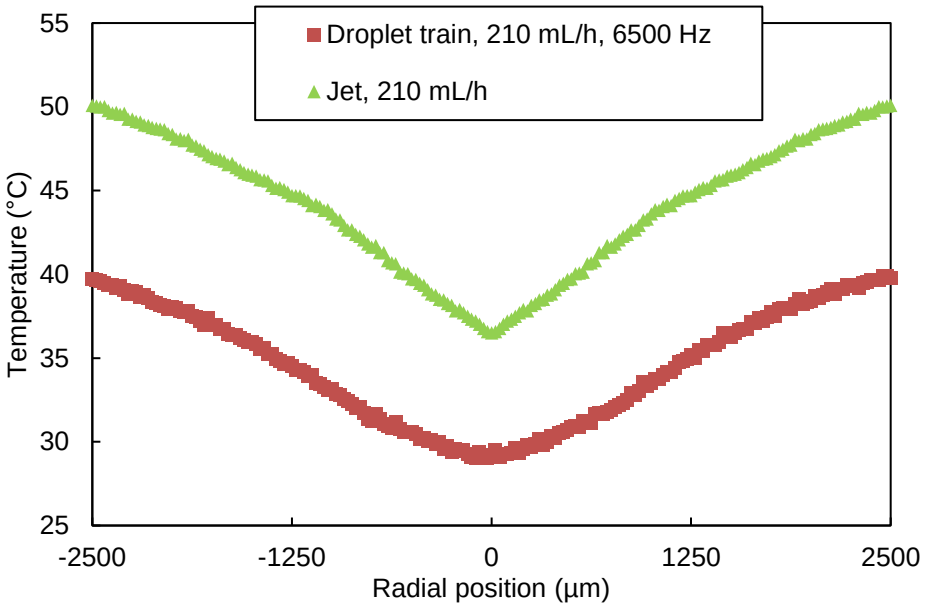

Fig. 80. Temperature distribution across impact craters for single droplet train and circular jet impingement at a flow rate of 210 mL/h, q''=3.7 W/cm²

As shown in Fig. 79 and 80, droplet train impingement leads to lower temperature profiles than circular jet impingement, which is consistent with the results shown in Fig. 77 and 78. Furthermore, it was found that temperature profiles are smoother for droplet train impingement. This could be due to the periodic nature of droplet train impingement, which leads to a more effective thermal and fluid mixing during heat transfer process [59].

The experimental local Nusselt number profiles for single droplet train impingement and circular jet impingement were obtained based on the methodologies described in Soriano et al. [55]. Nusselt numbers were calculated at different radial positions using local surface temperatures ($T(r)$), initial droplet temperature (T_0), orifice diameter (d_{orf}) and heat flux value (q'') [55], as follows:

$$Nu_{d_{orf}}(r) = \frac{q''}{T(r) - T_0} \frac{d_{orf}}{k_l} \tag{52}$$

Nusselt number correlations were obtained using Equations 53 through 55. Fig. 81 and 82 show the Nusselt number profiles and the predictions given by Equations 53 through 55.

$$Nu_{d_{orf}}(r) = A \mathrm{Re}_{d_{orf}}^{1/2} \mathrm{Pr}^{1/3}, 0 \le r / d_{orf} \le 1 \tag{53}$$

$$Nu_{d_{orf}}(r) = A \mathrm{Re}_{d_{orf}}^{1/2} \mathrm{Pr}^{1/3} \left(\frac{d_{orf}}{r} \right)^b, r / d_{orf} > 1 \tag{54}$$

$$\begin{aligned} \mathrm{Re}_{d_{orf}} &= \frac{V_d \cdot d_{orf}}{\nu} \\ \mathrm{Re}_{d_{orf}} &= \mathrm{Re}_{d_d} \cdot \frac{d_{orf}}{d_d} \end{aligned} \tag{55}$$

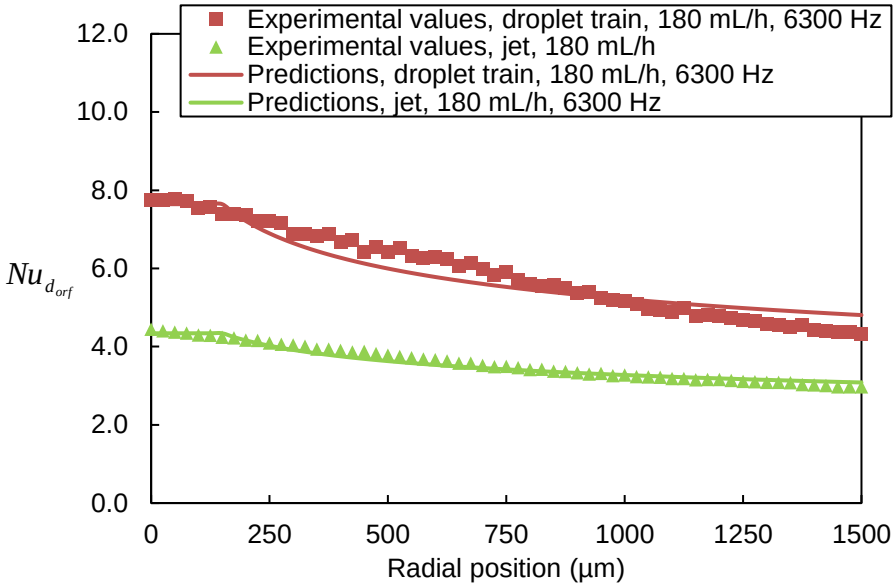

Fig. 81. Comparison of Nusselt number profiles for single droplet train impingement and circular jet impingement, Q =180 mL/h

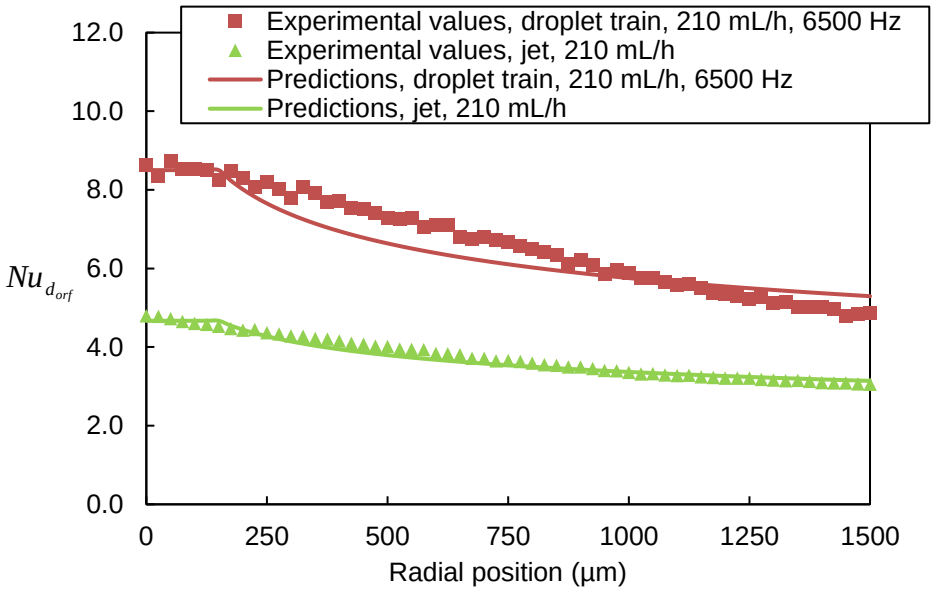

Fig. 82. Comparison of Nusselt number profiles for single droplet train impingement and circular jet impingement, Q =210 mL/h

The values of coefficients *A* and *b* in Equation 53 and 54, and R^2 values of the correlations are shown in Table 20, as follows:

Table 21. Nusselt number correlation coefficients for single droplet train and single circular jet impingement

	Single droplet train				Single circular jet		
Q (mL/h)	*f* (Hz)	*A*	*b*	R^2	*A*	*b*	R^2
180	6300	0.097	0.20	0.91	0.059	0.15	0.98
210	6500	0.101	0.21	0.87	0.061	0.17	0.97

As shown in Fig. 81, 82 and Table 21, single droplet train impingement leads to higher Nusselt number profiles at fixed flow rate conditions, which is consistent with the results shown in Fig. 79 and 80. Furthermore, it was found that the R^2 values of circular jet impingement correlations are higher than droplet train impingement. This is because the methodologies used by Soriano et al. [55] was based on the Liu model [61], which was developed for circular jet impingement. As a result, the experimental circular jet impingement data should fit better with the predictions. Furthermore, the Liu model [61] cannot fully capture the periodic nature of the droplet impingement process described above.

4.5.2. Comparison between multiple circular jet impingement and multiple droplet train impingement

In this sub-section, the comparisons between multiple circular jet impingement and multiple droplet train impingement are analyzed and discussed. Table 22 shows the experimental conditions and variables considered in this section.

Table 22. Experimental conditions and variables for the comparison between multiple droplet train and multiple circular jet impingement

Input variable			Experimental values						
			Droplet trains				Circular jet		
Impingement pattern	Q (mL/h)	S (mm)	d_d (μm)	V_d (m/s)	Re_{d_d}	We	d_j (μm)	V_j (m/s)	Re_j
Double	2*195	0.65	240	4.02	2406	434	150	3.07	1147
Triangulated	3*90	1.1	188	3.49	1636	256	100	3.18	794
Hexagonal-6	6*100	1.8	186	3.91	1827	316	100	3.54	882
Hexagonal-7	7*100	1.75	186	3.88	1800	310	100	3.54	882

As shown in Table 22, comparisons between multiple droplet train and multiple circular jet impingement were performed at fixed flow rate and impact spacing conditions. It should be noted only one flow rate and one impact spacing were considered for each impingement pattern. This because the experimental setup used in the current study was designed for droplet train impingement experiments. As shown in Section 3.1 (experimental setup section), the droplet generator has limited ability to produce stable circular jets in a wide range of experimental conditions. Comparison of the heat transfer and hydrodynamics between multiple droplet train and multiple circular jet impingement are presented, as follows.

Hydrodynamics of multiple circular jet impingement have been investigated experimentally. Fig. 83 through 86 show the bottom view images of droplet train impingement and circular jet impingement for various impingement patterns.

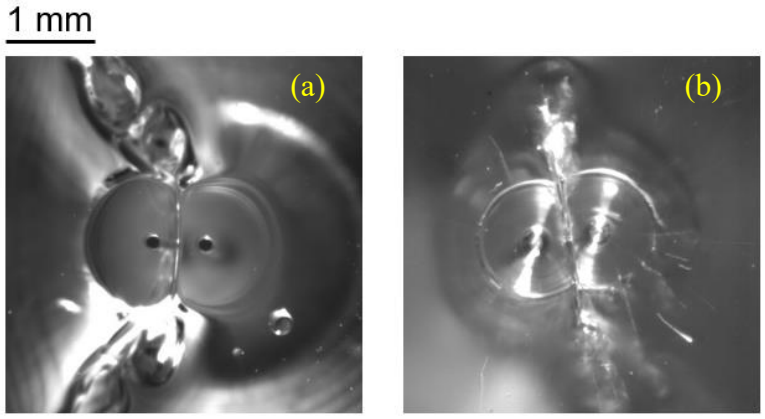

Fig. 83. Bottom view of (a) double jet and (b) double droplet train impingement when no heat was applied, Q = 2*195 mL/h, S = 0.65 mm

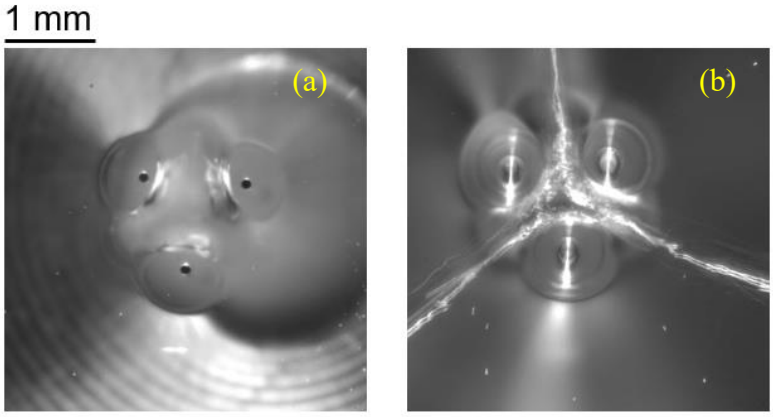

Fig. 84. Bottom view of (a) triangulated jet and (b) triangulated droplet train impingement when no heat was applied, Q = 3*90 mL/h, S = 1.1 mm

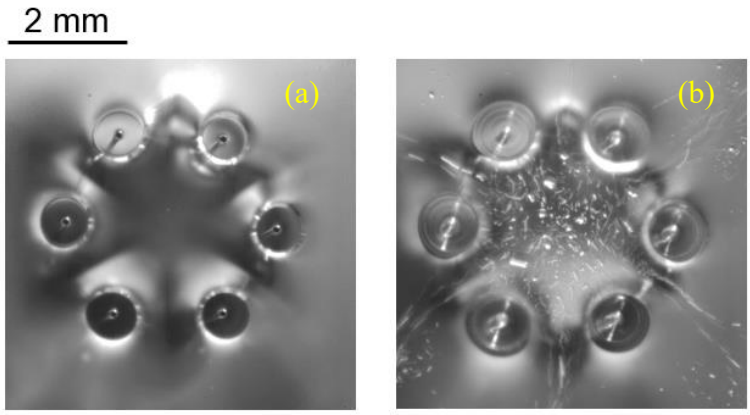

Fig. 85. Bottom view of a hexagonal arrangement with (a) six jets and (b) six droplet trains when no heat was applied, Q = 6*100 mL/h, S = 1.8 mm

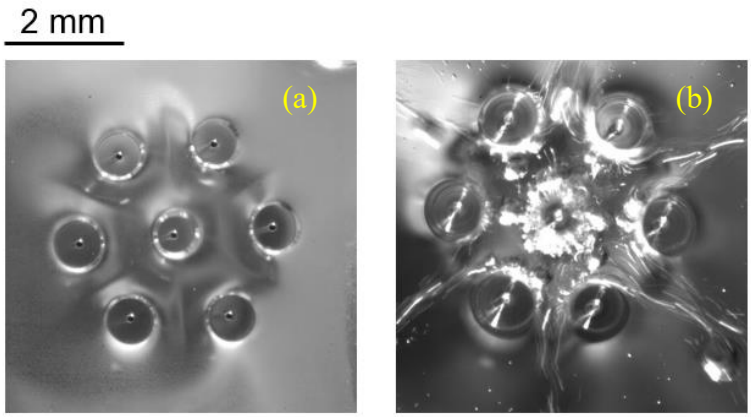

Fig. 86. Bottom view of a hexagonal arrangement with (a) seven jets and (b) seven droplet trains when no heat was applied, Q = 7*100 mL/h, S = 1.75 mm

As shown in Fig. 83 through 86, droplet train impingement arrays lead to stronger interactions among impact craters, specifically for triangulated and hexagonal-arranged impingement patterns. Furthermore, entrapped air bubbles were observed among impact craters for triangulated and hexagonal-arranged droplet train impingement patterns, as shown in Fig. 84(b), 85(b) and 86(b). However, impact craters seemed to be

unperturbed by the surrounding impact craters for triangulated and hexagonal-arranged circular jet impingement patterns, as shown in Fig. 84(a), 85(a) and 86(a). The stronger interactions among droplet impact craters could be due partly to the higher velocity of impinging droplets. As shown in Table 22, the velocity of impinging droplets is higher than circular jets for the same (fixed) flow rate conditions. Furthermore, as Table 22 shows, the diameter of droplets is much greater than for circular jets for various impingement patterns. The higher diameter of impinging droplets may also enhance the interactions among impact craters.

Comparisons of the heat transfer performance induced by multiple circular jet and multiple droplet train impingement have also been performed. Fig. 87 through 90 compare the heat transfer performance for various impingement patterns. In Fig. 87 through 90, average surface temperatures were measured in characteristic areas ($\overline{T}_{line}$, $\overline{T}_{tri}$ and $\overline{T}_{hex}$), as defined in Sections 4.2 through 4.4.

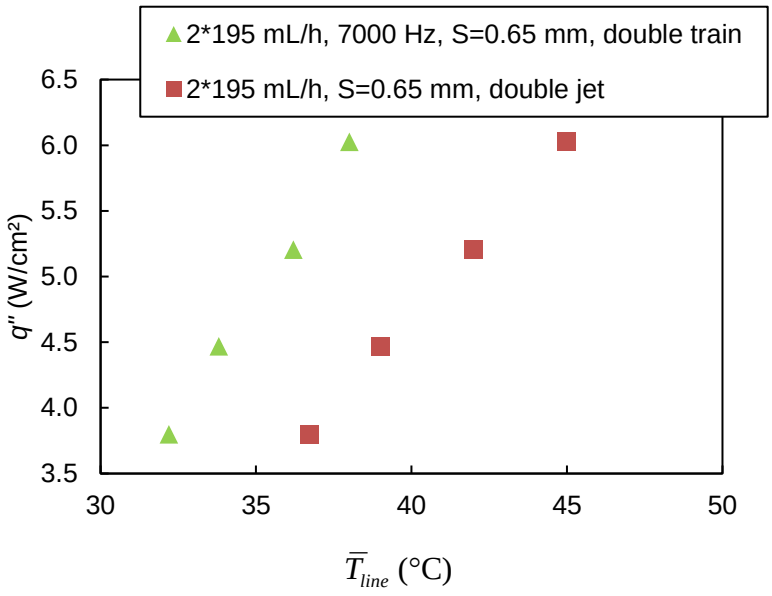

Fig. 87. Comparison of heat transfer performance for double droplet train and double circular jet impingement, Q = 2*195 mL/h, S =0.65 mm

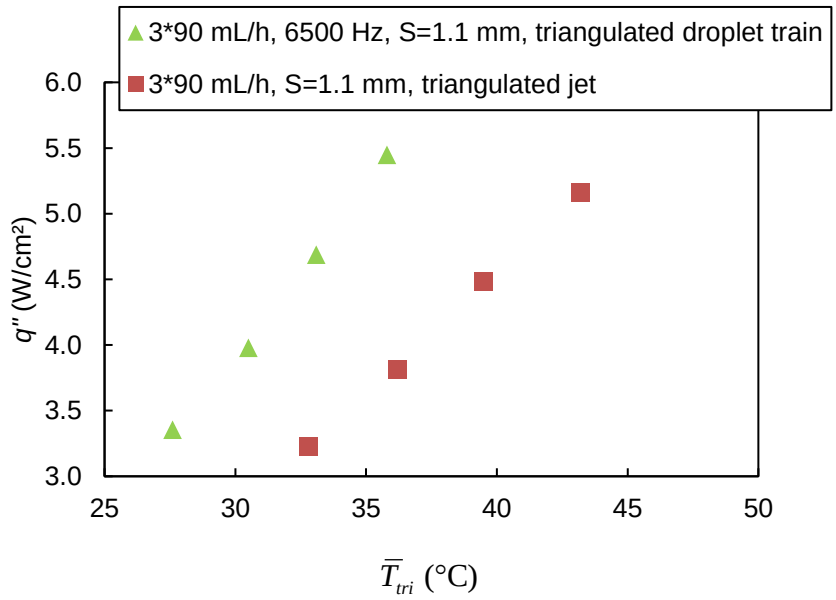

Fig. 88. Comparison of heat transfer performance for triangulated droplet train and triangulated circular jet impingement, Q = 3*90 mL/h, S =1.1 mm

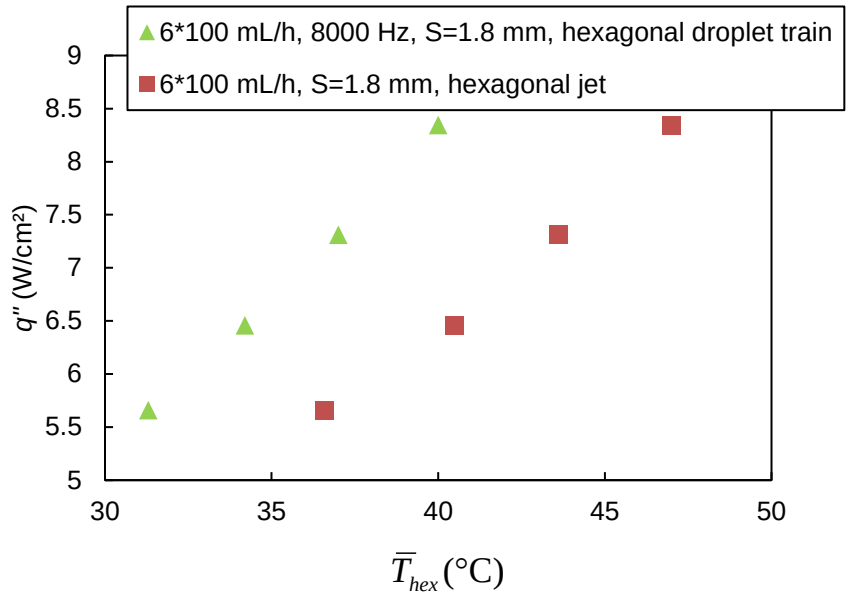

Fig. 89. Comparison of heat transfer performance for a hexagonal arrangement with six droplet trains and six circular jets, Q = 6*100 mL/h, S =1.8 mm

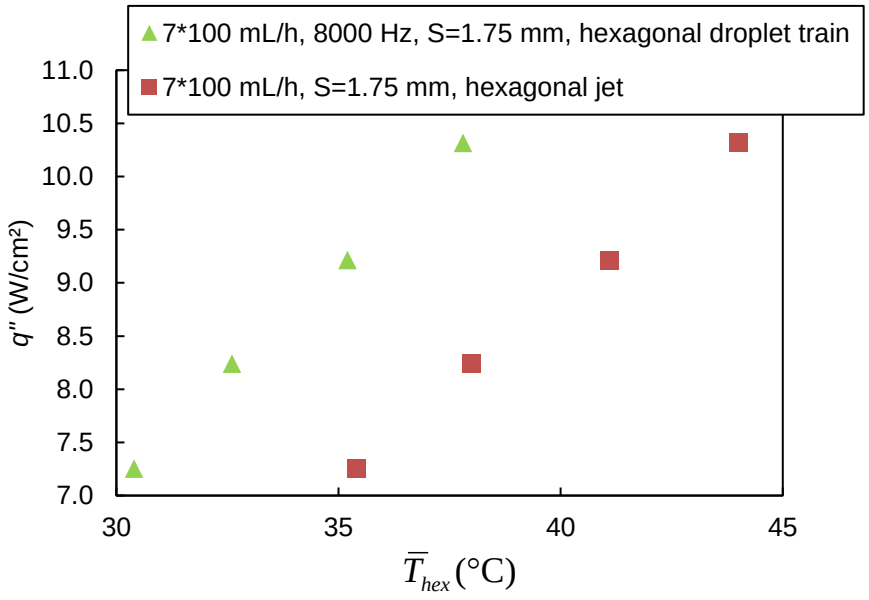

Fig. 90. Comparison of heat transfer performance for a hexagonal arrangement with seven droplet trains and seven circular jets, Q = 7*100 mL/h, S =1.75 mm

As shown in Fig. 87 through 90, droplet train impingement leads to better heat transfer performance for various impingement patterns. The heat transfer results suggest that the periodic droplet-induced crown propagation and interactions among droplet-induced craters lead to a more effective mixing of cooling liquid, which improves the liquid usage efficient during the heat transfer process. Fig. 91 through 94 show the temperature profiles across impact craters for various impingement patterns.

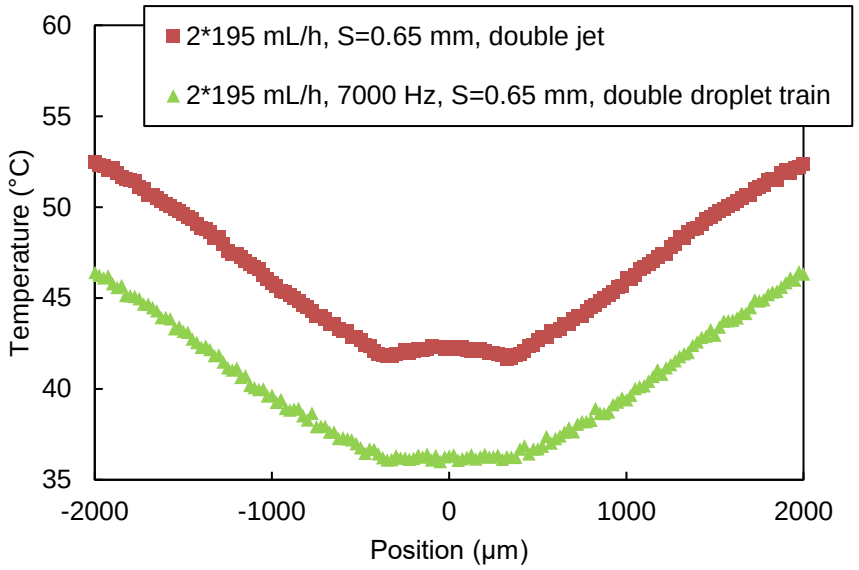

Fig. 91. Temperature profiles across two impact craters for double droplet train and jet impingement, Q = 2*195 mL/h, S = 0.65 mm, q'' = 5.3 W/cm²

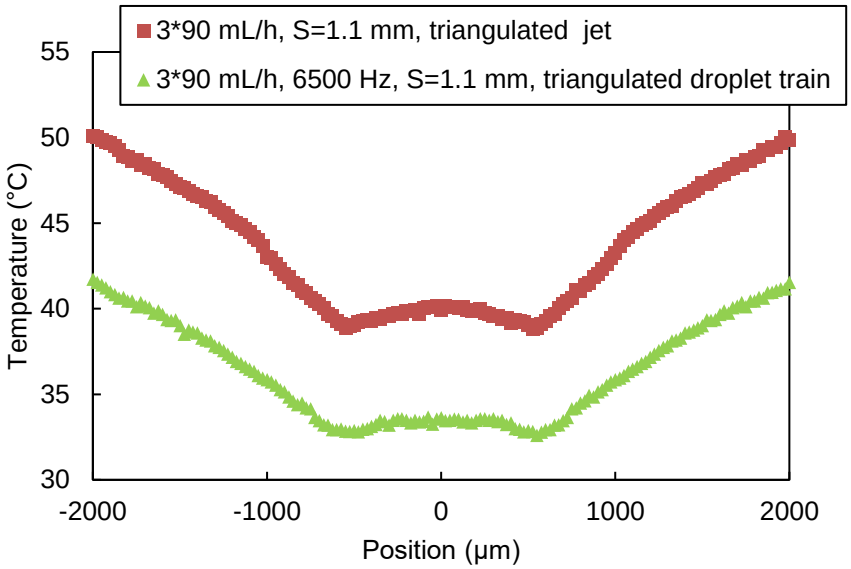

Fig. 92. Temperature profiles across two impact craters for triangulated droplet train and jet impingement, Q = 3*90 mL/h, S = 1.1 mm, q'' = 4.5 W/cm²

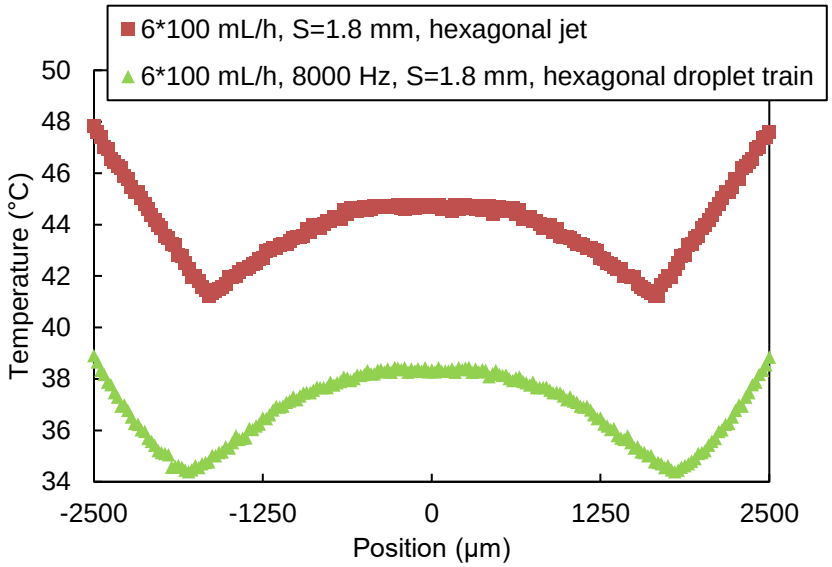

Fig. 93. Temperature profiles across two diagonal impact craters for a hexagonal arrangement with six droplet trains and six jets, Q = 6*100 mL/h, S = 1.8 mm, q'' = 7.3 W/cm²

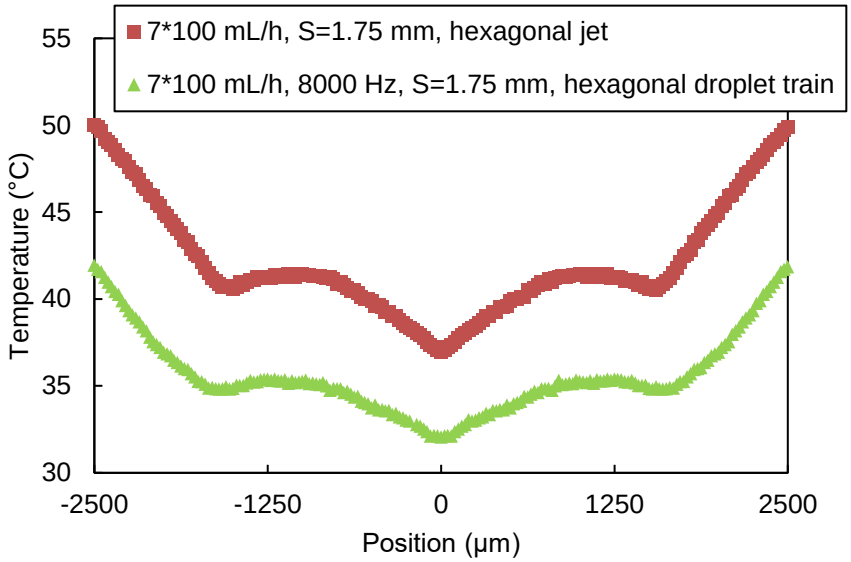

Fig. 94. Temperature profiles across two diagonal impact craters for a hexagonal arrangement with seven droplet trains and seven jets, Q = 7*100 mL/h, S = 1.75 mm, q'' = 9.2 W/cm²

As shown in Fig. 91 through 94, droplet train impingement arrays lead to lower temperature profiles than circular jet impingement arrays for all the impingement patterns considered. This is consistent with the results shown in Section 4.5.1 for single droplet train and single circular jet impingement. It was also found that temperature profiles are smoother for droplet train impingement, specifically for hexagonal impingement patterns, as shown in Fig. 93 and 94. The results indicate that the periodic nature of droplet train impingement and interactions among droplet-induced impact crater lead to a more effective thermal mixing during heat transfer process.

Nusselt number values of circular jet impingement arrays and droplet train impingement arrays have been compared for all the impingement patterns considered. The experimental averaged Nusselt number values were calculated using average surface

temperatures ($\overline{T}_{line}$, $\overline{T}_{tri}$ and $\overline{T}_{hex}$ for double, triple and hexagonal impingement patterns, respectively), orifice diameter (d_{orf}) and initial droplet temperatures (T_0). The experimental average Nusselt numbers for double, triple and hexagonal impingement patterns are calculated using Equations 56, 57 and 58, respectively, as follows:

$$\overline{N}u_{d_{orf}} = \frac{q^{"}}{\left(\overline{T}_{liine} - T_0\right)} \cdot \frac{d_{orf}}{k_l} \tag{56}$$

$$\overline{N}u_{d_{orf}} = \frac{q^{"}}{\left(\overline{T}_{tri} - T_0\right)} \cdot \frac{d_{orf}}{k_l} \tag{57}$$

$$\overline{N}u_{d_{orf}} = \frac{q^{"}}{\left(\overline{T}_{hex} - T_0\right)} \cdot \frac{d_{orf}}{k_l} \tag{58}$$

Table 23 compares the Nusselt values of droplet train and circular jet impingement arrays for various impingement patterns.

Table 23. Comparison of Nusselt number values for multiple droplet train and circular jet impingement arrays

Input variable				Nusselt number values, $\overline{N}u_{d_{orf}}$			
Impingement pattern	Q (mL/h)	S (mm)	d_{orf} (μm)	Equation used	$\overline{N}u_{d_{orf}}$ for jet	$\overline{N}u_{d_{orf}}$ for droplet	Enhancement (%)
Double	2*195	0.65	150	Eq. 56	5.9	8.4	42
Triangulated	3*90	1.1	100	Eq. 57	3.3	4.7	42
Hexagonal-6	6*100	1.8	100	Eq. 58	4.4	6.3	43
Hexagonal-7	7*100	1.75	100	Eq. 58	6.2	8.8	42

As shown in Table 23, at fixed flow rate and fixed impact spacing conditions, droplet train impingement arrays lead to much higher Nusselt number values than

circular jet impingement arrays. The results further validate that droplet train impingement is a more effective liquid cooling scheme than circular jet impingement for various impingement patterns.

CHAPTER V

CONCLUSIONS AND RECOMMENDATIONS

The primary objective of this study was to investigate the hydrodynamics and heat transfer induced by single and multiple droplet train impingement arrays. To study the underlying physical mechanism of droplet-induced hydrodynamics and surface heat transfer, a series of experiments have been conducted using high speed optical imaging and IR thermal imaging techniques. Based on the results of this study, the effects of droplet impingement parameters, such as droplet Weber number, impact spacing and impingement patterns on droplet-induced hydrodynamics and surface heat transfer have been elucidated. In this Chapter, the conclusions and recommendations for future study are presented below.

5.1. Conclusions

Based on the experimental results of the current study, it was found that droplet Weber number, impact spacing and impingement pattern play significant roles in droplet-induced hydrodynamics and heat transfer. In this subsection, concluding remarks are made for various impingement patterns, as described below.

5.1.1. Conclusions of single droplet train impingement

From the single droplet train impingement results, the following specific concluding remarks can be made:

- The relationships between droplet-induced crown propagation and crater formation were investigated experimentally. It was found that the crater diameter is proportional to the maximum crown rim diameter for different Weber number, as follows: $d_{cra} = 1.61 \cdot d_{c,rim,\max}$.
- A revised droplet-induced crown propagation model was proposed by taking into account liquid film thickness and velocity distribution within the initial spot. Good agreement was reached between the predictions given by the proposed model and the numerical crown base propagation results by Muthusamy [62].
- A transition from spreading to splashing were observed by increasing droplet Weber number while holding flow rate a constant. Analysis of the crown splashing process show that the droplet-induced crown splashing phenomena could be explained using the Plateau-Rayleigh instability theory.
- The effects of spreading-splashing transition on heat transfer performance have also been investigated at a fixed flow rate condition. It was found that higher droplet Weber number leads to better heat transfer performance when there is no dry-out formation. However, it was also found that strong splashing leads to the formation of dry-out area at lower heat flux values, which is unfavorable for heat transfer.

5.1.2. Conclusions of double droplet train impingement

From the double droplet train impingement results, the following specific concluding remarks can be made:

- Hydrodynamic results of double droplet train impingement show that a hump was formed between impact craters. It was observed that the hump height decreases with impact spacing. It was also found that the hump height does not change much when impact spacing is higher than the maximum crown rim diameter. However, a drastic increases in hump height was observed when impact spacing was lower than maximum crown rim diameter.
- Heat transfer results of double droplet train impingement show that higher impact spacing leads to better heat transfer performance both locally and globally, which is consistent with Tsai [52] and Zhang et al. [53]. A Nusselt number correlation was proposed for double droplet train impingement, which agrees well the experimental Nusselt number data.

5.1.3. Conclusions of triangulated droplet train impingement

From the triangulated droplet train impingement results, the following specific concluding remarks can be made:

- Surface jet flows were observed among impact craters. A transition from laminar to transitional and chaotic surface jet flows were observed by increasing Weber number or decreasing impact spacing. An empirical

correlation has been proposed, which is capable of predicting the transition of surface jet flows.

- Heat transfer measurements show that surface jet flow regimes play a significant role in heat transfer performance. At a fixed flow rate condition, it was found that the transitional surface jet flows was the most favorable for heat transfer.
- A Nusselt number correlation has been proposed for triangulated droplet train impingement. The correlation takes the mathematical form of a Gaussian equation, which agrees well the experimental Nusselt number values.

5.1.4. Conclusions of hexagonal-arranged droplet train impingement

From the hexagonal-arranged droplet train impingement results, the following specific concluding remarks can be made:

- Hydrodynamic results show that the interactions among impact craters become more chaotic as flow rate increases or impact spacing decreases.
- Heat transfer measurements show that lower impact spacing leads to better heat transfer performance locally. However, higher impact spacing leads to better heat transfer performance globally.
- For a hexagonal arrangement with seven droplet trains, lowest surface temperature always coincide with the geometric center of the impingement pattern. However, for a hexagonal arrangement with six

droplet trains, higher surface temperatures were observed in the central area of impingement zone, specifically at high impact spacing conditions.

- Nusselt number correlations have been proposed for hexagonal arranged droplet train impingement arrays. Results show that Nusselt number decreases exponentially with impact spacing, which is consistent with the Nusselt number correlations developed for circular jet impingement arrays [91].

5.1.5. Conclusions of comparisons between droplet train and circular jet impingement

From the comparisons between droplet train and circular jet impingement, the following specific concluding remarks can be made:

- At fixed flow rate conditions, single droplet train impingement leads to higher crater diameter than single circular jet impingement. The results indicate that the periodic nature of droplet train impingement is more favorable in terms of extending the thin film region because of greater fluid momentum.
- At fixed flow rate conditions, single droplet train impingement is more favorable for heat transfer than circular jet impingement. The results indicate that droplet train impingement leads to a more effective thermal mixing mechanism during heat transfer process, as observed in recent studies [59].

- At fixed flow rate and impact spacing conditions, multiple droplet train impingement leads to stronger interactions among the impact craters than multiple circular jet impingement for various impingement patterns. Furthermore, it was found that multiple droplet train impingement leads to better heat transfer performance for various impingement patterns. Dimensionless analysis show that droplet train impingement arrays lead to a 40% higher Nusselt number than when circular jet impingement arrays are used.

5.2. Recommendations for future work

From the results of the study, the following recommendations for future work can be made:

- In this study, most of the cooling liquid flows out of the heater and evaporate without recirculation. Future study should consider building a cooling liquid recirculation system for the purpose of improving liquid usage efficiency. The recirculation system should consider placing micro pumps at the corners of heater. The use of recirculation system may also suppress the formation of dry-out area during the heat transfer process.
- In this study, the heater surface was placed horizontally. Future study could consider the effects of surface inclination angle on droplet-induced hydrodynamics and heat transfer. By using an inclined surface, the gravity potential energy of the liquid could be transferred to kinematic

energy during droplet impingement process. As a result, stagnation of cooling liquid could be effectively suppressed, which might be more favorable for heat transfer purposes.

- In this study, it was found that the crater diameter is proportional to the maximum crown rim diameter for different droplet Weber numbers. However, the underlying physical mechanism of the linear relation remained unknown. Future study should consider analyzing the liquid film flow field within the droplet impingement region in more depth by relying on computational fluid dynamics simulations.
- In this study, it was found that droplet train impingement leads to much better heat transfer performance than circular jet impingement for various impingement patterns. However, comparisons between droplet train impingement and circular jet impingement are only limited to the morphology of liquid films and surface temperature measurements. Future study should consider using a PIV system to compare flow field within the impingement region.

REFERENCES

[1] I. Mudawar, "Assessment of high-heat-flux thermal management schemes," *IEEE Transactions on Components and Packaging Technologies*, vol. 24, no. 2, pp. 122-141, 2001.

[2] J. Kim, "Spray cooling heat transfer: The state of the art," *Int. J. Heat Fluid Flow*, vol. 28, no. 4, pp. 753-767, 2007.

[3] R.-H. Chen, L.C. Chow, J.E. Navedo, "Effects of spray characteristics on critical heat flux in subcooled water spray cooling," *Int. J. Heat Mass Transfer*, vol. 45, no. 19, pp. 4033–4043, 2002.

[4] R.-H. Chen, L.C. Chow, J.E. Navedo, "Optimal spray characteristics in water spray cooling," *Int. J. Heat Mass Transfer*, vol. 47, no. 23, pp. 5095–5099, 2004.

[5] D. E. Tilton, "Spray cooling," Ph. D. dissertation, University of Kentucky, Lexington, KY, 1989.

[6] M. S. Sehmbey, L. C. Chow, O. J. Hahn and M. R. Pais, "Spray cooling of power electronics at cryogenic temperatures," *J. Thermophysics and Heat Transfer*, vol. 9, no. 1, pp. 123-128, 1995.

[7] D. P. Rini, R.-H. Chen and L. C. Chow, "Bubble behavior and nucleate boiling heat transfer in saturated FC-72 spray cooling," *J. Heat Transfer*, vol. 24, pp. 63-72, 2002.

[8] J. Schwarzkof, T. Cader, K. Okamoto, B. Li and B. Ramaprian, "Effects of spray angle in spray cooling thermal management of electronics," *ASME Heat Transfer Engineering Summer Conf.*, vol. 4, pp. 423-431, 2004.

[9] G. Aguilar, H. Vu and J. Nelson, "Influence of angle between nozzle and skin surface on the heat flux and overall heat extraction during cryogen spray cooling," *Phys. Med. Biol.*, vol. 49, no. 10, pp. 147-153, 2004.

[10] Mudawar, K.A. Estes, "Optimizing and predicting CHF in spray cooling of a square surface," *J. Heat Transfer*, vol. 118, no. 3, pp. 672-679, 1996.

[11] E. A. Silk, J. Kim, K. Kiger, "Spray cooling of enhanced surfaces: Impact of structured geometry and spray axis inclination," *Int. J. Heat Mass Transfer*, vol. 49, no. (25-26), pp. 4910-4920, 2006.

[12] C. C. Hsieh and S.C. Yao, "Evaporative heat transfer characteristics of a water spray on micro-structured silicon surfaces," *Int. J. Heat Mass Transfer*, vol. 49, no. (5-6), pp. 962-974, 2006.

[13] J. H. Kim, S. M. You and S. Choi, "Evaporative spray cooling of plain and microporous coated surfaces," *Int. J. Heat Mass Transfer*, vol. 47 no. (14-16), pp. 3307-3315, 2004.

[14] R. Rioboo, C. Tropea and M. Marengo, "Outcomes from a drop impact on solid surfaces," *Atomization and Sprays*, vol. 11, no. 2, pp. 155-165, 2001.

[15] R. Rioboo, M. Marengo and C. Tropea, "Time evolution of liquid drop impact onto solid, dry surfaces," *Experiments in Fluids*, vol. 33, no. 2, pp. 112-124, 2002.

[16] I. V. Roisman, E. Berberović and C. Tropea, "Inertia dominated drop collisions. I. On the universal flow in the lamella," *Physics of Fluids*, vol. 21, pp. 052103, 2009.

[17] I. V. Roisman, R. Rioboo and C. Tropea, "Normal impact of a liquid drop on a dry surface: model for spreading and receding," *Proc. R. Soc. Lond. A*, vol. 458, no. 2022, pp. 1411-1430, 2002.

[18] C. Mundo, M. Sommerfeld and C. Tropea, "Droplet-wall collisions: Experimental studies of the deformation and breakup process," *International J. Multiphase Flow*, vol. 21, no. 2, pp. 151-173, 1995.

[19] G. E. Cossali, M. Marengo, A. Coghe and S. Zhdanov, "The role of time in single drop splash on thin film," *Experiments in Fluids*, vol. 36, no. 6, pp. 888-900, 2004.

[20] S. Mukherjee and J. Abraham, "Crown behavior in drop impact on wet walls," *Physics of Fluids*, vol. 19, pp. 052103, 2007.

[21] G. Liang, Y. Guo, S. Shen and Y. Yang, "Crown behavior and bubble entrainment during a drop impact on a liquid film," *Theor. Comput. Fluid Dynamics*, vol. 28, pp. 159-170, 2014.

[22] D. A. Weiss and A. L. Yarin, "Single drop impact onto liquid films: neck distortion, jetting, tiny bubble entrainment, and crown formation," *J. Fluid Mech.*, vol. 385, pp. 229-254, 1999.

[23] A. L. Yarin and D. A. Weiss, “Impact of drops on solid surfaces: self-similar capillary waves, and splashing as a new type of kinematic discontinuity,” *J. Fluid Mech.*, vol. 283, pp. 141-173, 1995.

[24] A. L. Yarin, “Drop impact dynamics: Splashing, Spreading, Receding, Bouncing…,” *Annual Review of Fluid Mechanics*, vol. 38, pp. 159-192, 2006.

[25] M. F. Trujillo and C. F. Lee, “Modeling crown formation due to the splashing of a droplet,” *Physics of Fluids*, vol. 13, no. 9, pp. 2503-2516, 2001.

[26] M. Rieber and A. Frohn, “A numerical study on the mechanism of splashing,” *International J. Heat Fluid Flow*, vol. 20, no. 5, pp. 455-461, 1999.

[27] H. Shetabivash, F. Ommi and G. Heidarinejad “Numerical analysis of droplet impact onto liquid film,” *Physics of Fluids*, vol. 26, no.1, pp. 022102, 2014.

[28] S. H. Lee, N. Hur and S. Kang, “A numerical analysis of drop impact on liquid film by using a level set method,” *J. Mech. Sci. & Tech.*, vol. 25, no. 10, pp. 2567-2572, 2011.

[29] G. E. Cossali, A. Coghe and M. Marengo, “The impact of a single drop on a wetted solid surface,” *Experiments in Fluids*, vol. 22, no. 6, pp. 463-472, 1997.

[30] A. Wang and C. Chen, “Splashing impact of a single drop onto very thin liquid films,” *Physics of Fluids*, vol. 12, no. 9, pp 2155-2158, 2000.

[31] M. Cheng and J. Lou, “A numerical study on splash of oblique drop impact on wet walls,” *Computer and Fluids*, vol. 115, pp. 11-24, 2015.

[32] L. Rayleigh, "On the instability of jets," *Proceedings of the London Mathematical Society*, vol. s1-s10, no. 1, pp. 4-13, 1878.

[33] J. Schneider and C. Hendricks, "Source of uniform-sized liquid droplets," *Review of Scientific Instruments*, vol. 35, no. 10, pp. 1349-1350, 1964.

[34] L. V. Zhang, P. Brunet, J. Eggers and R. D. Deegan, “Wavelength selection in crown splash,” *Physics of Fluid*s, vol. 22, pp. 122105, 2010.

[35] S. S. Yoon, R. A. Jepsen, S. C. James, J. Liu and G. Aguilar, “Are drop-impact phenomena described by Rayleigh-Taylor or Kelvin-Helmholtz Theory?,” *Drying Technology*, vol. 27, pp. 316-321, 2009.

[36] Y. Liu, P. Tian and L. Xu, "Kelvin-Helmholtz instability in an ultrathin air film causes drop splashing on smooth surfaces," *Proceedings of the National Academy of Sciences of the United States of America*, vol. 112, no. 11, pp. 3280-3284, 2015.

[37] R. Krechetnikov, "Rayleigh-Taylor and Richtmyer-Meshkov instabilities of flat and curved interfaces," *J. Fluid Mech.*, vol. 625, pp. 387-410, 2009.

[38] I. V. Roisman and C. Tropea, "Impact of a drop onto a wetted wall: description of crown formation and propagation," *J. Fluid Mech.*, vol. 472, pp. 373-397, 2002.

[39] G. Agbaglah and R. D. Deegan, "Growth and instability of the liquid rim in the crown splash regime*," J. Fluid Mech.*, vol. 752, pp. 485-496, 2014.

[40] Z. Che, A. Deygas and O. K. Matar, "Impact of droplets on inclined flowing liquid films," *Phys. Rev. E*, vol. 92, no. 2, pp. 023032, 2015.

[41] S. T. Thoroddsen, "The making of a splash," *J. Fluid Mech.*, vol. 690, pp. 1-4, 2012.

[42] R. Krechetnikov and G. M. Homsy, "Crown-formation instability phenomena in the drop splash problem," *J. Colloid & Interface Sci.*, vol. 331, pp. 555-559, 2009.

[43] R. L. Vander Wal, G. M. Berger and S. D. Mozes, "Droplets splashing upon films of the same fluid of various depths," *Exp. In Fluids*, vol. 40, pp. 33-52, 2006.

[44] N. Nikolopoulos, A. Theodorakakos and G. Burgles, "Three-dimensional numerical investigation of a droplet impinging normally onto a wall film," *J. Comp. Phys.*, vol. 225, pp. 322-341, 2007.

[45] B. Kang, "Experimental study of the phenomenon of droplet impact upon a liquid surface," *J. Applied Fluid Mech.*, vol. 9, no. 2, pp. 757-765, 2016.

[46] S. Herbert, S. Fischer, T. G. Roisman and P. Stephan, "Local heat transfer and phase change phenomena during single drop impingement on a hot surface," *Int. J. Heat Mass Tranfer.*, vol. 61, pp. 605-614, 2013.

[47] J. Shen, C. Graber, J. Liburdy, D. pence and V. Narayanan, "Simultaneous droplet impingement dynamics and heat transfer on nano-structured surfaces," *Exp. Therm. & Fluid Sci.*, vol. 34, pp. 496-503, 2010.

[48] E. Berberović, I.V. Roisman, S. Jakirlić and C. Tropea, "Inertia dominated flow and heat transfer in liquid drop spreading on a hot substrate," *Int. J. Heat Fluid Flow*, vol. 21, pp. 785-795, 2011.

[49] M. L. Sawyer, S. M. Jeter and S. I. Abdel-Khalil, "A critical heat flux correlation for droplet impact cooling," *Int. J. Heat Mass Transfer*, vol. 40, no. 9, pp. 2123-2131, 1997.

[50] W. M. Healy, P. J. Halvorson, J. G. Hartley and S. I. Abdel-Khalil, "A critical heat flux correlation for droplet impact cooling at low Weber numbers and various ambient pressures," *Int. J. Heat Mass Transfer*, vol. 41, no. 6-7, pp. 975-978, 1998.

[51] S. M. Sellers and W. Z. Black, "Boiling heat transfer rates for small precisely placed water droplets on a heated horizontal plate," *J. Heat Transfer*, vol. 130, no. 5, pp. 054504, 2008.

[52] H. M. Tsai, "Study of the Effect of Single and Double Droplets Impingement on Surface Cooling," M.S. thesis, Texas A&M University, College Station, TX, 2011.

[53] T. Zhang, H. M. Tsai and J. Alvarado, "Effects of single and double streams of droplet impingements on surface cooling," *Atomization and Sprays*, vol. 24, no. 10, pp. 875-893, 2014.

[54] G. E. Soriano, "Study of the physics of droplet impingement cooling," Ph. D. thesis, Texas A&M University, College Station, TX, 2011.

[55] G. E. Soriano, T. Zhang and J. Alvarado, "Study of the effects of single and multiple periodic droplet impingements on liquid film heat transfer," *Int. J. Heat Mass Transfer*, vol. 77, pp. 449-463, 2014.

[56] Y. P. Lin, "Droplet impingement cooling experiments on nano-structured surfaces," M.S. thesis, Texas A&M University, College Station, TX, 2010.

[57] J. Alvarado and Y. P. Lin, "Multiple droplet impingements on nanostructured surfaces for enhanced spray cooling," *Proceedings of the ASME/JSME 2011 8th Thermal Engineering Joint Conference*, pp. T10241.

[58] M. Colburn, T. Bailey, B. J. Choi, J. G. Ekerdt, S. V. Sreenivasan and C. G. Willson, "Development and advantages of step-and-flash lithography," *Solid State Technology*, vol. 44, no. 7, pp. 67-78, 2011.

[59] M. Trujillo, J. Alvarado, E. Gehring and G. Soriano, “Numerical Simulations and Experimental Characterization of Heat Transfer from a Periodic Impingement of Droplets,” *J. Heat Transfer*, vol. 133, no. 12, pp. 122201, 2011.

[60] M. Trujillo and S. Lewis, “Thermal boundary layer analysis corresponding to droplet train impingement,” *Physics of Fluids*, vol. 24, no. 11, pp. 112102, 2012.

[61] X. Liu, J. H. Lienhard V and J. S. Lombara, “Convective heat transfer by impingement of circular liquid jets,” *J. Heat Transfer*, vol. 113, no. 3, pp 571-582, 1990.

[62] T. Zhang, J. Muthusamy, J. Alvarado, A. Kanjirakat and R. Sadr, “Numerical and experimental investigations of crown propagation dynamics induced by droplet train impingement,” *Intl. J. Heat Fluid Flow*, vol. 57, pp. 24-33, 2016.

[63] J. Muthusamy, T. Zhang, J. Alvarado, A. Kanjirakat and R. Sadr, “Effects of High Frequency Droplet Train Impingement on Crown Propagation Dynamics and Heat Transfer,” *J. Heat Transfer*, vol. 138, no.2, pp. 020903, 2016.

[64] T. Zhang, J. Alvarado, J. Muthusamy, A. Kanjirakat and R. Sadr, “Effects of High Frequency Droplet Train Impingement on Spreading-Splashing Transition, Film Hydrodynamics and Heat Transfer,” *J. Heat Transfer*, vol. 138, no.2, pp. 020902, 2016.

[65] T. Zhang, J. Alvarado, J. Muthusamy, A. Kanjirakat and R. Sadr, “Effects of screen laminates on droplet-induced film hydrodynamics and surface heat transfer,” *J. Heat Transfer*, vo. 138, no. 8, pp. 080902, 2016.

[66] T. Zhang, J. Alvarado, A. Kanjirakat and R. Sadr, “Experimental characterization and numerical simulation of crown propagation induced by impingement of droplet train,” *67th Annual Meeting of the APS Division of Fluid Dynamics*, vol. 59, no. 20, BAPS.2014.DFD.M15.8, 2014.

[67] T. Zhang, J. Alvarado, A. Kanjirakat and R. Sadr, “Hydrodynamics of micro-scale surface flows induced by triangulated droplet stream impingement array,” *67th Annual Meeting of the APS Division of Fluid Dynamics*, vol. 59, no.20, BAPS.2014.DFD.M12.1, 2014.

[68] T. Zhang and J. Alvarado, “Crown Propagation Dynamics Induced by High Frequency Droplet Impingements,” *67th Annual Meeting of the APS Division of Fluid Dynamics*, APS.DFD.2014.GFM.V0010, 2014.

[69] T. Zhang and J. Alvarado, “Thermal Performance of Triangulated Array of Droplet Streams,” *ASME 2015 International Technical Conference and Exhibition on Packaging and Integration of Electronic and Photonic Microsystems*, IPACK2015-48672, 2015.

[70] T. Zhang, J. Alvarado, J. Muthusamy, A. Kanjirakat and R. Sadr, “Hydrodynamics and heat transfer of micro-scale surface flows induced by triangulated droplet stream impingement array,” *ASTFE First Thermal and Fluid Engineering Summer Conference*, TFESC-12576, 2015

[71] T. Zhang, J. Muthusamy, J. Alvarado, A. Kanjirakat and R. Sadr, “Experimental and Numerical Characterization of Droplet-Induced Spreading-Splashing Transition in Surface Cooling,” *ASME 2016 Sumer Heat Transfer Conference collocated with the ASME 2016 Fluids Engineering Division Summer Meeting and the ASME 2016 14th International Conference on Nanochannels, Microchannels, and Minichannels*, HT-2016-7226, vol. 2, pp. V002T08A013, 2016.

[72] T. Zhang, J. Muthusamy, J. Alvarado, A. Kanjirakat and R. Sadr, “Experimental and Numerical Visualization of Droplet-Induced Crown Splashing Dynamics,” *J. Heat Transfer*, in press, 2017.

[73] Y. Yu, D. Sun, K. Wu, Y. Xu, H. Chen, X. Zhang and L. Qiu, “CFD study on mean flow engine for wind power exploitation,” *Energy Conversion and Management*, vol. 52, no. 6, pp. 2355-2359, 2011.

[74] D. Sun, Y. Xu, H. Chen, K. Wu, K. Liu and Y. Yu, “A mean flow acoustic engine capable of wind energy harvesting,” *Energy Conversion and Management*, vol. 63, pp. 101-105, 2012.

[75] I. N. Reddy, V. R. Reddy, N. Sridhara, S. Basavaraja, M. Venkatanarayana, V. S. Rao, A. K. Sharma, and A. Dey, “Development of SiO2 based thin film on metal foils for space applications,” *Ceramics International*, vol. 39, no. 7, pp. 8493-8498, 2013.

[76] D. B. Mahadik, S. Gujjar, G. M. Gouda, H. C. Barshilia, "Double layer SiO2/Al2O3 high emissivity coatings on stainless steel substrates using simple spray deposition system," *Applied Surface Science*, vol. 299, pp. 6-11, 2014.

[77] R. G. Driggers, *Encyclopedia of optical engineering*, New York: Marcel Dekker Inc., 2003.

[78] T. C. Tszeng and V. A. Saraf, "A study of fin effects in the measurement of temperature using surface-mounted thermocouples," *J. Heat Transfer*, vol. 125, no. 5, pp. 926-935, 2003.

[79] S. Kline and F. McClintock, "Describing uncertainties in single-sample experiments," *Mechanical Engineering*, vol. 75, no. 1, pp. 3-8, 1955.

[80] C. Hirt and B. Nichols, "Volume of Fluid (VOF) method for the dynamics of free boundaries," *J. Compt. Phys.*, vol. 39, pp. 201-225, 1981.

[81] D. Maynes, M. Johnson and B. Webb, "Fee-surface liquid jet impingement on rib patterned superhydrophobic surfaces," *Physics of Fluids*, vol. 23, pp. 052104, 2011.

[82] S. Chandra and C. T. Avedisian, "On the collision of a droplet with a solid surface," *Proceedings of the Royal Society of London A: Mathematical, Physical and Engineering Sciences*, vol. 432, no. 1884, pp. 13-41, 1991.

[83] L. Qiu, S. Dubey, F. H. Choo and F. Duan, "Splashing of high speed droplet train impinging on a hot surface," *Applied Physics Letters*, vol. 107, no. 16, pp. 164102, 2015.

[84] L. Qiu, S. Dubey, F. H. Choo and F. Duan, "The transition of time-dependent spreading diameter and splashing angle when a droplet train impinging on to a hot surface," *RSC Advances*, vol. 6, no. 17, pp. 13644-13652, 2016.

[85] L. Qiu, S. Dubey, F. H. Choo and F. Duan, "The impingement of droplet train onto a flat hot surface with high wall superheat," *ASME 2016 5th International Conference on Micro/Nanoscale Heat and Mass Transfer*, pp. V001T04A002, 2016.

[86] L. Li, X. Jia, Y. Liu and M. Su, "Simulation of double droplets impact on liquid film by a simplified lattice Boltzmann model," *Applied Thermal Engineering*, vol. 98, no. 5, pp. 656-669, 2016.

[87] L. Li, X. Jia, Y. Liu and M. Su, "Simulation of flow process of two droplets with large density ratio impacting on liquid film by two-phase Lattice Boltzmann method," *Journal of Chinese Society of Power Engineering*, vol. 35, no. 6, pp. 457-462, 2015

[88] K. A. Raman, R. K. Jaiman, T. S. Lee and H. T. Low, "On the dynamics of crown structure in simultaneous two droplets impact onto stationary and moving liquid film," *Computer and Fluids*, vol. 107, no. 31, pp. 285-300, 2015.

[89] Y. Pan and B. W. Webb, “Heat transfer characteristics of arrays of free-surface liquid jets,” *J. Heat Transfer*, vol. 117, no. 4, pp. 878-883, 1995.

[90] A. J. Robinson and E. Schnitzler, “An experimental investigation of free and submerged miniature liquid jet array impingement heat transfer.” *Exp. Thermal Fluid Sci.*, vol. 32, no.1, pp. 1-13, 2007.

[91] M. Fabbri and V. K. Dhir, “Optimized heat transfer for high power electronic cooling using arrays of microjets,” *J. Heat Transfer*, vol. 127, no. 7, pp. 760-769, 2005.

[92] R. P. Kate, P. K. Das and S. Chakraborty, “An experimental investigation on the interaction of hydraulic jumps formed by two normal impinging circular liquid jets,” *J. Fluid Mech.*, vol. 590, pp. 355-380, 2007.

[93] T. Bohr, P. Dimon and V. Putkaradze, “Shallow-water approach to the circular hydraulic jump,” *J. Fluid Mech.*, vol. 254, pp. 635-648, 1993.

[94] J. W. M. Bush and J. M. Aristoff, “The influence of surface tension on the circular hydraulic jump,” *J. Fluid Mech.*, vol. 489, pp. 229-238, 2003.